International Scientific-Technical and Production Journal

The Paton WELDING JOURNAL

April 2004 # 4

English translation of the monthly «Avtomaticheskaya Svarka» (Automatic Welding) journal published in Russian since 1948

Founders: *E.O. Paton Electric Welding Institute of the NAS of Ukraine*
International Association «Welding»

Publisher: *International Association «Welding»*

Address:
E.O. Paton Electric Welding Institute,
International Association «Welding»,
11, Bozhenko str., 03680, Kyiv, Ukraine
Tel.: (38044) 227 67 57
Fax: (38044) 268 04 86
E-mail: journal@paton.kiev.ua
http://www.nas.gov.ua/pwj

State Registration Certificate
KV 4790 of 09.01.2001

Subscriptions:
$460, 12 issues per year,
postage and packaging included.
Back issues available.

CONTENTS

EFFECT OF CHEMICAL INHOMOGENEITY ON THE FORMATION OF ACICULAR FERRITE IN HIGH-STRENGTH WELD METAL

G.M. GRIGORENKO, V.A. KOSTIN, V.V. GOLOVKO and V.F. GRABIN
E.O. Paton Electric Welding Institute, NASU, Kiev, Ukraine

It is shown that the role of non-metallic inclusions in the formation of acicular ferrite is associated with the formation around non-metallic inclusions of regions of a solid solution with an increased content of nickel and manganese and different dislocation structure. Chemical composition of weld metal and different degree of a chemical inhomogeneity in the distribution of austenite-forming elements depend on the change in oxygen potential of the flux and adding of elements of deoxidizers (Al, Ti and Al + Ti) into it.

Keywords: *arc welding, low-alloy, steels, weld, microstructure, acicular ferrite, chemical inhomogeneity, MAC-phase, non-metallic inclusions*

Reliability of welded joints of structures made from low-alloy steels is defined mainly by structural-phase composition of weld metal, whose mechanical properties are provided by the formation of a complex of ferrite-cementite structures and structures of austenite decay in the intermediate region and of martensite in some cases. The main structure constituents, forming in weld metal of this type, are acicular ferrite (AF), polygonal ferrite (PF), Widmannstaetten ferrite (WF), morphological forms of ferrite with ordered (FOSP) and non-ordered (FNOSP) second phases, martensitic-austenitic-carbide phase (MAC-phase). During metal cooling a large amount of non-metallic inclusions (NMI) is formed as a result of proceeding reactions of deoxidation of alloying and impurity elements in weld metal, which contribute greatly to the kinetics of formation of its microstructure.

It was established that the most favourable structure is the AF structure from the point of view of providing the complex of regulated properties of the welded joints. Many works [1–4 et al.] were devoted to the study of conditions of formation of this structure constituent in metal of low-alloy welds. Two main approaches to the explanation of the AF formation mechanism were formulated in these works. According to the first approach, the initiation of AF occurs inside the austenite grain during cooling at the interface with NMI or near them. According to the second approach, the probability of initiation and growth of AF is due to the content of alloying elements in solid solution and rate of metal cooling.

Peculiarities of effect of alloying and impurity elements on AF formation are defined by their tendency to influence the austenite resistance, capability to change the temperature of beginning and completion of transformation, position of a martensite point on a cooling curve, and also the capability to change the rate of carbon diffusion in weld metal.

At the same time, when analysing the effect of any chemical element on the formation of a definite type of a structure constituent it is accepted to make allowance for its total content in metal, i.e. in this case the chemical composition is considered as a macroscopic characteristic of the metal, whereas a share of a structure constituent, its sizes and shapes refer to microscopic objects. This non-conformity of object parameters and methods of assessment of their chemical composition can explain a number of contradictory data about the nature of AF effect on the mechanical properties of weld metal.

The aim of the present work was to establish the correlation between the nature of distribution of alloying elements in solid solution and process of AF formation in weld metal.

Procedure of experiment. Experiments were made using the arc welding of butt joints under agglomerated fluxes. By varying the composition of fluxes it was possible to simulate the effect of oxygen potential of welding consumables, deoxidation and alloying of weld pool on formation of both NMI and also separate structure constituents in weld metal. For this purpose, such active deoxidizers, as metallic aluminium and/or ferrotitanium (≈ 25 % Ti in ferrotitanium) were added to the composition of fluxes having different oxygen potential.

Butt joints, assembled in accordance with requirements of the European standard EN 1597-1 [5], were made from 20 mm thick low-alloy steel 10KhSND and welded with 5 mm diameter wire Sv-04N3GTA. Welding was performed at direct current of reverse polarity and following conditions: I_w = (620 ± 5) A; U_a = = (30 ± 1) V; v_w = (20 ± 0.5) m/h; q_w = 48 kJ/cm.

Three types of fluxes were used in experiments. They differed by an index of basicity *BI*, calculated by IIW formula [6]. Oxygen potential was determined in accordance with the formula given in [7]:

$$\pi_O = RT\ln P_{O_2}\ [\text{kJ/mol } O_2],$$

where R is the universal gas constant equal to 8.31 J/(mol·K); T is the temperature; P_{O_2} is the par-

Table 1. Type of welding fluxes used in experiments, their basicity and oxygen potential

Type of welding flux	*Designation of series**	*No. of weld metal*	*Oxygen potential of flux* π_O, *kJ/mol*
Acid (BI = 0.67)	A	13A	−307
	T	13T	
	AT	13AT	
Neutral (BI = 1.25)	A	9A	−337
	T	9T	
	AT	9AT	
Basic (BI = 2.53)	A	19A	−369
	T	19T	
	AT	19AT	

*0.5 % Al was added aditionally into fluxes of series A, 0.4 % Ti — to series T, 0.5 % Al + 0.2 % Ti — to series AT.

tial pressure of oxygen over the slag melt, measured by the procedure of work [8].

Type of welding fluxes, their basicity and oxygen potential are given in Table 1.

Samples were selected from weld metal for determination of chemical composition using the method of a spectral analysis in unit Baird, equipped with computer IBM PC, and also for metallographic examinations (Table 2).

Metallographic examinations determined a volumetric share of separate constituents of weld metal microstructure, content of alloying elements in solid solution and element composition of NMI. Microstructure was examined by the methods of optical and electron metallography using a light microscope «Neophot-32» and JEOL scanning electron microscope JSM-840, equipped with a board of capture of images MicroCapture with a subsequent record of image on the computer screen. Instrument is completed with a

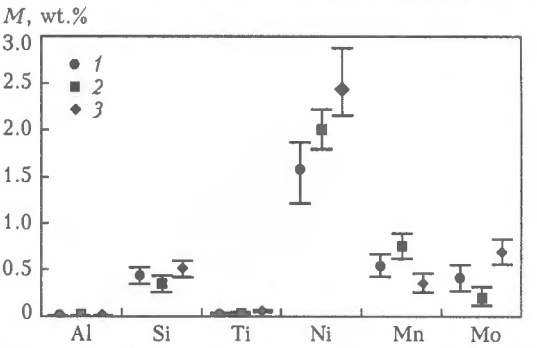

Figure 1. Range of content M of alloying elements in PF (*1*), AF (*2*) and MAC-phase (*3*)

system for construction of concentration maps DIGIMAP, based on a discrete scanning by electron beam over the sample surface with a record of intensity of characteristic radiation in each point of the scanning region consisting of 128×128 points and having 165×165 μm sizes.

Quantitative determination of microstructure constituents was made in accordance with IIW procedure [9]. Content of alloying elements in solid solution and element composition of NMI were determined by X-ray diffraction microanalysis using a Link System energy-dispersion spectrometer Link 860/500 and Ortec wave-dispersion spectrometer «Ortec».

Results of examinations. Nature of microstructure and data about the quantitative composition of structure constituents in the deposited metal are presented in [10]. It is shown that the weld metal structure consists mainly of AF, PF, WF, FOSP, FNOSP and MAC-phase.

Content of alloying elements was determined during investigation of effect of oxygen potential [10] (Table 3). The use of fluxes in experiments within the wide range of oxygen potential (BI = 0.67–2.53) allowed determination of the range of content of alloying elements in different structure constituents of weld metal, typical of the given system of weld pool deoxidation (Figure 1).

Table 2. Chemical composition of deposited metal, wt.%

Object of analysis	*C*	*Al*	*Si*	*Ti*	*Ni*	*Mn*	*Mo*	*Cr*	*Cu*	*S*	*P*	*O*
Welding wire	0.020	0.002	0.16	0.004	2.29	0.62	0.17	0.17	0.20	0.010	0.011	0.013
No.of weld metal												
13A	0.032	0.007	0.84	0.001	2.40	0.84	0.19	0.12	0.15	0.009	0.004	0.050
13T	0.031	0.010	0.89	0.003	2.48	0.82	0.20	0.11	0.15	0.019	0.005	0.065
13AT	0.035	0.007	0.81	0.001	2.39	0.82	0.19	0.13	0.16	0.009	0.005	0.045
9A	0.036	0.011	0.35	0.015	2.32	0.84	0.18	0.18	0.18	0.009	0.007	0.027
9T	0.036	0.014	0.32	0.003	2.36	0.84	0.17	0.18	0.19	0.008	0.007	0.035
9AT	0.039	0.014	0.41	0.003	2.46	0.89	0.19	0.17	0.19	0.009	0.008	0.025
19A	0.037	0.023	0.13	0.002	2.43	0.55	0.17	0.17	0.14	0.009	0.005	0.025
19T	0.036	0.028	0.13	0.003	2.46	0.52	0.16	0.17	0.13	0.007	0.009	0.027
19AT	0.038	0.034	0.12	0.005	2.53	0.52	0.19	0.15	0.15	0.008	0.007	0.022

Table 3. Content of alloying elements in structure constituents of weld metal

Object of analysis	Elements, wt.%					
	Al	*Si*	*Ti*	*Ni*	*Mn*	*Mo*
PF	0.002–0.006 / 0.004	0.336–0.504 / 0.420	0.008–0.024 / 0.016	1.209–1.859 / 1.580	0.420–0.653 / 0.530	0.260–0.543 / 0.410
AF	0.002–0.008 / 0.004	0.250–0.420 / 0.340	0.015–0.032 / 0.023	1.800–2.226 / 2.010	0.620–0.901 / 0.750	0.110–0.320 / 0.210
MAC-phase	0–0.001 / 0.001	0.413–0.585 / 0.510	0.040–0.054 / 0.047	2.150–2.890 / 2.430	0.250–0.440 / 0.340	0.546–0.822 / 0.690

Note. Range of values is given in numerator, mean values are given in denominator.

In connection with the fact that the methods of a local analysis do not provide the complete representation of nature, level and degree of non-homogeneity in the distribution of alloying and impurity elements in weld metal structure, the method of construction of concentration maps by a selected element was used to study the nature of distribution of elements within the ranges of the primary austenite grain [11].

Using the results obtained the concentration range of content of alloying elements in main structure constituents of weld metal was determined for each of alloying elements. Typical samples of these maps of distribution of manganese, silicon, nickel and molybdenum are presented in Figure 2. Comparison of results of digital processing of concentration maps with data about the structural composition of weld metal could establish the definite interrelation between the area of solid solution regions and AF content.

Comparison of concentration maps with a microstructure of weld shows that content of 1.8–2.2 % Ni and 0.7–0.9 % Mn in a local microregion contributes to the AF formation, however, it is extremely important here to reduce the content of silicon and sulphur to minimum (not more than 0.8 % Si and not more than 0.5 % S).

In construction of concentration maps the presence of regions with a composition different from that of matrix was observed around some NMI (Figure 3). To have the more comprehensive study of these regions the polished samples were investigated under the condition of back-scattered electrons, resulting in establishing that these regions have the darker colour and differed by their morphology. In some cases they cover NMI completely, while in other cases they are arranged asymmetrically as regards to NMI, and they can almost be absent near inclusions of 0.1–0.3 μm (Figure 4). It was also established that the size of these regions is equal to 0.1–0.5 μm, and the nature of their formation around inclusions, located inside

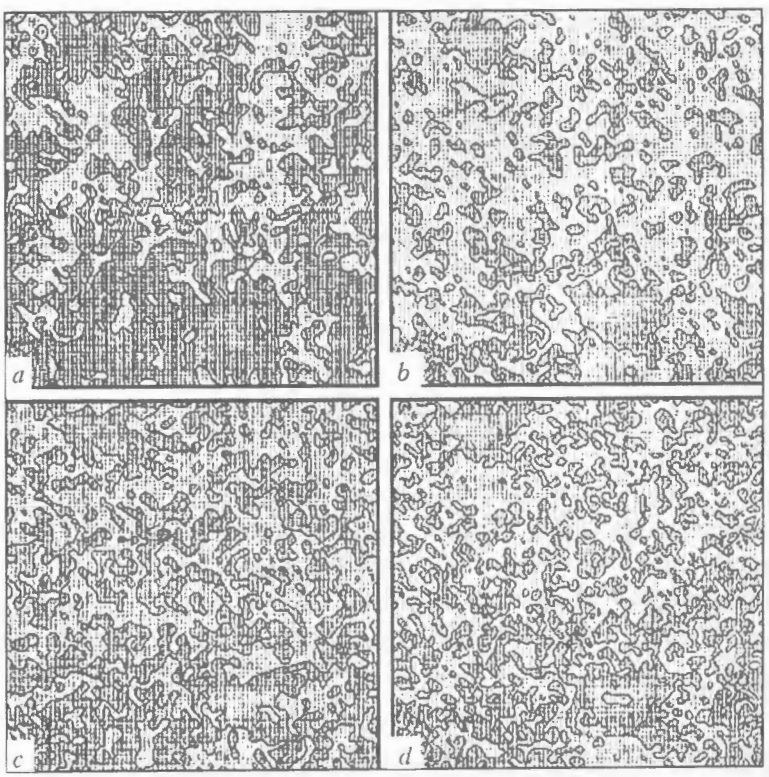

Figure 2. Concentration maps of distribution of elements in weld metal: *a* — manganese; *b* — silicon; *c* — nickel; *d* — molybdenum

or along the boundaries of the primary austenite, is differed.

To determine the nature of distribution of alloying and impurity elements in the regions of solid solution, adjacent to NMI, a linear scanning of the mentioned regions was made using the energy-dispersion spectrometer. Investigations showed that regions of the darker colour around NMI are enriched with nickel (Figure 5).

These regions of the structure were examined in the transmission electron microscope (TEM) using the method of a diffraction microanalysis. It was established that the interplanar spacing a in these regions is 0.289 nm, for α-Fe it is equal to 0.2866 nm. It can be concluded as a result of comparison of data obtained that the examined regions represent a solid solution α-Fe with an increased (3–4 %) content of nickel. In addition, NMI of size of more than 1 μm in metal of examined welds have, as a rule, a complex composition and morphology. An increased content of sulphur and manganese was observed at the NMI surface that makes it possible to assume the feasibility of formation of fringing at the boundary of inclusions, containing the manganese sulphides. Internal regions of inclusions consist of two parts with different concentration of aluminium, silicon and manganese. The external part contains approximately 40 % Si, 25 % Mn, 35 % Al. Otherwise in the internal part of NMI, where the content of manganese (≈ 45 %) at 30 % Si and 20 % Al (not more) is higher. The mutual arrangement of constituents of phases is random that can be due to the peculiarities of kinetics of their formation in the process of solidification of the weld pool. Inclusions of size of not less than 0.3 μm are homogeneous and matrix around them has a homogeneous composition.

The metallographic examinations showed that in AF, located inside the former grain of the primary austenite, the area around NMI with composition different from the surrounding matrix is practically always formed, while in PF, located along the boundary of the former austenite grain, this region is observed more seldom. It can be assumed that this formation of the given region is due to the peculiarities of formation of the dislocation structure around the NMI in a ferrite matrix.

To check this assumption, the dislocation structure in samples of welded joints was examined. It was

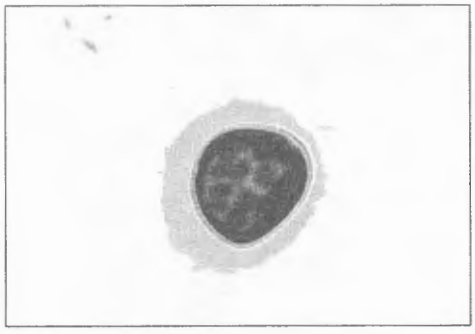

Figure 3. Illustration of region around NMI of composition different from that of matrix (×3000)

established that the AF structure is characterized by a high density of dislocations $\rho = 10^{12}$–10^{14} cm^{-2} (Figure 6, *b*). The peculiar feature of AF grains is a noticeable fragmentation of structure into dislocation-free regions which are separated by regions with a high ($\rho = 10^{14}$ cm^{-2}) dislocation density (Figure 6, *b*). In PF grains the density of dislocations is much lower ($\rho = 10^{10}$ cm^{-2}), while only separate dislocation clusters are formed within the grain (Figure 6, *a*).

The examined microstructure constituents are also different by the nature of distribution of density of dislocations near NMI. For PF the density of dislocations in microregions around NMI is almost the same as that inside the grain body (Figure 7, *a*), while in AF it is higher near NMI (Figure 7, *b*) than in the more distant regions of the solid solution.

Analysis of results and their discussion. Results obtained during investigations make it possible to conclude that there is a high probability of AF formation in the process of structural transformations in the areas of solid solution enriched with manganese and nickel. Data, presented in Figure 8, show that there is a clearly visible relationship between the area of solid solution regions, containing 1.8–2.2 % Ni and a volumetric share of AF in the weld metal structure. This relationship has a straightlinear nature at the presence of AF up to 40 %. At the higher contents of AF it is deviated from linear that can be caused by increase in content of MAC-phase in the regions examined (Figure 9). It is possible to prevent the deviation from the linearity of the above-mentioned relationship by correcting the obtained results with allowance for a mutual effect of the MAC-phase (Figure 8).

The increase in probability of formation of AF structure in regions enriched with nickel and manga-

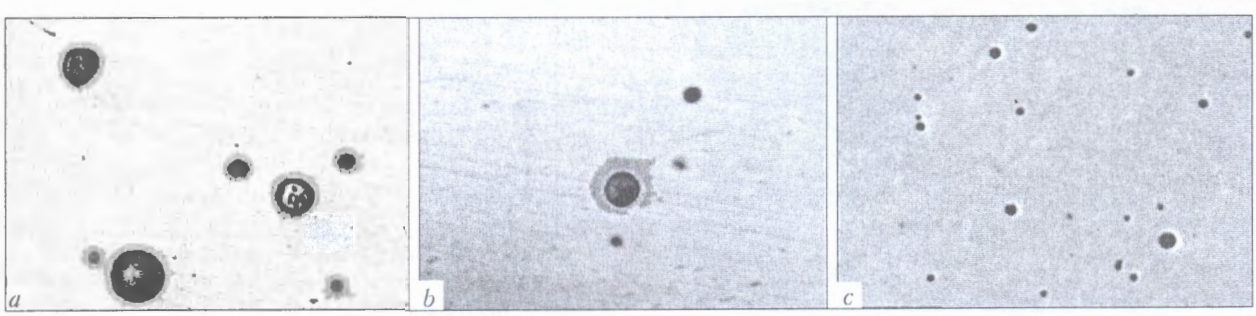

Figure 4. Formation of regions around NMI: *a* — zone covers completely NMI; *b* — zone is formed from one side; *c* — zone is not formed (×1000)

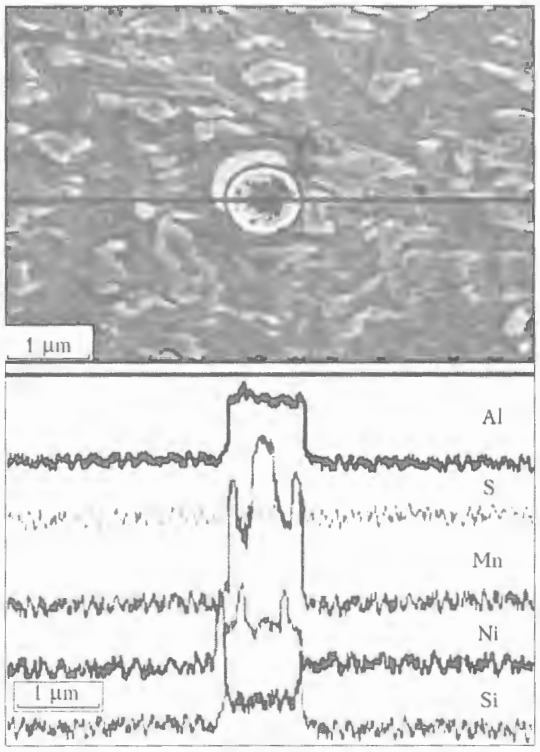

Figure 5. Nature of distribution of alloying elements (manganese, silicon, nickel, aluminium and sulphur) in the scanning line passing through NMI

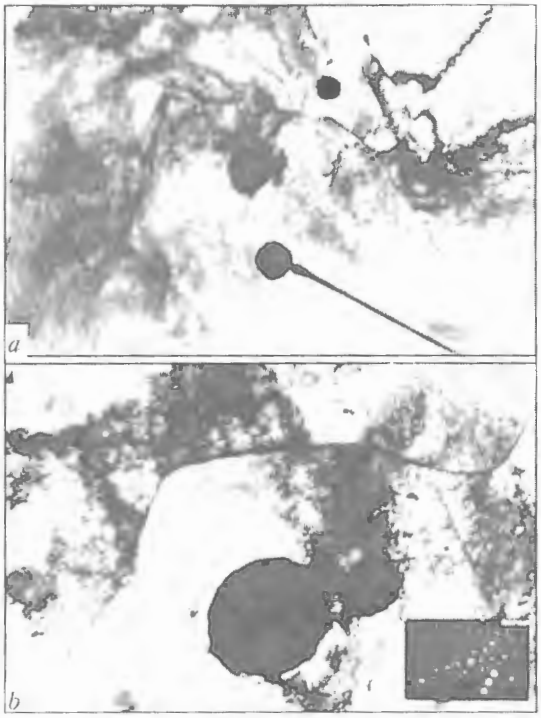

Figure 7. Distribution of dislocations near NMI in PF (*a*) and AF (*b*) (microdiffraction pattern of region adjacent to NMI is given in the lower angle) (×20000)

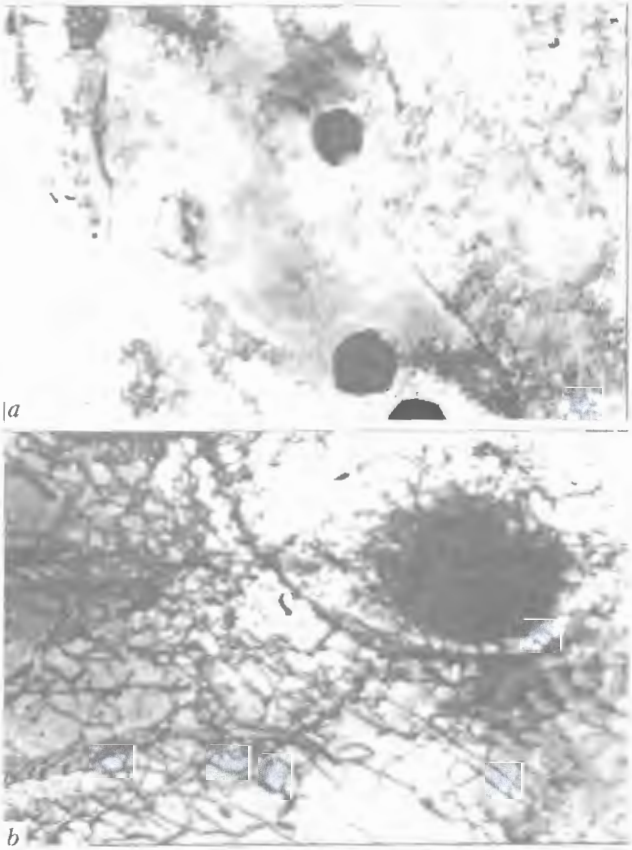

Figure 6. Nature of distribution of dislocations in PF (*a*) and AF (*b*) (×20000)

nese, is, probably, due to a strong austenite-forming action of these elements, as a result of which the structural transformations during recrystallization are occurred by a shear mechanism. Simultaneously, the number of regions of solid solution with maximum content of these elements is increased, resulting in increase of MAC-phase content in weld metal, therefore, the increase in AF share is accompanied often by the increase in a volumetric share of the MAC-phase.

The second specific factor influencing the formation of AF in weld metal structure is NMI [12].

The high rate of weld metal cooling contributes to the formation of chemical inhomogeneity inside the primary grains. In areas, enriched with nickel and

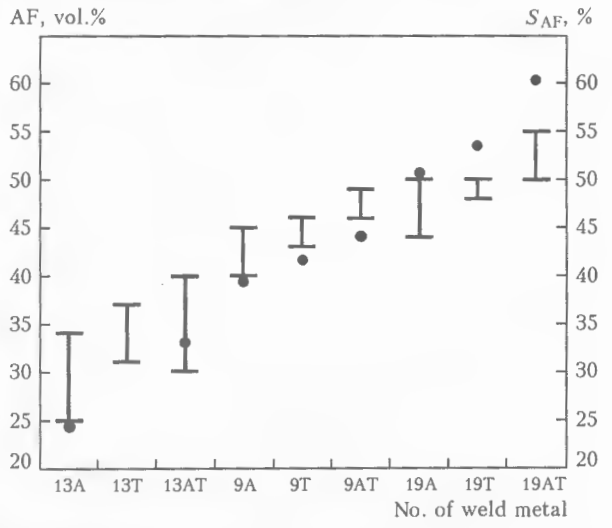

Figure 8. Interrelation between the area of regions S_{AF} with optimum content of nickel (*points*) and share of AF (*vertical line*) in weld metal

manganese, the strengthening of a ferritic matrix during recrystallization is occurred [13], therefore, regions with an increased density of dislocations are formed around NMI occurred in these regions. In connection with the fact that the rate of diffusion of alloying elements in nuclei of dislocations is much higher than in dislocation-free regions, the rate of nickel diffusion is increased in the latter that contributes to the formation of concentration zones with increased content of nickel in solid solution around NMI. The probability of formation of AF structure in these regions is much higher than in the regions with the lower content of this element. The regions enriched with nickel and manganese along the boundaries of the primary grains are little observed, therefore, density of dislocations is lower and the concentration zones with increased content of nickel near inclusions are more seldom observed around NMI located in this zone. Probability of formation of quenched structures of AF type in these regions is decreased.

Thus, it can be concluded on the basis of results that the concentration zones of an appropriate composition around NMI contribute to the formation of AF structure in these regions of solid solution during the process of cooling.

CONCLUSIONS

1. It was established that the microstructure of weld metal is characterized by the presence of chemical inhomogeneity of solid solution in the form of regions with increased content of nickel and manganese.

2. It was determined that the amount of regions with increased content of nickel and manganese is much higher inside the grains of the primary austenite than in the near-boundary regions.

3. In the regions of solid solution enriched with nickel and manganese the probability of proceeding the structural transformations during recrystallization by a shear mechanism with the AF formation is increased.

4. It was established that the dislocation structures of high density are formed around NMI, located in the regions of solid solution with increased content of nickel and manganese, thus contributing to the formation of concentration zones in regions adjacent to inclusion.

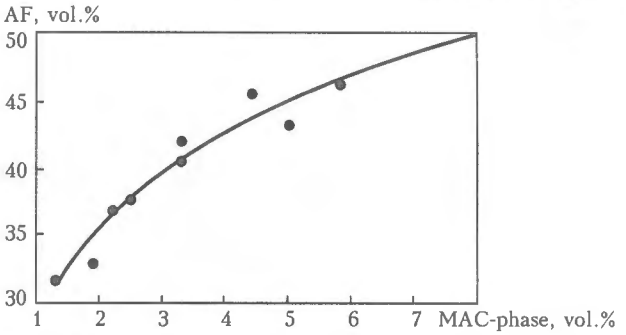

Figure 9. Interrelation between the volumetric shares of MAC-phase and AF in weld metal

5. Formation of concentration zones around the inclusion leads to the formation of AF structure initiated by this inclusion.

1. Mori, N., Homma, H., Okita, S. (1980) The behavior of B and N in notch toughness improvement of Ti–B bearing weld metals. *IIW Doc. IX-1158–80*.
2. Bramfitt, B.L. (1970) The effect of carbide and nitride additions on the heterogeneous nucleation behavior of liquid iron. *Met. Transact.*, **1**, 1987–1995.
3. Abson, D.J., Dolby, R.E., Hart, P.H.M. (1978) The role of non-metallic inclusions in ferrite nucleation in carbon steel weld metals. In: *Proc. of Int. Conf. on Trends in Steels and Consumables for Welding*, London, March, 1978. London: TWI.
4. Ricks, R.A., Howell, P.R., Barrite, G.S. (1982) The nature of acicular ferrite in HSLA steel weld metals. *J. Mat. Sci.*, **17**, 732.
5. *ISO 15792–1:2000*. Welding consumables. Test method. Part 1: Test methods for all-weld metal test in steel, nickel and alloys.
6. (1977) Classification and symbolization of bare steel wire electrodes and fluxes for submerged arc welding of structural steels. *IIW Doc. XII-666–77*.
7. Kazachkov, E.A. (1988) *Calculations on theory of metallurgical processes*. Moscow: Metallurgiya.
8. Pokhodnya, I.K., Golovko, V.V., Kushneryov, D.M. et al. (1990) Evaluation of oxidizing capacity of ceramic fluxes. *Avtomatich. Svarka*, **2**, 45–48.
9. (1986) Guidelines for the classification of ferritic steel weld metal microstructural constituents using the light microscope. *Weld. in the World*, 24(**7/8**), 144–148.
10. Grigorenko, G.M., Golovko, V.V., Grabin, V.F. et al. (2004) Effect of metallurgical characteristics of flux on structure and phase composition of high-strength weld metal. *The Paton Welding J.*, **3**, 7–14.
11. Grigorenko, G.M., Borisova, A.L., Taranova, T.G. et al. (1993) Examination of chemical inhomogeneity and evaluation of amorphisation degree of plasma coatings with use of scanning electron microscopy. *Problemy Spets. Elektrometallurgii*, **4**, 47–53.
12. Liu, S., Olson, D.L. (1986) The role of inclusions in controlling HSLA steel weld microstructures. *Welding J.*, **6**, 139–149.
13. Gulyaev, A.P. (1978) *Metals science*. Moscow: Metallurgiya.

DISTRIBUTION OF TEMPERATURE IN HAZ IN EXPLOSION WELDING OF DISSIMILAR METALS

A.P. PEEV, S.V. KUZMIN and V.I. LYSAK
Volgograd State Technical University, Volgograd, Russia

Design-experimental procedure of evaluation of thermal situation in HAZ of explosion-welded dissimilar metals, differing greatly in their physical-chemical properties, are presented. It is shown that the occurrence of molten metal regions at the interface of composite layers is due to the heat generated as a result of a plastic deformation in the stronger metal.

Keywords: *explosion welding, similar and dissimilar metals, heat-affected zone, shear, plastic deformation, distribution of temperature*

The process of explosion welding of metals is accompanied by an abrupt increase in temperature in a joining zone, that is proved by change in structure of metal of the HAZ (regions of recrystallization, cast metal, formation of non-equilibrium structures and chemical compounds and others) that is explained by the transformation of the deformation energy into heat energy [1–3 and oth.]. In works [4–8 and oth.] different approaches were applied for the solution of heat problem in explosion welding of metals, however, none of the suggested models makes allowance for the interrelation between the high-speed plastic deformation of near-contact volumes of HAZ metal and resultant generated heat. In addition, it should be noted that the heat generated in these volumes, is distributed non-uniformly because of existence of the deformation gradient.

Coming from above-mentioned, the aim of the present work was to make the calculation-experimental evaluation of thermal situation in HAZ in explosion welding of metals on the basis of analysis of distribution of energy of plastic deformation between layers.

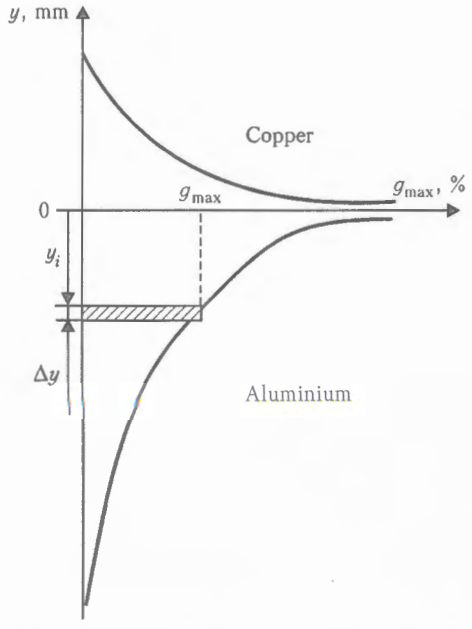

Figure 1. Scheme to the procedure of calculation of a shear deformation energy

The total energy of deformation is determined by integration of elementary works by y:

$$A = S_k \int_0^{\delta} \varepsilon(y) dy, \qquad (1)$$

where $\varepsilon(y)$ is the current value of deformation; δ is the thickness of plate being examined; S_k is the resistance of material against deformation (or limiting strength of material, depending on ultimate rupture strength and reduction in area), equal numerically to the dynamic yield strength (S_k^{Cu} = 640 MPa, S_k^{Al} = = 108 MPa [9]).

When calculating the integral, let us use the approximate method of rectangles. For this purpose the interval of integrating from zero (line of joining) up to δ (plate thickness) will be divided by n-equal parts and for the points of division y_1, y_2, ..., y_{n-1} and y_n the value of the integrating function $\varepsilon(y)$ will be calculated. Then the approximate value A_∂ will be equal to

$$A_\partial = \sum_{i=1}^{n} \Delta A_{\partial_i} = S_k \Delta y \sum_{i=1}^{n} g_{max\,i}, \qquad (2)$$

where $\Delta y = \delta / n$; g_{max} is the current mean value of shear deformation realizing in some i-th layer (Figure 1).

Processing of available diagrams $g_{max} = f(y)$ and analysis of data obtained allowed revealing of the following regularities:

- in case of explosion welding of similar materials (Al + Al) (Figure 2, *a, c*) the calculated values of deformation energy in flyer and fixed elements do not differ from each other by more than 10 %, i.e. energy consumed for plastic deformation of metals of both plates is divided between them almost equally. This regularity is preserved in varying welding conditions within the wide range;
- similar distribution of energy, consumed for plastic deformation, is observed also in case of explosion welding of copper with aluminium (Figure 2, *b, d*)

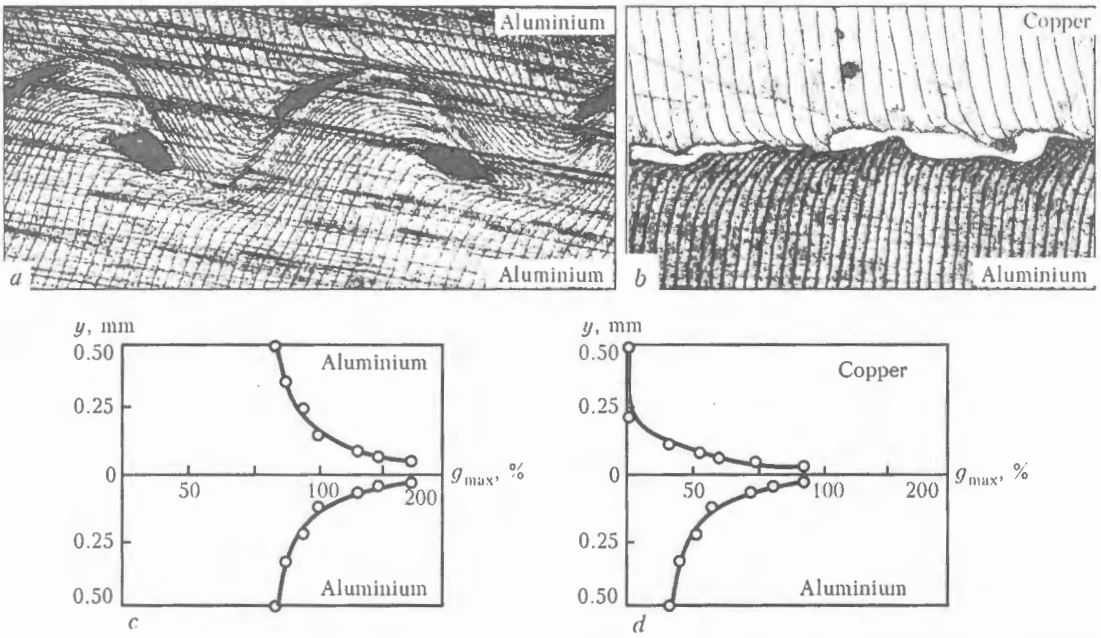

Figure 2. Macrostructure of laminar transverse model (*a*, *b*) and diagram of deformations (*c*, *d*) in explosion welding of similar (*a*) and dissimilar (*b*) metals at identical conditions (v_{cont} = 2000, v_c = 350 m/s) [10]

by a direct scheme (copper–flyer element). However, when the inverse scheme is used, the much higher part of the energy is generated in the flyer aluminium plate, exceeding the appropriate value in copper by more than 40 %, that is, probably, due to the additional deforming of less stronger aluminium plate subjected to double bending before collision.

Thus, for example, in welding by a direct scheme at conditions v_{cont} = 2600 m/s and v_c = 350 m/s approximately 0.46 MJ/m^2 is consumed for plastic deformation of HAZ metal of the aluminium element, 0.45 MJ/m^2 — of copper element (here, the design value W_2 = 0.78 MJ/m^2) [1]; in welding at the same conditions using an inverse scheme W_2^{Al} = = 0.56 MJ/m^2, for copper W_2^{Cu} — only 0.38 MJ/m^2.

Let us evaluate now the thermal situation in welded copper–aluminium joint, coming from the fact that almost all the energy consumed for plastic deformation of metal, will be transferred into heat [1–3 and oth.]. It is quite evident that the heat generated in copper and aluminium plates is proportional, respectively, to W_2^{Al} and W_2^{Cu}. Moreover, this heat is distributed over the entire sample across its thickness quite non-uniformly: its largest part is generated in near-contact layers of metals where the maximum deformations are realized and the larger part of the deformation energy is, respectively, consumed. From values of deformation energies in each layer of the welded joint of thickness Δy (Δy in our case is 0.03 mm), determined earlier from the relationships (1), (2), and, using the assumption that at some moment of time the heat, proportional to the energy consumed for deforming of each layer simultaneously in all the layers examined, it is not difficult to calculate in the first approximation the initial temperature fields in some section of bimetal.

Thus, for random i-th layer its temperature in the initial moment of time will be equal to

$$T_i = \frac{\Delta A_\partial}{C\Delta y\rho} + T_0 \qquad (3)$$

or

$$T_i = \frac{S_k\, \Delta y g_{max_i}}{C\Delta y\rho} + T_0 = \frac{S_k\, g_{max_i}}{C\rho} + T_0, \qquad (4)$$

where C is the specific heat content of metal; ρ is the metal density; T_0 is the initial temperature of elements being welded*.

The calculating distribution of temperature in copper–aluminium bimetal, welded at different conditions, is shown in Figure 3. Analysis of the relationships obtained showed that copper layers, located near the joining line, are heated to much higher temperatures than the aluminium layers adjacent to joining line (this is due to the difference in S_k and C for these materials). Here, the maximum values of temperature, determined by calculation-graphical method, of heating layers of near-contact volumes of explosion-welded metal have a tendency to increase in proportion to asymptotic approaching the joining line. Intensification of welding conditions causes the growth in values of maximum shears g_{max} near the joining line [3, 10, 11 and oth.], thus leading to heat generation in near-contact volumes of metal and, respectively, to the increase in their temperature.

Thus, it is quite evident that in explosion welding of copper with aluminium the appearance of molten metal regions at the interface of composite layers is

*It should be noted that relationship (3) is valid only for the case when the heat generated in some layer is insufficient for its heating up to the melting temperature. Otherwise, the addend with allowance for heat losses for melting should be added to (3).

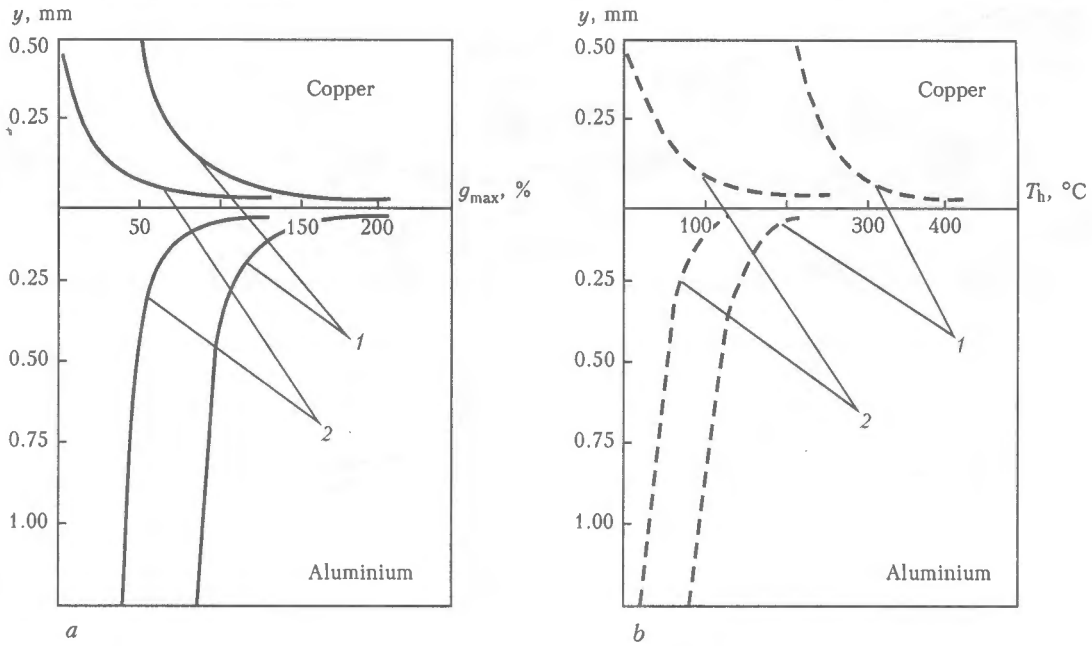

Figure 3. Diagrams of maximum shears (*a*) and distribution of temperatures (*b*) in section of explosion-welded copper–aluminium composite

due to the heat generated in a copper layer as a result of plastic deformation sufficient for melting the near-contact layers of the more fusible aluminium.

Let us compare the thermal situations in explosion welding of similar and dissimilar metals for the collision conditions characterized by the appearance in the latter of regions of molten metal at the joining interface. As initial data we shall use the diagrams of deformations plotted from experimental data of works [10, 11] for the case of explosion welding of copper with aluminium (v_{cont} = 2600, v_c = 350 m/s) using procedures [12], allowing accurate evaluation of maximum shears at the distance of not less than 30 μm.

Calculation of temperature values in HAZ using relationships (1)–(4) shows that in explosion welding of similar (aluminium) plates the layer, located at 30 μm distance from the joining line, is heated for not more than up to 150 °C, while in welding of copper plates the calculated value of temperatures is increased up to 650 °C, and the appearance of molten metal regions in both cases is not observed, as the temperature of near-contact layers is lower than the melting temperature of appropriate metals.

In explosion welding of copper with aluminium by the scheme, where a flyer element is copper, the values of HAZ temperatures, designed for the layer located at 30 μm distance from the joining line, are ≈ 450 and 150 °C, respectively, for copper and aluminium. However, at the interface of layers the regions of molten metal are observed that proves the reaching of higher temperature at the distance from the joining line of not less than 30 μm.

After solution of equation (4) relative to g_{max} and assuming that the aluminium melting temperature was reached in a near-contact layer, it is possible to evaluate the level of shear deformations at which the copper is heated up to the temperature of aluminium melting, it is about 350 %. Here the near-contact layer of aluminium is heated by its natural heat up to the temperature of not more than 250 °C.

The similar phenomenon is observed in explosion welding of steel with aluminium where such situation is realized in reaching some level of collision parameters, when the melts of pure aluminium are firstly formed in the weld. In this case, according to our arguments, the appearance of molten aluminium is due to the heat generated in near-contact layers of steel, whose temperature is higher than the aluminium melting temperature, but it is lower than the steel melting temperature. Intensification of welding conditions leads to the change in stoichiometric composition of the molten metal and the percent content of iron is increased in it. This indicates that such level of a shear deformation is attained at which the heat generated in steel is sufficient also for its melting.

Thus, the design-experimental method of evaluation of thermal situation in HAZ of explosion-welded dissimilar metals with quite different physical-mechanical properties makes it possible to explain the cause of formation of molten metal regions in welds at the conditions providing the defect-free zone of joining in case of explosion welding of similar metals, composing the composite.

CONCLUSIONS

1. It was established that approximately equal amount of energy is consumed for a shear deformation in explosion welding of similar and dissimilar metals. This regularity is preserved at varying the welding conditions within the wide ranges.

2. It is shown that in explosion welding of dissimilar metal with quite different physical-mechanical properties the appearance of molten metal regions at the interface of composite layers is due, first of all,

to the heat generating as a result of proceeding plastic deformation in more strong and refractory metal, sufficient for melting near-contact layers of the more fusible metal.

1. Sedykh, V.S., Sonnov, A.P. (1970) Calculation of energy balance of explosion welding process. *Fizika i Khimiya Obrab. Materialov*, **2**, 6–13.
2. Lysak, V.I., Sedykh, V.S. (1986) Influence of explosion welding parameters on kind of energy distribution in collision plates. In: *Transact. on Explosion Welding and Properties of Welded Joints*. Volgograd: VPI.
3. Kobelev, A.G., Lysak, V.I., Chernyshov, V.N. et al. (2002) *Manufacturing of laminated composite materials*. Minsk: Intermet Engineering.
4. Zakharenko, I.D. (1990) *Explosion welding of metals*. Minsk: Navuka i Tekhnika.
5. Kudinov, V.M., Koroteev, M.Ya. (1978) *Explosion welding in metallurgy*. Ed. by E.S. Karakozov. Moscow: Metallurgiya.
6. Khripunov, V.M., Pokataev, E.P. (2000) Calculation of thermal processes in explosion welding of dissimilar metals. In: *Transact. on Explosion Welding and Properties of Welded Joints*. Volgograd: VPI.
7. Berdychenko, A.A. (2000) On temperature distribution in near-weld zone during explosion welding. *Ibid*.
8. Pokataev, E.P., Khripunov, V.M., Pokataeva, V.M. (1998) Analytical investigation of thermal processes in explosion welded flat elements. *Ibid*.
9. Smelyansky, V.Ya., Ryskulov, M.T., Kozhevnikov, V.E. (1986) About problem of calculation of explosion welding conditions of dissimilar materials. *Ibid*.
10. Peev, A.P., Kuzmin, S.V., Lysak, V.I. et al. (2003) Features of plastic deformation of near-weld zone metal in explosion welding of copper with aluminium. *Fizika i Khimiya Obrab. Materialov*, **3**, 71–76.
11. Kuzmin, S.V., Lysak, V.I., Chugunov, E.A. et al. (2000) Welded joint formation in explosion welding of metals. *The Paton Welding J.*, **11**, 26–30.
12. Kuzmin, S.V., Lysak, V.I., Chugunov, E.A. et al. (2000) New procedure of investigation of near-weld zone metal produced by explosion welding. *Fizika i Khimiya Obrab. Materialov*, **2**, 54–60.

EFFECT OF CONTROLLING MAGNETIC FIELD ON TUNGSTEN ELECTRODE IN NARROW-GAP WELDING OF TITANIUM

V.Yu. BELOUS, V.P. PRILUTSKY and **V.N. ZAMKOV**
E.O. Paton Electric Welding Institute, NASU, Kiev, Ukraine

It has been established that in the case of using a welding torch, in which the shielding nozzle and collet are located over the gap, and only the tungsten electrode is introduced into the gap, the controlling magnetic field exerts a substantial force effect on the electrode. This circumstance should be taken into account, along with the value of the current load, to ensure reliable operation of the electrode.

Keywords: *TIG welding, narrow gap, tungsten electrode, magnetic field, magnetically impelled arc, deformation of electrode, electrode diameter*

Narrow-gap welding is the most efficient method for arc welding of metallic materials of medium and large thickness. It provides decrease in the number of passes required to make the weld, reduction in volume of the deposited metal and consumption of filler wire, and simplifies preparation of edges for welding. For titanium, considering its reactivity and high cost of titanium wire, such technological advantages of narrow-gap welding are especially important.

Narrow-gap argon-arc welding of titanium alloys is performed, as a rule, by using a non-consumable tungsten electrode [1–3]. There are two methods which can be employed for inert gas shielding of the welding zone.

In welding with the first method of shielding, the tungsten electrode is introduced into the gap together with a collet and shielding nozzle. With the second method only the tungsten electrode is introduced into the gap, while the shielding nozzle and collet are located over the gap [2]. Both methods have advantages and drawbacks.

The use of the first method leads to increase in the gap width and, therefore, decrease in the efficiency of the welding process. On the other hand, this causes a substantial decrease in a thermal load on the electrode, thus making the operating conditions for the electrode much easier and extending its service life. With the second method, width of the gap remains small and depends mostly upon the diameter of the tungsten electrode, although its operating conditions become much more difficult. For example, in welding titanium plates with thickness of up to 100–110 mm the tungsten electrode extension is L = 160 mm [2]. Therefore, it is important to estimate reliability of operation of the electrode under such conditions.

As established in the course of preliminary studies performed to select the tungsten electrode diameter for narrow-gap welding of titanium, when using the electrode with a diameter of 3 mm the alternating controlling magnetic field (frequency ν = 10 Hz, magnetic induction in the arc zone B = 9 mT) causes transverse oscillations of not only the welding arc but also the electrode. This initiated the first series of experiments to study behaviour of tungsten electrodes in narrow-gap magnetically-impelled arc welding. Tungsten electrodes of the EVI-2 grade with a diame-

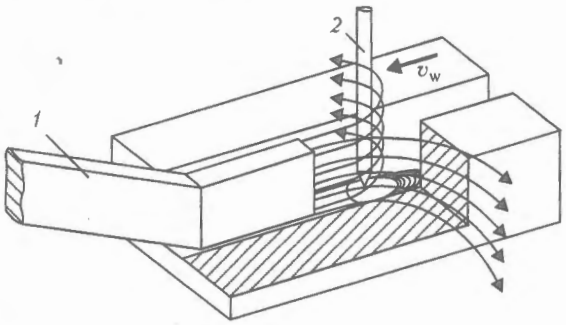

Figure 1. Flow diagram of the narrow-gap magnetically-impelled arc welding process: *1* — magnetic core; *2* — electrode

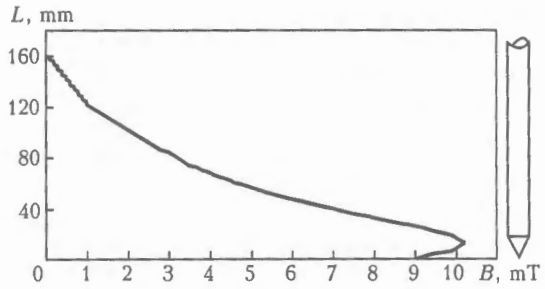

Figure 3. Distribution of root-mean-square value of magnetic induction B of the controlling magnetic field in plane ZOX along the tungsten electrode

ter of 3, 4 and 5 mm, having the identical pointing shape, were used for the experiments.

With this welding process, the tungsten electrode acts as a current conductor in the alternating magnetic field (Figure 1). It would be naturally to assume that oscillations of the electrode result from the Ampere force affecting it. It is well known that its values depend upon the current in the conductor and magnetic induction of the external magnetic field. In this case these are the welding current and magnetic induction of the controlling magnetic field, i.e. the technological parameters of the welding process. To determine whether the tungsten electrode of this diameter or the other is applicable for narrow-gap welding, it is necessary to determine dependence of spatial oscillations of the electrode upon these parameters.

Distribution of induction of the alternating controlling magnetic field along the electrode axis was found experimentally. This was done through determining the root-mean-square values of a radial induction component. Measurements were made by using the teslameter 43205 and primary measurement converter PIP-RAD, having the form of a flat probe. Magnetic induction was measured in axial plane ZOX of the electrode (Figure 2), starting from the tip (Z = = 0) and ending in a zone where the electrode leaves the water-cooled collet (L = 160 mm). The measurement results are shown in Figure 3. As the electrode tip is level with the lower end of the magnetic core, here we see some decrease in magnetic induction. Its maximum (B = 10.1 mT) is directly opposite the geometric centre of the magnetic core end (see Figure 2), where the distance from the magnetic core to electrode is minimal.

The electrode was watched during the welding process using a special optical system, allowing video filming it while the arc was burning. As shown by the experiments, transverse oscillations of the tungsten electrode under the effect of the controlling magnetic field take place even in a case where the welding current is much lower than its maximum permissible value for electrode of a given diameter. For example, for electrode of the EVI-2 grade with a diameter of 3 mm the permissible current load is 320 A. However, transverse oscillations of the electrode with an amplitude of 0.4 mm were fixed at a welding current as low as I_w = 150 A. In this case the electrode oscillates across the groove at a frequency equal to frequency of reversal of the controlling magnetic field. It should be noted that the magnetic induction values causing elastic deformation (oscillations) of the tungsten electrode decrease (Figure 4) with increase in the welding current (other conditions being equal).

When a constant or pulsed magnetic field is used instead of the alternating one, i.e. in the absence of change of the electromagnet poles, instead of oscillations we see gradual distortion (plastic deformation) of the electrode, occurring until it touches one of the gap walls (depending upon the magnetic induction direction).

In addition to elastic and plastic deformation in a transverse direction (across the weld axis), the electrode was found to bend also in a direction of the magnetic core. This occurs irrespectively of the direction of the magnetic induction vector. Magnetic induction along axis Y (see Figure 2) was determined to find the cause of deformation of the electrode in a longitudinal direction. As shown by the measure-

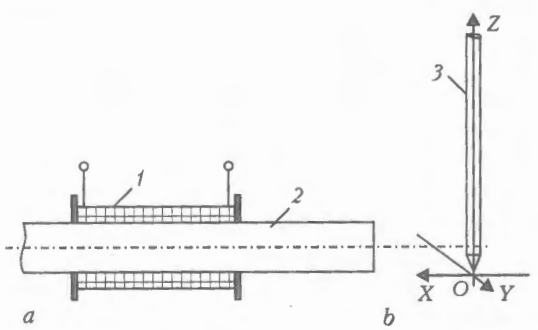

Figure 2. Schematic of relative arrangement of magnetic core (*a*) and electrode (*b*) in measurement of induction of the controlling magnetic field: *1* — solenoid; *2* — magnetic core; *3* — electrode

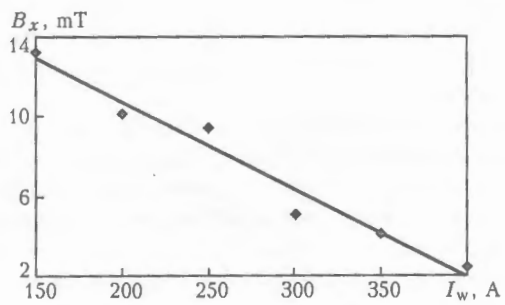

Figure 4. Variations in magnetic induction component B_x causing oscillations of the electrode tip with an amplitude of 0.4 mm at different values of welding current I_w

ments, magnetic induction along axis Y was $B_y = 0$ at all points on axis Z (Figure 5). Therefore, when the electrode is in a vertical position, the Ampere force affects it only in plane ZOY normal to the weld axis. As soon as the electrode deviates from the vertical axis, an additional component of the Ampere force, $\vec{F}_y$, appears. Direction of its effect (other conditions being equal) depends upon the direction of $\vec{B}_y$ (Figure 6). Force $\vec{F}_y$ causes the electrode to deviate in a direction of the magnetic core at the moment when it moves to an extreme vertical position under the effect of the force component $\vec{F}_y$ (see Figure 6).

Duration of the effect of force $\vec{F}_y$, its values and, hence, the degree of deformation of the electrode in a direction of the magnetic core depend upon the welding current, magnetic induction component B_y, weight and mechanical properties of the tungsten electrode, as well as peculiarities of operation of the device for magnetic control of the arc.

Therefore, the electrode with a diameter of 3 mm was found to bend in two directions, i.e. along and across the weld axis, its deformation persisting after welding. Moreover, deformation along the length of the electrode (Figure 7) is of an extremely non-uniform character. In the upper part of the electrode it begins at a distance of about 40 mm from the location where it leaves the water-cooled collet, whereas in the lower part of the electrode it occurs in a region 50–55 mm long, starting from the electrode tip. No residual deformations were fixed in this case. This character of variations in shape of the tungsten electrode is likely to relate to temperature conditions of its operation.

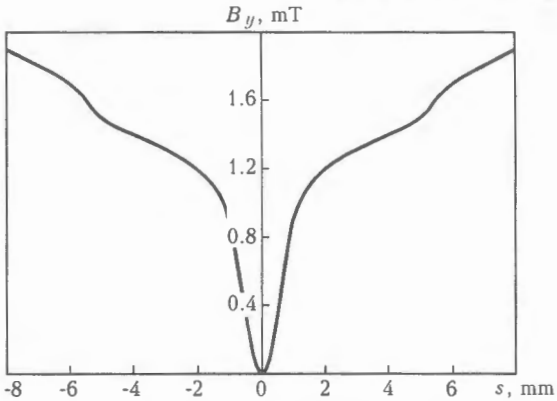

Figure 5. Distribution of magnetic induction component B_y of the controlling magnetic field in plane ZOY (s — distance from the weld axis)

As follows from [4], during welding the tungsten electrode 3 mm in diameter may be heated, depending upon the welding current value, to 2600–3200 K, which causes dramatic deterioration of its strength properties. For example, if at a normal temperature the elasticity modulus of tungsten is $\approx 40 \cdot 10^4$ MPa, at 2800 K its value decreases to $23 \cdot 10^4$ MPa [5]. Furthermore, the electrode during the welding process is heated non-uniformly along its length. According to the data of study [6], at $I_w = 300$ A the electrode with a diameter of 2.5 mm and 40 mm long is heated most intensively in its middle part, where the temperature may reach 3350 K. This character of distribution of temperature along the length of the tungsten

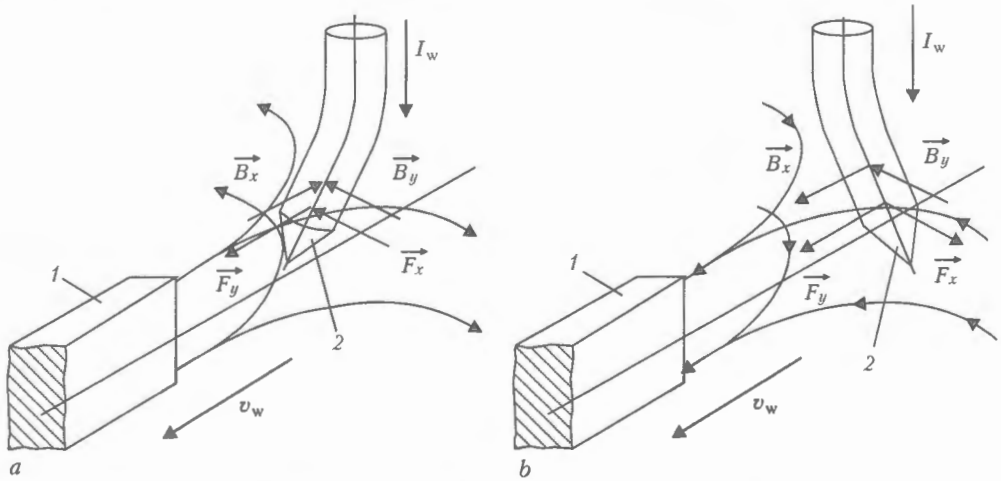

Figure 6. Directions of induction of the controlling magnetic field and Ampere force in transverse oscillations of electrode at its extreme left (*a*) and right (*b*) positions: *1* — magnetic core; *2* — electrode; B_x and B_y — components of magnetic induction in planes ZOX and ZOY, respectively; F_x and F_y — components of the Ampere force in the same planes

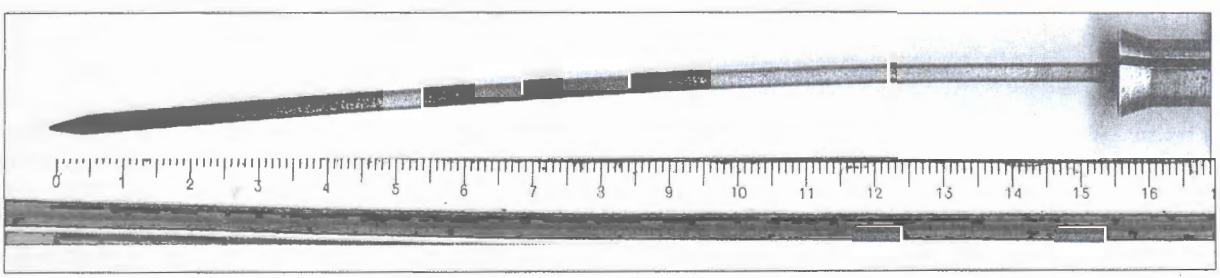

Figure 7. Appearance of the deformed tungsten electrode

electrode is attributable to the fact that its upper part is cooled due to removal of heat by the collet, whereas the lower part is cooled because of the so-called «electron cooling» effect at the thermionic arc cathode [4]. Therefore, the electrode is bent under the effect of the Ampere force in its hottest part. It can be assumed that as extension of the electrode increases, length of the overheated region in its central part also increases.

The ultimate current load for electrode of the EVI-2 grade with a diameter of 4 mm is 600 A. However, transverse oscillations of the electrode begin as low as at I_w = 400 A under the effect of the controlling magnetic field (ν = 10 Hz, B = 10 mT). After welding the tungsten electrode 4 mm in diameter exhibited no residual deformations. In the case of using electrode with a diameter of 5 mm, no deformation of the electrode was fixed at I_w = 450 A.

CONCLUSIONS

1. In narrow-gap magnetically-impelled arc TIG welding the tungsten electrode is affected by extra forces formed as a result of interaction of the welding current magnetic field and the controlling magnetic field.

2. Forces affecting the electrode during the welding process cause its elastic and even plastic deformation (depending upon the diameter), which violates spatial position of the electrode in the gap, decreases stability of arcing and deteriorates weld formation.

3. When selecting diameter of the tungsten electrode for narrow-gap magnetically-impelled arc welding, it is necessary to allow not only for the maximum permissible current for a given electrode grade, but also for the conditions needed to maintain the spatial position and shape of the electrode.

1. Matsui, S., Narayama, S., Sakurai, T. (1988) *Application of narrow-gap GTA welding to various products*. Osaka: JWS.
2. Paton, B.E., Zamkov, V.N., Prilutsky, V.P. (1996) Narrow-groove welding proves its worth on thick titanium. *Welding J.*, **4**, 37–41.
3. Grinin, V.S., Shtrikman, M.M. (1982) High-productivity automatic narrow-gap welding. *Svarochn. Proizvodstvo*, **7**, 21.
4. Dorodnov, A.M., Kozlov, N.P., Pomelov, Ya.A. (1973) The «electron cooling» effect at thermionic arc cathode. *Teplofizika Vys. Temperatur*, **11**, 724–727.
5. Savitsky, E.M., Povarova, K.B., Makarov, P.V. (1978) *Tungsten metals science*. Moscow: Metallurgiya.
6. Badianov, B.N., Davydov, V.A. (1994) Calculation of temperatures along the length of the tungsten electrode in argon-arc welding. *Svarochn. Proizvodstvo*, **1**, 34–35.

PECULIARITIES OF FORMATION AND CRYSTALLIZATION OF WELDS IN TIG WELDING WITH MAGNETIC ARC DEFLECTION

R.N. RYZHOV, V.S. SEMENYUK and **A.A. TITOV**
National Technical University of Ukraine «KPI», Kiev, Ukraine

Results of experimental study of the efficiency of application of longitudinal and transverse oscillations of arc, as well as non-reversing and reversing oscillation-rotation movements of arc for control of the processes of formation and crystallization of welds in non-consumable electrode welding are presented. The nature of experimental curves obtained allowed determination of the region of optimum values of parameters of arc deflection and formulation of recommendations for practical application.

Keywords: *TIG welding, electromagnetic systems, control magnetic field, arc deflection, parameters of formation and crystallization of welds*

Application of arc deflections in the process of welding is one of the methods of external pulsed actions on the processes of formation and crystallization of welds. This technological procedure is realized both by using mechanical and also electromagnetic devices. The latter are characterized by the simpler design schemes and improved dynamic characteristics of the arc movement. The quality of weld formation depends greatly on the amplitude, direction and frequency of arc deflections. The methods of welding are known in which the longitudinal and transverse oscillations of the arc, created by two-polar electromagnetic systems (EMS), are used to improve the parameters of formation and crystallization of welds [1, 2]. Here, the directions of arc oscillations in the process of welding were constant and determined by the EMS orientation with respect to the weld. The improvement of the above-mentioned technological procedures is possible by using hardware which will allow creation of the wider spectrum of characteristics of the arc deflection.

In the present work the control magnetic field (CMF) in the zone of welding was generated using EMS consisting of six electromagnets located at similar distance from the electrode under 60° angle one to another [3]. Using a specially-developed microprocessor device for control of electromagnetic actions (DCEMA) [4], the polarity, duration and periodicity of pulsed trains of magnetizing currents of each EMS coil were programmed. Here, the pulsed trains of du-

ration $t_{p.t}$ = 0.01–0.05 s consisted of 1–5 unipolar sinusoidal pulses of 0.01 s duration.

Arc was deflected in a preset direction by a radial CMF which was generated both by one and also by two EMS electromagnets, located one opposite another on the both sides from the electrode. Here, the magnetizing currents were of different polarities. Distance from edges of magnetic cores to the surface of samples was 5.5 mm, while the plane, in which a pair of electromagnets was located, was normal to the arc deflection direction. It was established during experimental determination of CMF parameters in the zone of welding that when magnetic fields of a pair of electromagnets are superimposed, the distribution of a radial component of induction B_y in the zone of arc burning is more uniform than in case of use of one electromagnet (Figure 1). Besides, to generate the CMF induction of a preset value in the zone of welding the lower magnetizing currents I_m were necessary, that improved the heat conditions of EMS system operation. At I_m up to 3 A, passed through one electromagnet, B_y varied within 0–5.5 mT ranges, while at generation of CMF by a pair of electromagnets — within 0–8.5 mT ranges. The further increase in magnetizing current led to the magnetizing of EMS cores and non-proportional increase in B_y.

It is known that the arc deflection is directly proportional to the amplitude value of the CMF radial component in the zone of welding. In the course of an experiment the phase control of currents through coils of electromagnets was realized by changing the angles of triggering of thyristors of the commutation block of DCEMA. Due to the low inductance of EMS coils the CMF pulses had here almost a vertical leading edge. At such shape of pulses the rate of arc movement at the beginning of cycles of deflection was very high that deteriorated the stability of its burning. In addition, with increase in angle of triggering of thyristors the duration of arc burning in natural conditions was increased, that reduced the efficiency of the actions studied. Therefore, in conductance of the main part of experiments the values of CMF inductance, and, consequently, also the arc deflections were adjusted by changing voltage in the primary winding of the DCEMA power transformer.

Experimental determination of dependence of arc deflection on magnetizing current, passing through EMS coils, was realized by record on a copper polished plate of the arc deflection radius $r_{a.d}$. Here, the arc current was I_a = 100 A, and its length l_a = 2 mm. To realize the oscillation-rotation movement of the arc, one pulse of magnetizing current was passed successively through each EMS coil. Stable results were obtained at arc burning during 0.12 s that corresponded to two its full rotations. It was established that in CMF generation by one electromagnet with increase in I_m from 0 to 8 A the values $r_{a.d}$ was increased exponentially from 1.2 to 2.3 mm, i.e. almost 2 times (Figure 2). At I_m = 3–8 A a negligible growth of $r_{a.d}$ can be explained by a negligible increase in a

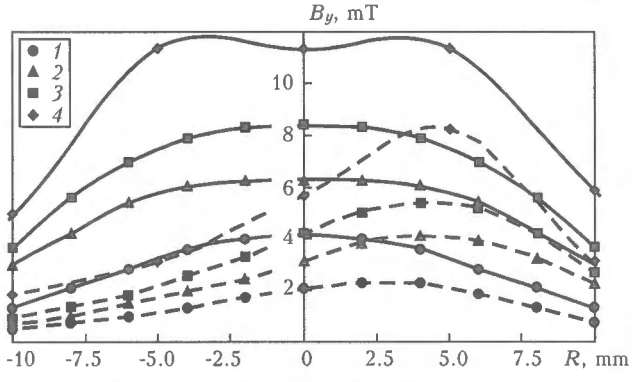

Figure 1. Distribution of a radial component of induction B_y in the zone of welding at CMF generation by one electromagnet (*dashed lines*) and a pair of electromagnets (*solid curves*): *1–4* — I_m = 1, 2, 3, 7 A, respectively; R — distance from longitudinal axis of EMS

radial component of CMF due to magnetization of EMS cores. In CMF generation by a pair of electromagnets with magnetizing current of opposite polarities the nature of relation $r_{a.d}(I_m)$ was not changed, but the arc was deflected by 40 % larger than in case of use of one electromagnet.

To determine the dependencies of parameters of formation and crystallization of welds on parameters of CMF arc deflection, 6 mm thick samples of steel 12Kh18N10T were welded without filler wire using the following condition: I_w = 100 A; U_a = 10 V; v_w = = 10 m/h. Experiments were performed at I_m = 3 A and $t_{p.t}$ = 0.01–0.05 s. Longitudinal and transverse oscillations of the arc were realized by changing the magnetizing current, passed through a pair of EMS poles, located in a plane normal to the directions of arc deflection, for opposite polarity through intervals of time $t_{p.t}$. Oscillation-rotation movement of arc was set by a series connection of one or a pair of opposite electromagnets with magnetizing currents of different polarities in the direction of arc rotation for time $t_{p.t}$. Reversing of arc rotation direction was realized through intervals of time $t_{r.a} = 6t_{p.t}$ by changing the sequences of connection of EMS electromagnets for opposite. Here, at the beginning of reversing cycle the arc was deflected to the direction of a longitudinal axis of weld to the side of a pool head part.

It was established that unlike the welding under the conventional conditions the periodic ripples are formed at all the examined types of arc movement over the surface of welds. This proves the proceeding of intensive hydrodynamic processes in weld pool. In all the cases with increase in $t_{p.t}$ the linear increase

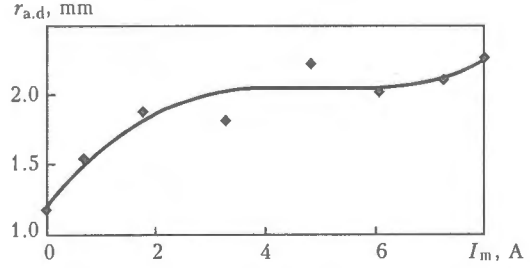

Figure 2. Dependence of arc deflection radius $r_{a.d}$ on magnetizing current I_m of EMS coils

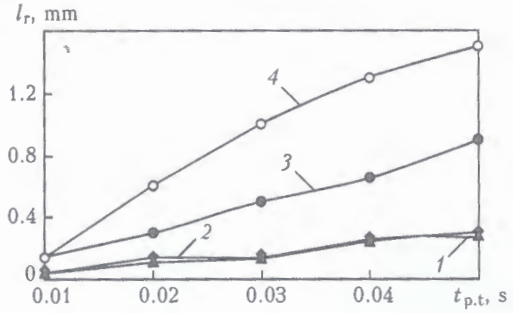

Figure 3. Effect of parameters of arc deflection on weld surface ripples: *1, 2* — longitudinal and transverse arc oscillations, respectively; *3, 4* — non-reversing and reversing oscillation-rotation movements of arc, respectively

in distance l_r between apexes of neighboring ripples were almost observed (Figure 3). Here, in case of longitudinal and transverse oscillations of the arc

$$l_r = v_w 2t_{p.t} \text{ (m)}.$$

At non-reversing oscillation-rotational arc movement

$$l_r = v_w 6t_{p.t} \text{ (m)}.$$

Reversing of direction of arc rotation leads to the 2 times increase in l_r. This can be explained by changing the time interval of formation of flows of melts directed to the side of the crystallization front, which is increased due to the necessity in delay of flows formed in a previous cycle.

It was determined experimentally that application of all the examined types of arc deflection with $t_{p.t}$ = = 0.01 s does not lead to significant changes in geometric characteristics of welds (Figure 4). In case of oscillation-rotation movements of the arc the depth of penetration was decreased by 17 % at an appropriate increase in the width of welds with increase in $t_{p.t}$ up to 0.05 s. This effect is explained by decrease in time

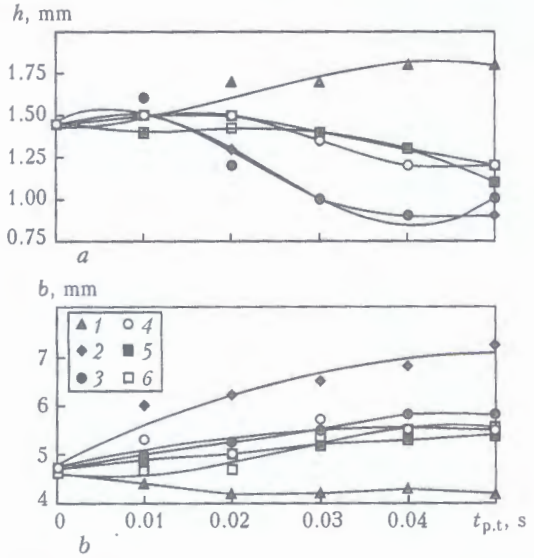

Figure 4. Effect of arc deflection parameters on geometric characteristics of welds: penetration depth h (*a*) and their width b (*b*): *1, 2* — longitudinal and transverse arc oscillations, respectively; *3, 4* — non-reversing and reversing oscillation-rotation arc movements at CMF generation by one electromagnet; *5, 6* — the same at CMF generation by a pair of electromagnets

during which the arc heated metal at one and the same place. Reversing of direction of arc rotation does not lead to significant changes in parameters of weld formation. At transverse oscillations the arc is located more often at lateral edges of the pool that explains the increase in width of welds by 56 %. However, here the heat dissipation is intensified through lateral surfaces of the pool to the parent metal, that is accompanied by decrease in penetration depth by 38 %. Hydrodynamics at longitudinal oscillations of the arc is featured by melt forcing out from a central region into head and tail parts of the pool, resulting in decrease of molten interlayer thickness under the arc and the process of parent metal melting occurs more intensively. This explains the increase in depth of penetration by 24 % with decrease in width of welds by 9 %. It should be noted that in all the cases the significant changes in parameters of formation of welds were observed at $t_{p.t}$ up to 0.04 s.

Using the arc deflection by the magnetic field it is possible to control effectively the process of crystallization of welds (Figure 5). As compared with a

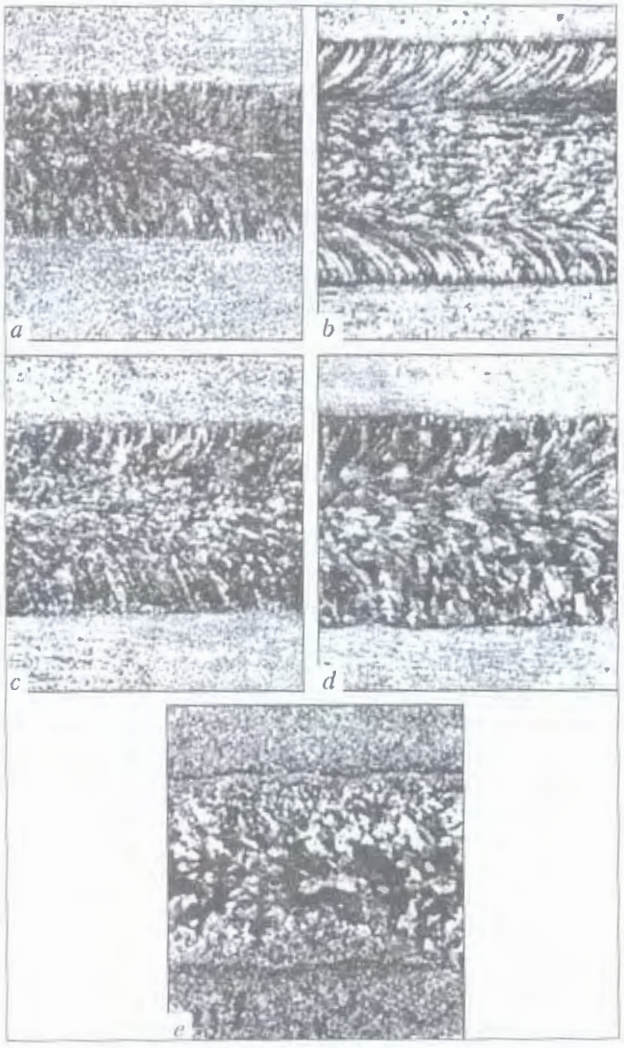

Figure 5. Primary structure of weld metal produced at different types of arc deflection: *a, b* — longitudinal and transverse arc oscillations, respectively; *c, d* — non-reversing and reversing oscillation-rotation movements of arc, respectively; *e* — without electromagnetic actions (×4)

primary structure of weld metal produced in welded under the conventional conditions (Figure 5, *e*) the highest structure refining was observed at longitudinal oscillations of arc along the entire section of welds and transverse oscillation in a central part of welds (Figure 5, *a, b*). This effect is explained by the fact that the above-mentioned actions are characterized by the highest frequency of arc movement in the direction of the crystallization front.

However, at these actions the schemes of crystallization are greatly differed. In case of longitudinal oscillations of arc the crystallites have a square shape and directed almost normal to the fusion line. At transverse oscillations of arc the zone of penetration consists of a central region, in which the direction of growth of crystallites is coincided with a longitudinal axis of weld and regions adjacent to the fusion line, formed of the larger crystallites of the arc-like shape. With increase in $t_{p.t}$ the width of a central zone is decreased and at $t_{p.t} = 0.05$ s the primary structure is formed only from the arc-shaped crystallites. The schemes of crystallization of welds, observed at transverse arc oscillations, prove that transverse movements of the pool head parts took place in the process of welding.

It was established by comparison of welds, produced in welding with non-reversing and reversing oscillation-rotational movements of the arc, that the more noticeable refining of weld metal structure is attained in the first case (Figure 5, *c, d*).

This effect can be explained the same as in case of formation of ripples at the weld metal surface by more stationary hydrodynamic processes proceeding in the pool. Moreover, the degree of structure refining is almost the same as in welds produced at longitudinal oscillations of the arc. However, the angle of binding the crystallites is smaller and the crystallites themselves have not a square, but arc-like shape that contributes to the increase in ductility of weld metal.

Unlike the welding in a non-reversing axial CMF [5] the application of non-reversing oscillation-rotation movement of the arc does not lead to a significant shifting from the longitudinal axis of line of binding lateral fronts of crystallization. Probably, in this case not rotational movements of metal flows, causing asymmetry of distribution of temperature at a lateral front of crystallization, are dominating in the pool hydrodynamics, but symmetrical flows in the directions from electrode axis to the pool edges.

It was established that increase in $t_{p.t}$ at all examined types of arc movement leads to the decrease in degree of weld metal structure refining. However, its characteristics remain much better as compared with welds produced by welding under the conventional conditions. Unlike the process of formation of welds for the process of crystallization the arc deflection is more effective by not one, but a pair of EMS electromagnets. This circumstance should be taken into account in programming of DCEMA operation conditions.

CONCLUSIONS

1. Application of a multipolar electromagnetic system with DCEMA in non-consumable electrode welding makes it possible to realize different types of a three-dimensional control of arc deflections using appropriate changes in direction, value and duration of arc deflection that is the effective method of effect on the process of formation and crystallization of welds.

2. Maximum changes in parameters of formation of welds in welding with arc deflections by the magnetic field are attained at $t_{p.t} = 0.03–0.05$ s, that is sufficient for the formation of melt flows in the direction from the pool center. Here, it is most effectively to use longitudinal and transverse oscillations of the arc to increase, respectively, the depth of penetration and width of welds.

3. The most favourable changes in primary structures of weld metal are observed at oscillation-rotation movement of the arc at the conditions characterized by the maximum frequency of pool melt displacement in the direction of the crystallization front.

1. Boldyrev, A.M., Tkachenko, Yu.S., Tolokonnikov, N.P. et al. (1975) Refinement of metal structure in welding with arc oscillated by transverse magnetic field. *Avtomatich. Svarka*, **7**, 70–71.
2. Zavialov, V.E., Ivantsov, V.Ya., Skornyakov, V.Ya. et al. (1979) Argon-arc welding of stainless steel pipes using magnetic fields. *Svarochn. Proizvodstvo*, **12**, 19–20.
3. Ryzhov, R.M., Malyshev, O.V. *Soldering iron for welding with external electromagnetic actions.* Pat. 42252A Ukraine. Int. Cl. 23 K 9/08. Publ. 15.10.01.
4. Titov, A.A., Malyshev, O.V., Ryzhov, R.M. *Method of non-consumable electrode welding with external combined controlled magnetic fields and device for its realization.* Pat. 50430 Ukraine. Int. Cl. B 23 K 9/08. Publ. 15.10.02.
5. Bardokin, E.V., Livenets, V.I., Okishor, V.A. et al. (1975) Structure and properties of weld metal in welding at low-frequency longitudinal alternating magnetic field. *Svarochn. Proizvodstvo*, **11**, 12–14.

PROPERTIES OF AUSTENITIC WELD METAL PRODUCED UNDER THE WATER

N.V. ZAJTSEVA[1], S.M. ZAKHAROV[1], S.Yu. MAKSIMOV[2] and I.V. LYAKHOVAYA[2]
[1]G.V. Kurdyumov Institute of Metal Physics, NASU, Kiev, Ukraine
[2]E.O. Paton Electric Welding Institute, NASU, Kiev, Ukraine

Welded joints on low-alloy steels of increased strength made underwater using electrodes with Cr–Ni alloy rods have been studied. The effect of the environment on gas saturation level and density of deposited metal, structure and properties of different zones in a welded joint has been evaluated. It is shown that the use of high-alloy electrodes makes it possible to increase ductility and strength of weld metal up to a level of those of the base metal.

Keywords: *underwater welding, coated electrodes, welded joint, chromium-nickel weld metal, structural constituents, gas saturation*

Despite the existing need for repair of metal structures of higher strength steels under the water, application of wet welding has so far been limited, because of unsatisfactory quality of welded joints. Coated electrodes are used for this purpose abroad [1]. Development of Hydroweld FS electrodes [2] in 1999 allowed recommending manual wet welding for restoration of the load-carrying capacity of critical structures, made of C–Mn steels with $C_{eq} \leq 0.4$.

Problem of welding higher strength steels with a high carbon equivalent is still unsolved. The main efforts to solve it are focused on development of electrodes with a rod of Ni-base alloys. However, no positive results have been reported. Preliminary experiments on welding with flux-cored wire with a nickel strip sheath [3], on the one hand, confirmed the possibility of producing a welded joint on higher-strength low-alloyed steel of X60 type without cracks in the HAZ metal and, on the other hand, revealed the difficulties associated with provision of the required level of mechanical properties. Presence of a large amount of hydrogen increases the plastic deformation resistance of weld metal and lowers the limit characteristics of its ductility.

Such a result is in agreement with the known susceptibility of nickel to hydrogen embrittlement [4]. In addition, this phenomenon becomes more noticeable in the presence of an oxygen impurity and higher cooling rate [4], which is characteristic for underwater welding conditions. In the opinion of the authors, oxygen presence in nickel facilitates intergranular fracture, which in this case proceeds at lower hydrogen concentrations, as the pressure of water vapours is added to hydrogen pressure, the water vapours forming at restoration of nickel oxides. In this case, cracking along the grain boundaries leads to sample fracture at tensile testing already at slight deformation.

In view of the above, it is of interest to study the hydrogen embrittlement of nickel alloys with iron and chromium. In [4] it is established that hydrogen embrittlement of nickel alloys with iron and chromium decreases with higher content of the latter. The authors associated such a nature of the influence of chemical composition with variation of electronic state of the alloys. Therefore, application of electrode materials for underwater welding, which provide a weld metal of Fe–Ni–Cr alloying system, may be more promising.

Electrodes with a stainless steel rod [5] were earlier recognized to be non-promising, because of the danger of cracking in weld metal near the fusion line, as a result of mixing with the base metal. Nonetheless, the authors of [6] report development of electrodes with a rod of Sv-10Kh16N25AM6 wire for underwater welding of high-strength steels, which provide sound welded joints with high mechanical properties and cold cracking resistance.

The purpose of this work was evaluation of the structure and mechanical properties of welded joints on 17G1S steel, made under the water with electrodes, providing an austenitic Cr–Ni deposited metal. Investigations were conducted by the methods of optical and scanning electron microscopy, X-ray phase and X-ray fluorescence analysis (FA), volumetry, gas analysis, optical spectroscopy, and also uniaxial tensile testing and hardness measurements were performed.

Test electrodes of 4 mm diameter with a stainless steel rod were made for investigations. Deposition was performed in a laboratory water tank at 1 m depth in the following modes: I_w = 140–160 A, U_a = 26–28 V, at reverse polarity current. 17G1S steel plates 14 mm thick, the composition of which is given in Table 1, were used as base metal.

Deposited metal has a sufficiently uniform structure and composition. Solidification results in predominant formation of a structure of columnar crystallites. Central nugget is much less pronounced than in a Ni-base weld [3]. No solidification cracks, coarse pores or shrinkage cavities were detected. No distributed porosity was found within the limits of resolution of the optical microscope. Dendrites and cells prevail

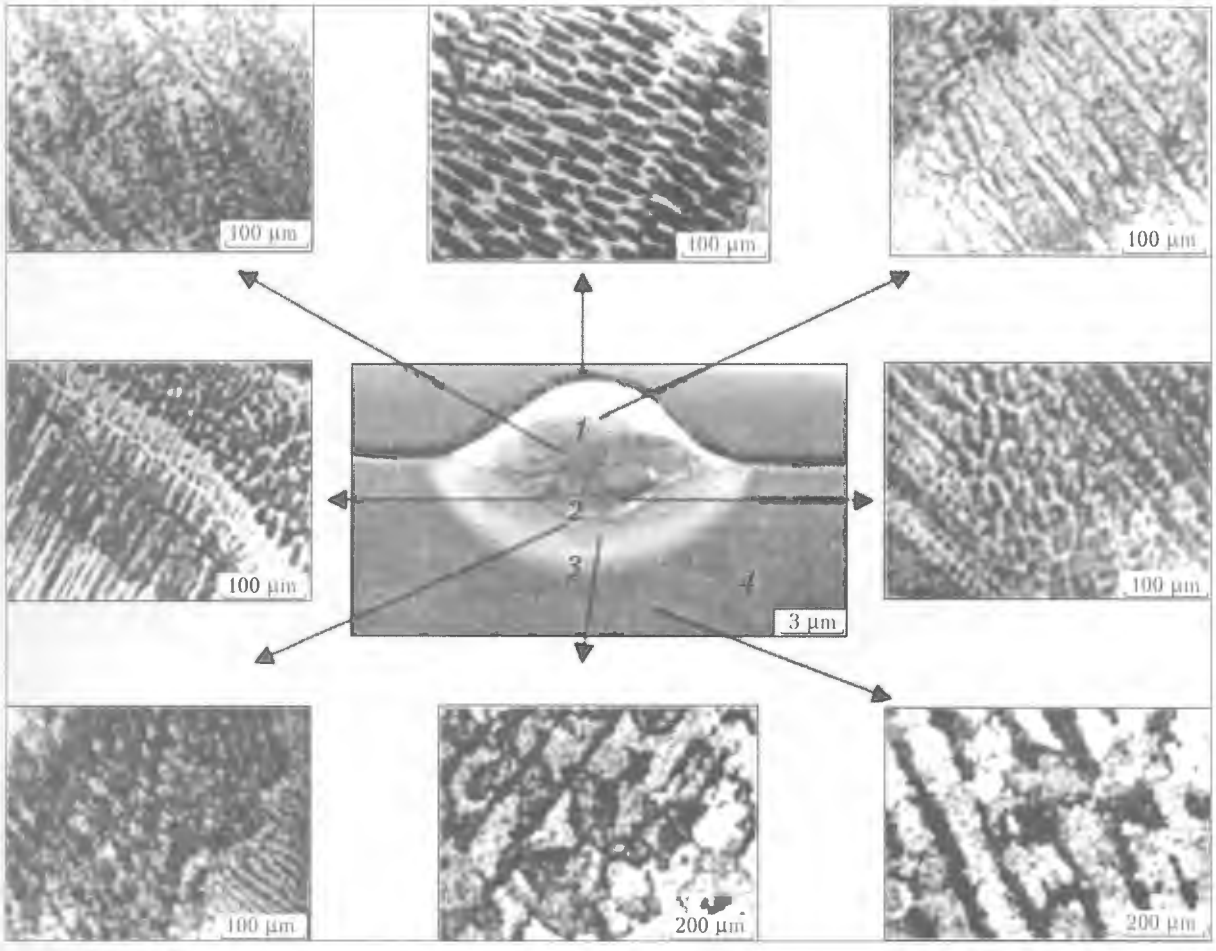

Figure 1. Microstructures of different sections of the deposit on 17G1S steel made under the water: *1* — deposited metal; *2* — transition zone; *3* — HAZ metal; *4* — base metal

in the deposited metal microstructure (Figure 1), which is indicative of significant concentration overcooling at deposited metal solidification [7].

Fusion zone and HAZ metal demonstrate a degradation of the lineage ferritic-pearlitic structure, characteristic of hot-rolled 17G1S steel, into a colony-type structure with a more uniform distribution of cementite, which leads to a higher hardness of this zone (Figure 2). No cracks were found in the HAZ metal.

X-ray phase analysis reveals a predominantly uniform fcc solid solution of a variable composition across the deposit, which corresponds to the data of chemical analysis (see Table 1), and ternary Fe–Ni–Cr phase diagram [8]. Reflexes of carbide phases cannot be reliably determined, which together with the results of microstructural studies allows neglecting the influence of carbide strengthening.

Table 1. Composition of steel 17G1S and deposited metal, wt.% (FA)

Analyzed zone	*Fe*	*Ni*	*Mn*	*Cr*	*Mo*	*Si*	*C*
Deposit center	62.80	14.70	5.00	14.20	2.80	0.50	–
Fusion zone	77.78	8.74	3.85	7.32	1.86	0.45	–
Base metal*	97.59	0.10	1.67	0.10	–	0.36	0.18

*Optical spectral analysis.

Compared to Ni-base weld metal [3] oxygen content rose several times in the studied sample, while the residual hydrogen content remained at the same level (Table 2). In this case, the density of the deposited metal was markedly increased. Absence of macrodefects is confirmed by the results of metallographic investigations.

Obtained data suggest that simultaneous alloying with nickel and chromium will be positive for mechanical properties of weld metal, for determination of which the butt joints were made in the above modes.

Fracture of the studied sample after achievement of residual deformation of more than 30 % (Table 3) is accompanied by necking. Fractographic pattern

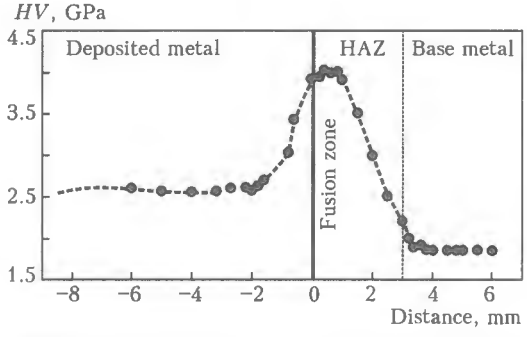

Figure 2. *HV* microhardness distribution across the deposit section near the fusion zone

Table 2. Gas content and value of deposited metal density

Alloying system	Gas content, wt.%·10^{-2}		Density, g/cm^3		$\Delta\rho = \rho_c - \rho_m$, g/cm^3	$\Delta\rho/\rho_c$, %
	[O]	[H]	measured ρ_m	calculated ρ_c		
Nickel	0.71	0.36	8.3789	8.5711	0.1922	2.242
Nickel + chromium	4.80	0.36	7.9545	8.0011	0.0466	0.580

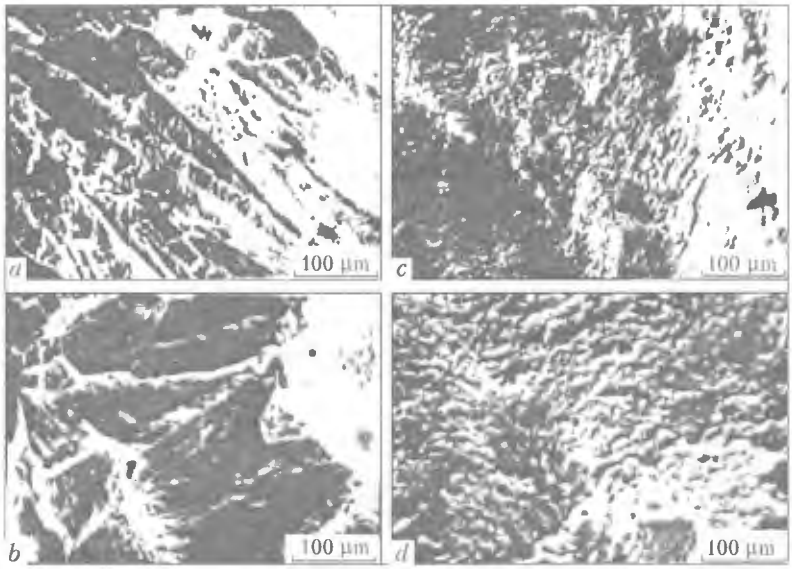

Figure 3. Fractograms of fractures after stretching weld metals made under the water: *a, b* — alloying with nickel; *c, d* — chromium and nickel alloying

Table 3. Mechanical properties of weld and base metal

Material	$\sigma_{0.2}$, MPa	σ_t, MPa	δ, %	ψ, %	E, MPa
Weld	410	626	34	38	15384
17G1S steel [7]	340	510	23	–	17000

characterizes the fracture as tough fracture (Figure 3), which confirms the general statement of the absence of coarse defects, i.e. fracture initiators in this case. For comparison, the same Figure gives fractograms of fractures in a sample of nickel weld metal, where the cleavage fraction exceeds 50 %. Mechanical properties of the deposited metal are in a good agreement with those of base metal (Table 3), which is necessary to ensure the operational reliability of the welded joint.

Thus, the conducted investigations showed that application of electrodes with a rod of a Cr–Ni alloy provides a uniform austenitic structure of the deposited metal without macroscopic defects, and promotes a higher ductility and strength of weld metal up to the level of properties of base metal, namely higher-strength low-alloyed steel.

1. Ibarra, S., Grubbs, C.E., Liu, S. (1994) State-of-the art and practice of underwater wet welding of steel. In: *Proc. of Int. Workshop on Underwater Welding of Marine Structures*, New Orleans, Dec. 7–9, 1994.
2. Pett, M. (1998) Wet (underwater) welding becomes a viable option. *Welding Met. Fabr.*, 66(**4**), 12–14.
3. Maksimov, S.Yu., Savich, I.M., Zakharov, S.M. et al. (2003) Structure and properties of metal deposited under the water by flux-cored wire with a nickel sheath. *The Paton Welding J.*, **4**, 18–21.
4. Moroz, L.S., Chechulin, B.B. (1967) *Hydrogen brittleness of metals*. Moscow: Metallurgiya.
5. Bailey, N. (1991) Welding under water — a metallurgical appraisal. In: *Proc. of 1st Int. Offshore and Polar Engineering Conf.*, Edinburg, Aug. 11–16, 1991. Vol. 4.
6. Maslennikov, P.S., Russo, V.L. (2000) New electrodes for underwater welding. *Svarochn. Proizvodstvo*, **11**, 26–27.
7. Prokhorov, N.N. (1968) *Physical processes in metals during welding*. Vol. 1. Moscow: Metallurgiya.
8. (1986) *Constitutional diagrams of binary and multicomponent iron-base systems*. Refer. Book. Ed. by O.A. Bannykh. Moscow: Metallurgiya.

COMPARISON OF IMPACT TOUGHNESS VALUES OF CHARPY AND MESNAGER SPECIMENS AT TOUGH FRACTURE

V.P. DYADIN
E.O. Paton Electric Welding Institute, NASU, Kiev, Ukraine

Approach to analytical comparison of the tough fracture energy of Mesnager and Charpy specimens and their components is considered. Simple relationship is suggested allowing the values of impact toughness of the Charpy specimens to be determined from the results of testing the upper shelf of Mesnager specimens.

Keywords: *welded joint, impact toughness, specific energy, Charpy and Mesnager specimens, fibre content in the fracture, strain ageing, upper shelf*

New approaches developed at PWI for determination of fracture toughness characteristics (K_{Ic} , δ_{Ic}, T) by the results of standard testing of Charpy specimens [1–4], allow a much wider practical application of fracture mechanics criteria in design and strength analysis of structures. In this connection particularly urgent is the problem of transition to acceptance testing of Charpy specimens of structural materials instead of Mesnager specimens, which will allow, on the one hand, harmonizing the local standards with the European and US norms for fabrication of structural steels and, on the other, developing scientifically substantiated requirements to admissible maximum values of impact toughness of base metal and welded joints, required for provision of structure reliability.

In local practice mandatory determination of impact toughness was until recently performed on Mesnager specimens, which required conducting additional testing of Charpy specimens. The latter is not always possible to implement in practice, particularly, for equipment, which is already in operation.

This paper is an attempt to use the existing experimental and correlation dependencies, obtained for specific energy of fracture of standard Charpy and Mesnager impact toughness specimens to analyze the possibility of existence of a stable connection between them.

Work in this area can be divided into two groups. The first includes investigations, aimed directly at correlation of impact toughness of standard specimens with concentrators of different sharpness. The second covers investigations, indirectly related to the considered problem, but including the results of studying the general regularities of the energies of initiation a_{in} and propagation a_{pr} of fracture in impact bending tests.

A considerable number of publications are devoted to an experimental method to establish correlations between the results of impact testing of these types of specimens, some of them being particularly interesting. In study [5] results of studying low-alloyed steels of six grades (09G2S, 10G2S1, 10KhSND, 15KhSND, 16G2AF) with sheet thickness of 20 and 30 mm (GOST 19282–73) and 12GN2MFAYu steel with sheet thickness of 12 mm (TU 14-1-1772–76), as well as their welded joints made with Sv-10NMA, Sv-08GA and Sv-08KhN2GMYu wires were used to derive the following dependence:

$$a_V = (1.6 \cdot 10^{-5}) a_U^3 - (1.5 \cdot 10^{-3}) a_U^2 + (4.8 \cdot 10^{-1}) a_U, \quad (1)$$

where a_V and a_U is the impact toughness determined on standard specimens made to GOST 9454–78 of type 11 and 1, respectively. Figure 1 shows the testing results. Here each point corresponds to values of impact toughness at a certain testing temperature.

As is seen from Figure 1 suggested dependence (1) in the transition region of brittleness yields unjustifiably higher (4 to 5 times) values of impact toughness

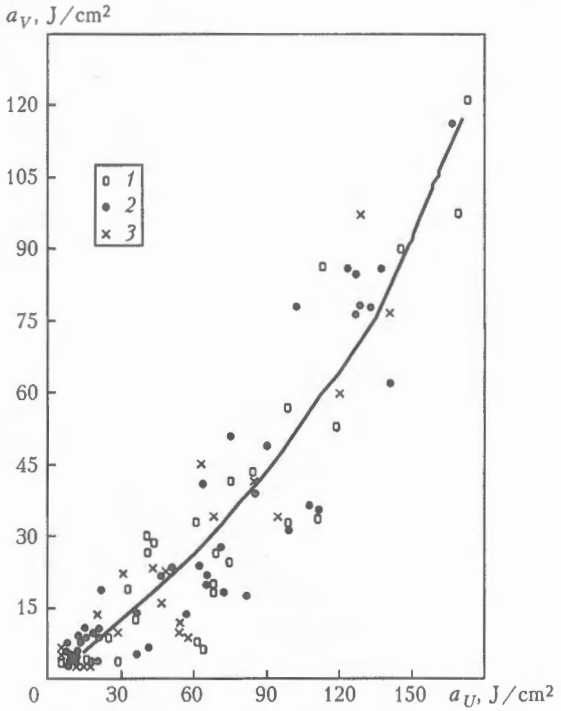

Figure 1. Correlation dependence (1) between impact toughness of Charpy and Mesnager specimens [5]: *1* — base metal; *2* — weld metal; *3* — HAZ metal

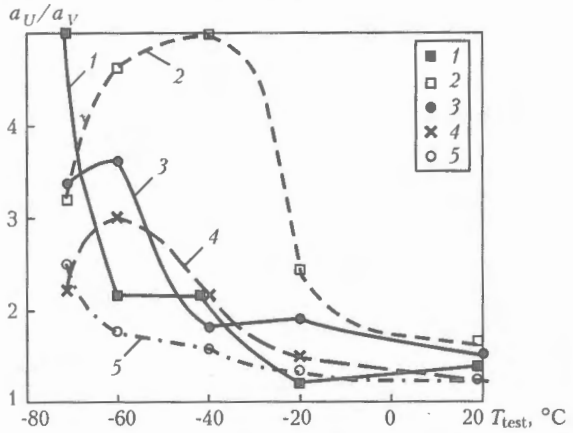

Figure 2. Change of the ratios of minimum values of impact toughness a_U/a_V of standard Mesnager and Charpy specimens depending on testing temperature: *1* — 14G2AFD steel; *2* — 15KhSND; *3* — 12G2MFT; *4* — 15G2AFD; *5* — 10KhSND

a_V, which may lead to considerable error in calculation of admissible stresses in structural elements in terms of fracture mechanics [1–4].

The latter is confirmed in [6], where it is proved that notch sensitivity in the studied low-alloy steels rises with temperature lowering, the degree of the increase depending on the steel grade. Values of impact characteristics decrease with temperature increase (Figure 2). Based on the obtained data the authors of [6] came to the conclusion that it is impossible to establish one transition coefficient K, having the form of $a_V = Ka_U$. In all probability, this is related to a number of factors, the main of which are disturbance of the condition of plane deformation in testing of Mesnager impact specimens in the transition temperature region. Results of impact testing of specimens at brittle fracture demonstrated that relative variation of the ratio of impact characteristics should also decrease with decrease of the energy of crack initiation. This follows from a more detailed analysis of testing results [6] at comparison of the nature of variation of minimum values of impact toughness, depending on temperature (see Figure 2).

A simpler correlation dependence, connecting variation of impact toughness values of standard Charpy and Mesnager specimens, is given in study [7]:

$$a_U = 1.2a_V + b_{av}, \qquad (2)$$

where $b_{av} = 32.5$ J/cm^2. The author believes that dependence (2) can be used to describe the entire set of experimental data (more than 15 grades of low-alloyed steels have been studied) with abmodality $\Delta b = \pm 25.5$ J/cm^2.

A similar correlation dependence is suggested in study [8], which describes the results of studying hull sheet steels of grades R44-4a and R52-6a.

It should be noted that dependencies of type (2) have limited application. This is related to the fact that the authors introduce a limitation on impact toughness values of Mesnager specimens — $a_U \geq 32.5$ J/cm^2. In addition, the above correlation dependencies were constructed on the basis of processing and analysis of average values of impact bend testing results, which introduces an additional error in evaluation of their minimum values.

When new methods for determination of steel performance are sought, division of impact toughness into components is often used [9–15]. It is mostly believed that impact toughness a consists of two components, which reflect the main stages of the fracture process: $a = a_{in} + a_{pr}$. Some authors [9, 10] believe that impact toughness of a specimen with a fatigue crack is the energy of fracture propagation, i.e. $a = a_{pr}$. However, as noted in [11], the difference between the values of energy a_{pr}, determined by the procedures of [9, 10], is equal to 20–30 %. This is, apparently, related to the fact that the accepted straight-line relationship of impact toughness and notch radius is not always in place. This is confirmed in [12], which shows that in the region of notches with rounding-off radius less than 1 mm a discrete transition from the tough to brittle fracture is observed in a number of cases.

A.S. Rakhmanov and L.S. Livshitz [13] suggested a different approach to division of impact toughness, as they believed that the specimen is only deformed first (energy of deformation), and then only fails (energy of fracture). Works [14, 15] are also interesting in terms of physical understanding of the process of impact specimen fracture.

Special mention should be made of research performed by the Physico-Mechanical Institute of the NAS of Ukraine into the influence of structural parameters on the energy of fracture initiation in the zones of stress raisers of different sharpness [16].

The above studies reflect the main approaches to establishment of possible links both for total impact energy of fracture between different impact testing specimens and for its components. Obtained results suggest the following.

It is first of all anticipated that the ratio of specific energy of fracture of impact testing specimens with different stress raisers should depend on fracture mode (tough, mixed or brittle). The leading role particularly in the case of relatively «soft» stress raisers will be played by the conditions of initiation of a particular mode of fracture and specific energy consumed by this process, respectively.

In the case, if fracture propagates by a mixed mechanism (quasi-brittle), the ratio of total energy of fracture of Charpy and Mesnager specimens can significantly differ primarily because of the fact that at the initial stage the crack in a Mesnager specimen propagates under less severe conditions. This is indicated by the difference in the nature of decrease of impact toughness values, depending on fibre content in fractures of Mesnager and Charpy specimens in the transition region of temperatures, which it is rational to take into account, when establishing the respective correlation links.

Further difficulties are also related to the fact that in the transition region of temperatures fracture in-

itiation is of a mixed nature. In this case, as noted by T.A. Vladimirsky [12], a bimodal «jump-like» variation of the energy of fracture is observed. The temperature at which this phenomenon proceeds depends mainly on disturbance of the condition of plane deformation. It is natural that these processes proceed in a different manner for specimens with different sharpness of the notch. While in Charpy specimens the «jump-like» change of the energy of fracture is manifested only slightly and for engineering purposes it can be approximated by one temperature curve of impact toughness, a pronounced salient point of this curve is found in Mesnager specimens [12]. The latter calls into doubt the possibility of establishing a single correlation and analytical link in the entire temperature range for Mesnager and Charpy impact testing specimens.

However, as at initiation of a tough fracture the volumetric nature of the stressed state near the notch should not have a significant role, it may be anticipated that the energy of a tough crack initiation will depend on the concentration of plastic deformations at the notch tip in a specimen. In this case existence of rather stable links between the energy of initiation of a tough crack in specimens of different types is quite admissible. If in this case the energy of fracture propagation, related to fractographic features of fractures, does not have any significant differences, this assumption may be also extended to total specific energy of specimen fracture. The available results [6] (see Figure 2) are exactly a confirmation of this assumption in terms of quality.

Proceeding from modern concepts, the processes of initiation and propagation of a tough fracture are characterized by different features of material crack resistance. In the first case, these may be deformation characteristics of fracture mechanics, in the second — critical angle of opening of a tough crack, T. Considering further that the critical angle of opening of a tough crack, T, is determined by the ratio of crack tip opening displacement δ_{1c} and size of prefracture zone [3], it becomes possible to derive an analytical expression of total energy of fracture of impact testing specimens with different rounding-off radii through the deformation characteristic of fracture toughness [4].

In the first stage let us consider the solution of this problem in the quasistatic definition.

As was noted in [17], Neuber ratio, according to which the product of the coefficients of stresses and strains in the non-linear region is equal to a square of elastic stress concentration, can be used for analysis of the conditions of tough fracture of a Charpy specimen. Critical deformation and angle of bending θ_{1c} of a Charpy specimen at the moment of a tough crack initiation are described by the following relationship:

$$(\varepsilon_f/\varepsilon_y)^{1+n} = K_V^2(1 + 4r^*/\rho_V)^{-1}\,[\theta_{1c}/(3\varepsilon_y)]^{1+n}, \quad (3)$$

where ε_f is the critical local plastic deformation at distance r^* from the tip of a notch in a Charpy specimen (in [17] value r^* is taken to be equal to the characteristic dimension of the structural element — 0.06 mm); ε_y is the deformation corresponding to the yield limit; K_V is the coefficient of elastic stress concentration at the tip of a notch in a Charpy specimen equal to 3.44 [18]; ρ_V is the notch radius in a Charpy specimen equal to 0.25 mm; n is the strain ageing of a material.

In this case after determination of bending moments under the condition of total yield and fracture propagation, the specific energy of fracture initiation in a Charpy specimen and specific energy of tough crack propagation allowing for [2], can be written as the following dependencies [17]:

$$a_V^{in} = [\theta_{1c}/(3\varepsilon_y)]^{1+n}(B - L)k_1 3\varepsilon_y\sigma_{0.2}/[4(1 + n)], \quad (4)$$

$$a_V^{pr} = [\theta_{1c}/(3\varepsilon_y)]^n(B - L)k_2\sigma_{0.2}(\sigma_t/\sigma_{0.2})n/[4(1 - n)^2], \quad (5)$$

where a_V^{in} is the specific energy at the moment of fracture initiation in a Charpy specimen under static loading; a_V^{pr} is the specific energy of a tough crack propagation in a Charpy specimen; $(B - L)$ is the height of the specimen under the notch equal to 8 mm; k_1 is the constraint coefficient for a Charpy specimen equal to 1.25 [9]; k_2 is the mean constraint coefficient for a Charpy specimen at the moment of fracture initiation equal to 1.26.

Approaches used to derive these dependencies, may be applicable also for analysis of fracture of a Mesnager specimen. In view of the fact that the coefficient of elastic stress concentration at the tip of a Mesnager specimen $K_U = 2.1$ [18], and the rounding-off radius is 1 mm, Neuber ratio for a Mesnager specimen can be written as

$$(\varepsilon_f/\varepsilon_y)^{1+n} = K_U^2(1 + 4r^*/\rho_U)^{-1}[\theta_{2c}/(3\varepsilon_y)]^{1+n}, \quad (6)$$

where θ_{2c} is the critical angle of bending of a Mesnager specimen at the moment of a tough crack initiation.

Assuming that fracture initiation should proceed at the same deformations in a certain volume of the material (in this case it is assumed to be equal to r^*), from the equality of left-hand parts of dependencies (3) and (6) it is possible to establish a connection between the critical angles of bending of Mesnager and Charpy specimens:

$$\theta_{2c}/\theta_{1c} = [(K_V^2(1 + 4r^*/\rho_U))/(K_U^2(1 + 4r^*/\rho_V))]^{1/(1+n)}. \quad (7)$$

Considering that the constraint factor for a Mesnager specimen $k_3 = 1.225$ [19], the specific energy of initiation can be expressed by the following dependence:

$$a_U^{in} = [\theta_{2c}/(3\varepsilon_y)]^{1+n}(B - L)k_3 3\varepsilon_y\sigma_{0.2}/[4(1 + n)]. \quad (8)$$

Allowing for (7) the ratio of specific energies of fracture initiation in Mesnager and Charpy specimens becomes

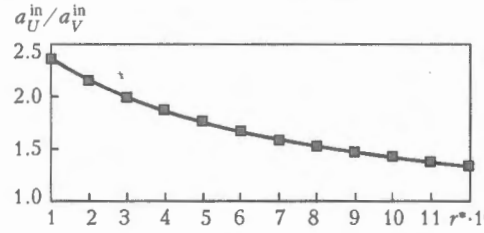

Figure 3. Change of specific energy of tough fracture initiation in Charpy and Mesnager specimens depending on structural element r

$$a_U^{in}/a_V^{in} = (k_3/k_1)(K_V/K_U)^2(1 + 4r^*/\rho_U)/(1 + 4r^*/\rho_V). \quad (9)$$

As is seen from (9), the ratio of specific energy of tough fracture initiation in Mesnager and Charpy specimens depends only on the dimensions of structural element r^*. Dependence of the ratio of specific energies of tough fracture initiation in Charpy and Mesnager specimens on r^* derived from (9), is shown in Figure 3.

The next step in determination of an analytical relationship between fracture energies of Charpy and Mesnager specimens is consideration of specific energy of a tough crack propagation in specimens of these types under static loading. In this case the critical angle of opening of a stable crack is used for analysis of tough fracture propagation as a criterion of material resistance to tough crack propagation [2]. The fact that its value remains practically constant at a stable propagation of the crack considerably facilitates the solution of this problem and allows the energy of fracture propagation in a Charpy specimen to be described by (5).

As is seen from this expression, specific energy of fracture propagation depends on a critical angle of specimen bending, corresponding to the moment of fracture initiation. It follows that expression (5) can also be used for analysis of the energy of propagation of a tough fracture of a Mesnager specimen:

$$a_U^{pr} = \\ = [\theta_{2c}/(3\varepsilon_y)]^n(B - L)k_2\sigma_{0.2}(\sigma_t/\sigma_{0.2})n/[4(1 - n)^2]. \quad (10)$$

Allowing for (7) it follows from (5) and (10) that

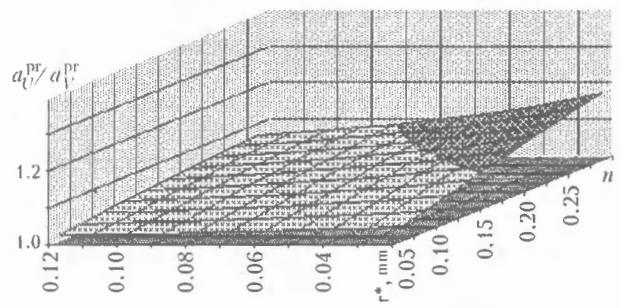

Figure 4. Change of specific energy of tough fracture initiation in Charpy and Mesnager specimens, depending on structural element r and strain ageing n, according to (11)

$$a_U^{pr}/a_V^{pr} = \\ = [(K_V/K_U)^2(1 + 4r^*/\rho_U)/(1 + 4r^*/\rho_V)]^{n/(1+n)}. \quad (11)$$

As is seen from (11), the ratio of specific energies of propagation of tough fracture in Charpy and Mesnager specimens depends on the coefficients of concentration of elastic stresses in the tips of notches and dimension of structural element r^*. As regards determination of the characteristic dimension of structural element r^* it is necessary to take into account a certain conditionality, related to uncertainty of the notion of «tough fracture initiation», which may include different stages of material continuity, starting with formation of individual microcracks or pores and their systems and up to development of a macroscopic crack, recorded experimentally in material testing for crack resistance. In these cases the dimensions of such defects are small and for the majority of structural steels and their welded joints they are from 40 up to 120 μm.

Considering that the characteristic of strain ageing of a material $n < 0.25$, right-hand part of equation (11) is close to 1.0 (Figure 4). This confirms the approximate equality of specific energy of tough fracture propagation in Mesnager and Charpy specimens.

Proceeding from dependencies (4), (5) and (8), (10) total energy of fracture of Charpy and Mesnager specimens, respectively, can be expressed through their specific energy of fracture propagation:

$$a_V = a_V^{in} + a_V^{pr} = \\ = a_V^{pr}[(k_1/k_2)(\sigma_{0.2}/\sigma_t)[(1 - n)^2/(n(1 + n))]\theta_{1c} + 1]; \quad (12)$$

$$a_U = a_U^{in} + a_U^{pr} = \\ = a_U^{pr}[(k_3/k_2)(\sigma_{0.2}/\sigma_t)[(1 - n)^2/(n(1 + n))]\theta_{2c} + 1]. \quad (13)$$

Allowing for (7) and (11) relationships, specific energy of tough fracture propagation in Charpy and Mesnager specimens under static loading can be written as follows:

$$a_U/a_V = \left[\frac{K_V^2}{K_U^2}\frac{1 + 4r^*/\rho_U}{1 + 4r^*/\rho_V}\right]^{\frac{n}{1+n}} \times \\ \times \frac{\frac{k_3\sigma_{0.2}(1 - n)^2}{k_2\sigma_t n(1 + n)}\left[\left(\frac{K_V^2}{K_U^2}\frac{1 + 4r^*/\rho_U}{1 + 4r^*/\rho_V}\right)^{\frac{1}{1+n}}\theta_{1c}\right] + 1}{\frac{k_1\sigma_{0.2}(1 - n)^2}{k_2\sigma_t n(1 + n)}\theta_{1c} + 1}. \quad (14)$$

From dependence (6) and study [2] (in this case ε_f is taken to be the deformation, corresponding to loss of plastic stability of a material) it follows that

$$\theta_{1c} = [3n/(1 - n)][(1 + 4r^*/\rho_V)/K_V^2]^{1/(1+n)}. \quad (15)$$

Substituting (15) into expression (14), we have

$$a_U/a_V = \left[\frac{K_V^2}{K_U^2}\,\frac{1+4r^*/\rho_U}{1+4r^*/\rho_V}\right]^{\frac{n}{1+n}} \times$$

$$\times \frac{\frac{3k_3}{k_2}\left(\frac{1+4r^*/\rho_U}{K_U^2}\right)^{\frac{1}{1+n}} + \frac{\sigma_t(1+n)}{\sigma_{0.2}(1-n)}}{\frac{3k_1}{k_2}\left(\frac{1+4r^*/\rho_V}{K_V^2}\right)^{\frac{1}{1+n}} + \frac{\sigma_t(1+n)}{\sigma_{0.2}(1-n)}}. \qquad (16)$$

As is seen from (16), the ratio of specific energies of tough fracture in Charpy and Mesnager specimens in this case depends on structural element r^*, mechanical characteristics $\sigma_{0.2}$ and σ_t and strain ageing n. As regards the latter, as was already noted in [2, 20], this characteristic can be determined from the following dependence with the accuracy sufficient for engineering purposes:

$$n = 0.222\,\frac{\sigma_t}{\sigma_{0.2}} - 0.182. \qquad (17)$$

It should be noted that expression (17) is empirical and is applicable at $n \geq 0.04$. This should be also taken into account in further analysis.

Thus, using equation (17) and also substituting the numerical values of elastic stress concentration in notch tips and curvature radii into expression (16), yields:

$$a_U/a_V = \left[2.683\,\frac{1+4r^*}{1+16r^*}\right]^{\frac{n}{1+n}} \times$$

$$\times \frac{2.916\left(\frac{1+4r^*}{2.1^2}\right)^{\frac{1}{1+n}} + \frac{(n+0.182)(1+n)}{0.222(1-n)}}{2.976\left(\frac{1+16r^*}{3.44^2}\right)^{\frac{1}{1+n}} + \frac{(n+0.182)(1+n)}{0.222(1-n)}}. \qquad (18)$$

Figure 5 shows the behaviour of this dependence. As is seen from Figure, in the range of possible variation of the values of strain ageing n and parameter r^*, the ratio of total specific energies of tough fracture of Mesnager and Charpy specimens varies in a rather narrow range of 1.13–1.33.

Obtained quasistatic dependence (18) is also valid for dynamic loading, proceeding from the following considerations: critical deformation corresponding to initiation of a tough crack depends weakly on loading rate; as follows from Figure 5, ratio a_U/a_V practically does not depend on values of strain ageing n.

Experimental data derived at PWI, when studying welds made with Sv-08A, Sv-08G2S, Sv-10G2 and Sv-10GSMT wires using AN-43 flux in welding 08G2SFB steel can be a rather representative example. Mechanical properties of the considered welded joints are given in the Table. Figure 6 gives the results of comparison of variation of the ratios of minimum

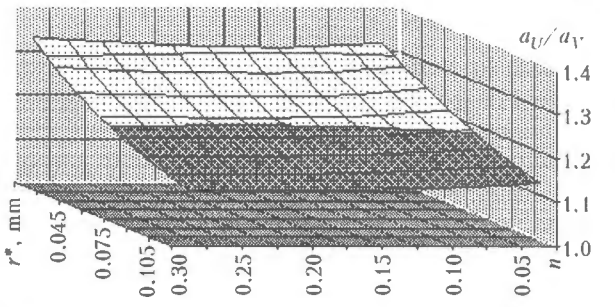

Figure 5. Variation of the ratio of impact toughness at fracture of standard Mesnager and Charpy specimens, depending on structural element r and strain ageing n

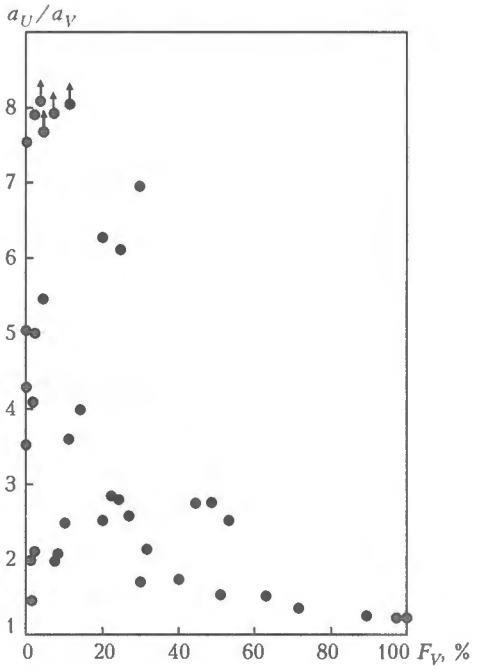

Figure 6. Variation of the ratio of impact toughness values of standard Mesnager and Charpy specimens, made of welded joints produced with different low-carbon and low-alloyed wires (Sv-08A, Sv-08G2S, Sv-10G2 and Sv-10GSMT) using AN-43 flux in welding of coiled steel 08G2SFB, depending on fibre content F_V in the fracture of Charpy specimens

and maximum values of impact toughness in Mesnager and Charpy specimens, depending on fibre content, F_V, in the fracture in Charpy specimens at the same testing temperatures.

As is seen from Figure 6, relative variation of impact toughness values a_U/a_V of the considered specimens in a region with fibre content in the fracture of a Charpy specimen of more than 60 % agrees quite well with the calculated data.

Mechanical properties of weld metal in welded joints produced in welding with AN-43 flux (T_{test} = 20 °C)

Welding consumables	σ_t, *MPa*	$\sigma_{0.2}$, *MPa*	δ, %	ψ, %
Sv-08G2S	610	487	25.3	67.9
Sv-10GSMT	574	464	26.6	72.5
Sv-10G2	482	387	28.5	70.8
Sv-08A	532	436	22.8	60.9

CONCLUSIONS

1. Obtained analytical dependencies allow analyzing variation of specific energy of tough fracture initiation and propagation in Charpy and Mesnager specimens, depending on structural element r^* and strain ageing n.

2. Existence of a link between specific energy of tough fracture in Mesnager and Charpy specimens was confirmed analytically and a simple engineering dependence was derived.

1. Girenko, V.S., Dyadin, V.P. (1985) Relationships between the impact toughness and fracture mechanics criteria δ_{1c}, K_{1c} of structural steels and their welded joints. *Avtomatich. Svarka*, **9**, 13–20.
2. Girenko, V.S., Dyadin, V.P. (1990) Correlation of characteristics of crack-resistant materials and welded joints with standard mechanical test results. *Ibid.*, **6**, 1–4.
3. Girenko, V.S., Dyadin, V.P. (1993) Relationships between the impact toughness and fracture mechanics criteria δ_{1c}, K_{1c} of structural steels and their welded joints. In: *Coll. of abstr. of ICF-8 on Fracture Mechanics: Successes and Problems*, Kiev, July 8–14, 1993. Lviv.
4. Girenko, V.S. (1995) Some approaches for evaluation of static crack resistance of metallic materials and welded joints. *Avtomatich. Svarka*, **9**, 74–77.
5. Bashmakov, V.E., Georgiev, M.N., Kolodyuk, V.P. et al. (1983) Comparison of critical brittleness temperatures determined on specimens with different stress concentrators. *Zavod. Laboratoriya*, **9**, 77–81.
6. Shishkin, V.Yu., Makurin, V.A., Efimov, P.I. (1987) On notch shape in impact specimens and impact toughness values. *Ibid.*, **3**, 71–74.
7. Basko, E.M. (1989) Influence of notch sharpness on impact toughness and critical brittleness temperatures of structural steels. *Ibid.*, **7**, 73–77.
8. Safta, V., Bernat, A., Mojsa, T. (1981) Relationship between the characteristics of dynamic fracture toughness. *Ibid.*, **7**, 72–75.
9. Drozdovsky, B.A., Fridman, Ya.B. (1960) *Influence of cracks on mechanical properties of structural steels*. Moscow: Metallurgizdat.
10. Gulyaev, A.P. (1967) Division of impact toughness into its components according to the data of testing of different notch specimens. *Zavod. Laboratoriya*, **4**, 473–475.
11. Georgiev, M.N., Popova, L.V. (1969) Comparison of methods of impact toughness division. *Ibid.*, **5**, 605–611.
12. Vladimirsky, T.A. (1969) On problem of impact toughness division into its components. *Ibid.*, **5**, 612–615.
13. Rakhmanov, A.S., Livshits, L.S. (1959) On the role of notch sharpness in impact toughness testing. *Ibid.*, **12**, 1502–1504.
14. Shermazan, I.V., Zelenova, V.D. (1969) Comparison of different methods of impact toughness division. *Ibid.*, **5**, 611–612.
15. Gulyaev, A.P. (1970) On determination of crack propagation energy. *Ibid.*, **12**, 1494–1497.
16. Panasyuk, V.V., Romaniv, O.M. (2001) Charpy and fracture toughness data: limitations and advantages in evaluation of the embrittlement of metals. In: *Proc. of ESSIS Charpy Centenary Conf.*, Poitiers, Oct. 2–5, 2001. Vol. 2. Paris.
17. Girenko, V.S. (1997) *Widening fracture mechanics applications for evaluation of crack resistance of welded structure components under static loading*. Syn. of Thesis for Dr. of Techn. Sci. Degree. Kiev: PWI.
18. Peterson, R. (1977) *Coefficients of stress concentration*. Moscow: Mir.
19. Kachanov, L.M. (1956) *Principles of plasticity theory*. Moscow: Gostekhizdat.
20. Dyadin, V.P. (1998) *Development of a method for evaluation of material and welded joint resistance to stable crack growth under static loading*. Syn. of Thesis for Cand. of Techn. Sci. Degree. Kiev: PWI.

LOCAL SURFACE HEAT TREATMENT BY A CIRCULAR-SHAPED ARC DISCHARGE

D.M. KALEKO
E.O. Paton Electric Welding Institute, NASU, Kiev, Ukraine

Design and experimental procedures were used to demonstrate the possibility of producing by a magnetically-impelled arc a heat-treated section of a circular shape with minimum distortion and higher oil absorption. Characteristics of the HAZ under a magnetically-impelled arc have been studied, and it is shown that the region of a two-times increase of hardness goes down to the depth of 1.5 mm.

Keywords: *magnetically-impelled arc, surface heat treatment, circular shape, strengthened zone, heating by a magnetically-impelled arc*

Higher requirements to performance of parts, including high wear resistance and fatigue strength at low consumption of high-quality materials, led to appearance of a large number of heat treatment processes, including surface treatment, by a highly concentrated energy source, in particular plasma and electric arc. A lot of publications are devoted to investigation of the methods of plasma and arc surface treatment. According to these publications, practically all the parts are treated by an arc, scanned by different methods (under the impact of a longitudinal magnetic field, mechanical oscillations of the welding head, etc.). In many cases, the thus produced strips overlap or border on each other, forming a continuous heat-treated surface. It is noted [1] that the best result is here achieved by surface melting of parts. However, in this case it is impossible to avoid distortions in the treated area.

The initial prerequisite for studying the local circumferential surface heat treatment was the assumption that a fast displacement of the arc will reduce thermal erosion of the surface of the treated part. In addition, a circular shape of the higher hardness section will increase the oil absorption of the heat treated friction surface, and also compressive stresses may appear on the processed surface of the part and, as a consequence, its fatigue strength may become higher [2].

Heating of the circular surface can be performed in the most effective manner by rotation of the arc in a transverse magnetic field between the auxiliary circular electrode and item. In this case, the speed of arc rotation will depend on the intensity of the magnetic field in the arcing region and arc current [3]. Heating of a semi-infinite body by a heat source, moving along a circular trajectory, can be analyzed assuming the circuit of a moving point source.

Initial equation, having the form of

$$T_A = T_0 + \int_0^t \frac{2q}{c\gamma(4\pi at)^{3/2}} \exp[\overline{R}^2/4at]\, dt, \qquad (1)$$

for a stationary point source in the posed problem is transformed into (Figure 1)

$$T_A = T_0 + \frac{2q}{c\gamma(4\pi a)^{3/2}} \times \times \int_0^t \exp\left[-\frac{2rr_A\cos(2\pi nt - \varphi_A) + (r^2 + r_A^2 + z^2)}{4at}\right] \frac{dt}{t^{3/2}}, \qquad (2)$$

where T_A and T_0 are the current and initial temperature in point A; q is the heat source power; c, a, γ are the heat capacity, thermal conductivity and density of material of the heated body; n is the number of arc rotations in seconds (arc rotation speed); t is the current time; other designations are understandable from Figure 1.

Since equation (2) is invariant relative to axis Z, asimuth φ_A of arc start can be taken to be equal to zero. Equation (2) was solved by Simpson method. Proceeding from the fact that the integrand is periodic, in order to obtain accurate values, it is necessary for the number of integration intervals to be $m >> 2\pi nt$ [4]. Assuming $n = 100$ s^{-1} and $t = 2.5$ s (maximum values at experimental observation of the process of circular heat treatment), numerical integration was performed for partition number $m = 12500$. Calculation was conducted for steel 65G with the following thermophysical characteristics: $c = 700$ J/(kg·°C), $\gamma = 7.85$ g/cm^3, $\lambda = 0.325$ W/(cm·°C), $a = \lambda/c\gamma = 0.059$ cm^2/s. Radius of circular trajectory of 2.4 kW arc (maximum one in experiments described below) was taken to be

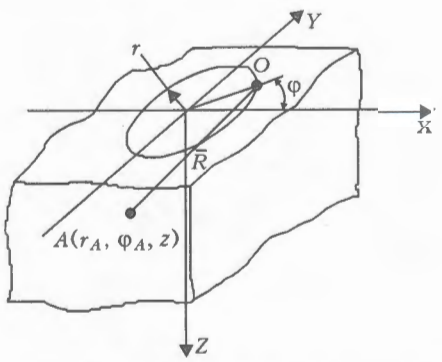

Figure 1. Circuit for calculation of heating by a rotating point heat source

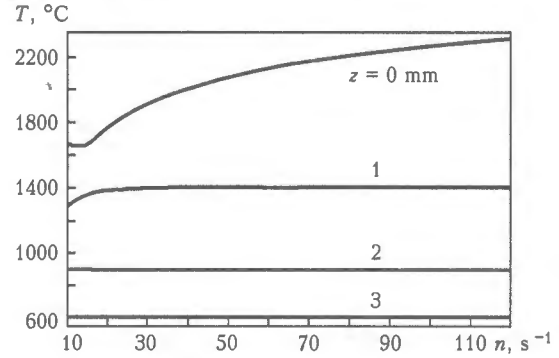

Figure 2. Dependence of temperature of a ring of 0.5 cm radius at different depth z of a semi-infinite body heated by a circular rotation of the arc at speed n for 2.5 s

0.5 cm, as a 10 mm tubular electrode with 2 mm wall thickness was used in the experiments.

Calculation by equation (2) showed a weak dependence (< 3 %) of temperature in point A (see Figure 1) on its asimuth φ_A. Therefore, further calculations were conducted at $\varphi_A = 0$. Dependence of heating under the arc on the speed of arc rotation is given in Figure 2. Strong dependence on the speed of arc rotation is observed only on the body surface and at speeds below 30 s^{-1}. At $n > 50$ s^{-1} for $z \geq 0.1$ cm the temperature in the control point drops (in the scale in Figure 2 this lowering is not noticeable). Therefore, further calculations were performed at $50 \geq n \geq 30$ s^{-1}.

The most important is temperature distribution around the diameter of the arc trajectory and through the body depth. For the above conditions this distribution is shown in Figure 3. Its shape is preserved also under other conditions of heating by a magnetically-impelled arc (Figure 4, *a*). The longer is this process, the higher the temperature in the respective points of the heated body.

Temperature equalizing is calculated by the following formula:

$$T = F(t) - F(t - t'), \qquad (3)$$

where t' is the arcing duration.

Integration of equation (3) by Simpson makes sense only under the condition that $\cos(2\pi nt) = \cos(2\pi(t - t'))$, i.e. at coincidence of the points of heat penetration and heat sink. Typical curves of temperature equalizing on the sample surface at different distance r from the circle center are shown in Figure 4, *b*. As in terms of polymorphous transformations the shape of the cooling curve is of interest only up to the point of bending of C-shaped curve of isothermal

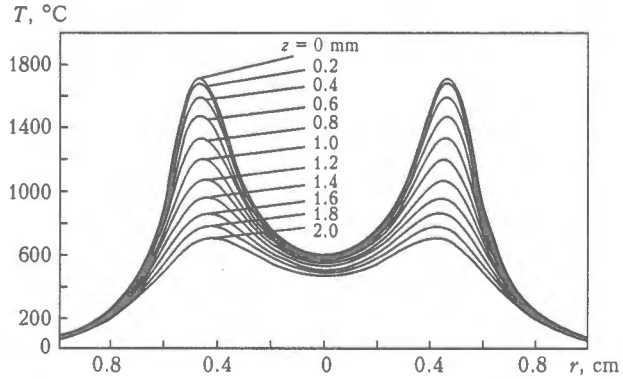

Figure 3. Temperature distribution around radius r and through depth z of a semi-infinite body at heating by an arc rotating at the speed of 30 s^{-1} for 1.4 s

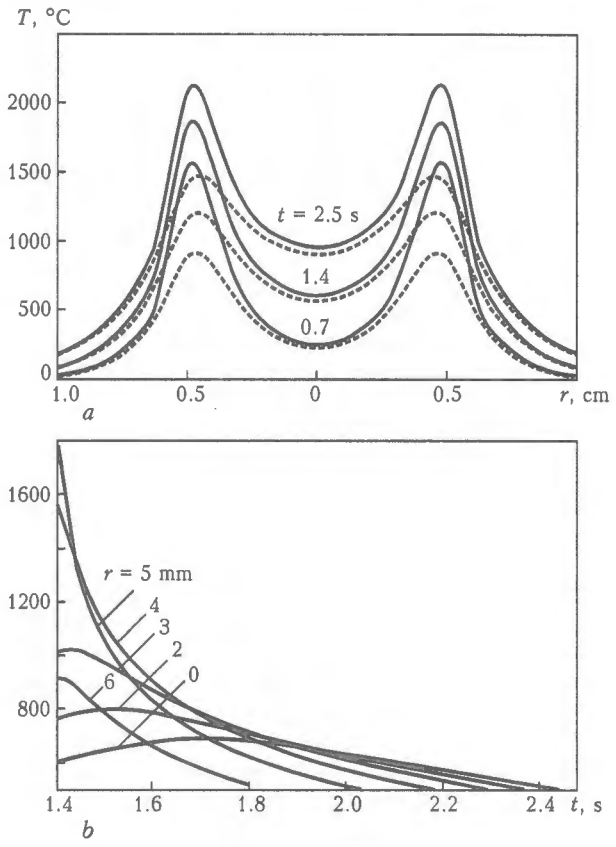

Figure 4. Temperature distribution on the surface (*solid curve*) and at 1 mm depth (*dashed*) of a semi-infinite body heated by an arc rotating at the speed of 50 s^{-1} (*a*) and temperature equalizing after arc extinguishing at $z = 0$ mm, $r = 1.4$ cm, $n = 50$ s^{-1} (*b*)

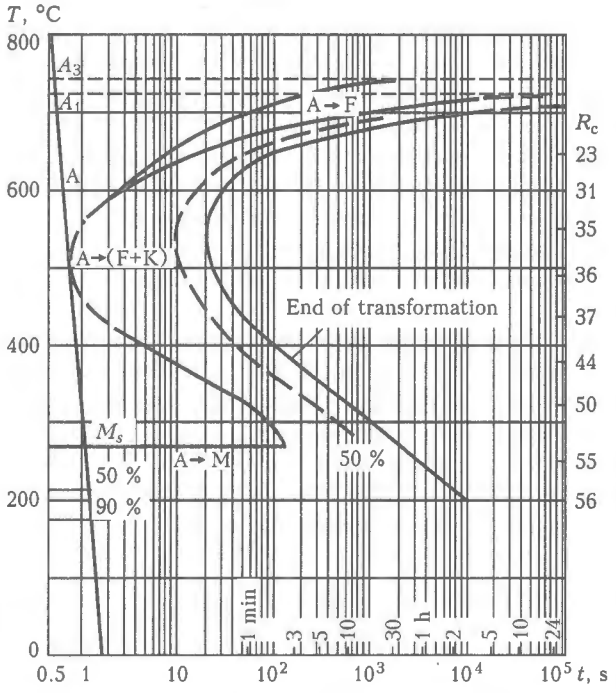

Figure 5. Isothermal diagram of decomposition of overcooled austenite in 65G steel [5]

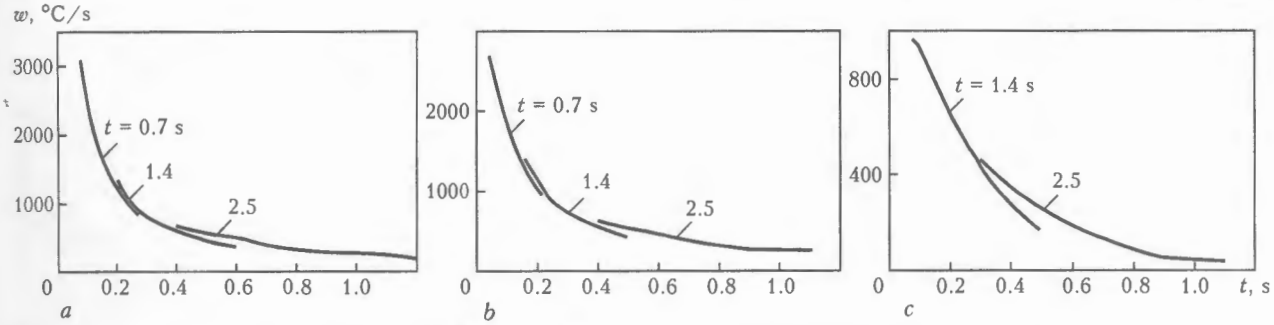

Figure 6. Rates of cooling in the range of 800–500 °C at different depth in the body after heating by an arc rotating at the speed of 50 s^{-1}: *a* — *z* = 0.5; *b* — 1.0; *c* — 1.5 mm

decomposition of austenite (for steel 65G this point is on 500 °C isotherm (Figure 5)), calculation of temperature equalizing was limited to this value. In the graph shown in Figure 5 a straight line is drawn, which determines the boundary of cooling rates, below which decomposition of primary austenite proceeds. It is seen that the limit cooling rate, which determines the martensite structure of quenched metal, is equal to 400 °C/s at the temperature of cooled region of 500 °C. Figure 6 shows the curves of cooling rates in the range of 800 to 500 °C at different depth in the body in points, located on a radius of 5 mm from the axis of arc rotation.

Thus, calculation showed the actual possibility of producing a heat-treated zone of a circular shape, using a magnetically-impelled arc; in this case, treatment depth should be sufficient for subsequent processing operations. However, calculation does not take into account the energy consumption for phase transformations and dependence of thermophysical characteristics on temperature and phase condition. Heat sink from the body surface and the influence of liquid phase spreading over the metal surface were not taken into account, either. Therefore, theoretical results were more precisely re-evaluated experimentally.

A transverse magnetic field is used most often in pipe welding, which is induced by subtractive polarity of two symmetric coils, located co-axially with the pipes being welded. At local heat treatment of the steel sheet it is impossible to generate a transverse magnetic field similar to the way it is done in pipe welding, because of a complex adjustment of the solenoid axes. Moreover, it is necessary to take into account the shielding influence of the treated item and presence of the axial component of the magnetic field in the arcing region.

We earlier [6] conducted a large scope of research to determine the possibility of producing a strong enough magnetic field, required for arc rotation around the edge of a hollow part, using just one coil, placed around the tube being welded. Results of these studies enabled development of a unit to study local surface heat treatment by a circular-shaped arc pulse discharge.

The unit, the schematic of which is shown in Figure 7, consists of a DC source AISI-2000 *1*; control unit *2*, which forms and controls the parameters of the pilot arc, switches the main arc current on and off with a preset heat treatment time; ballast rheostats *9*, regulating arc current; device for heat treatment *4* with circular electrode *8* and electromagnet of electrode displacement drive *3*, solenoid *5* with power source *6*. Heat treated sample *7* is placed into the device.

DC source AISI-2000 was developed by AISI company (Georgia) based on the statement of work, provided by PWI and is designed for arc-contact T-joint stud welding by 200–2000 A current. AISI-2000 was used for research work on surface heat treatment without any upgrading. The studied process was controlled, using the control unit for arc-contact T-joint stud welding with the necessary changes related, chiefly, to absence of the stage of stud immersion into a molten metal pool on the sheet. The arc discharge ran between a tubular electrode of 10 mm diameter with 2 mm wall thickness and plate of 65G steel. The solenoid had 1655 turns. Variable parameters of the mode were treatment time (t = 0.7–2.5 s), treating arc current (I = 100–200 A), supply current of arc rotation sole-

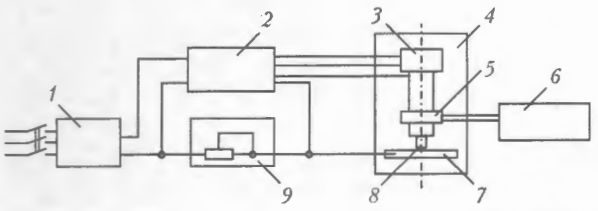

Figure 7. Diagram of a laboratory unit (for designations see the text)

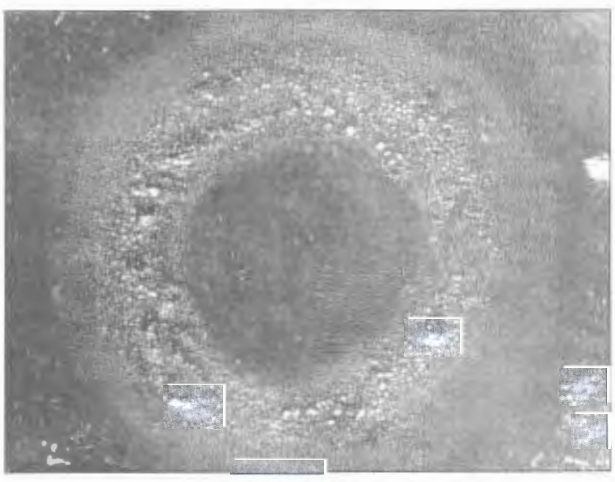

Figure 8. Shape of trace of 2.4 kW arc rotating at the speed of 30 s^{-1} for 2.5 s

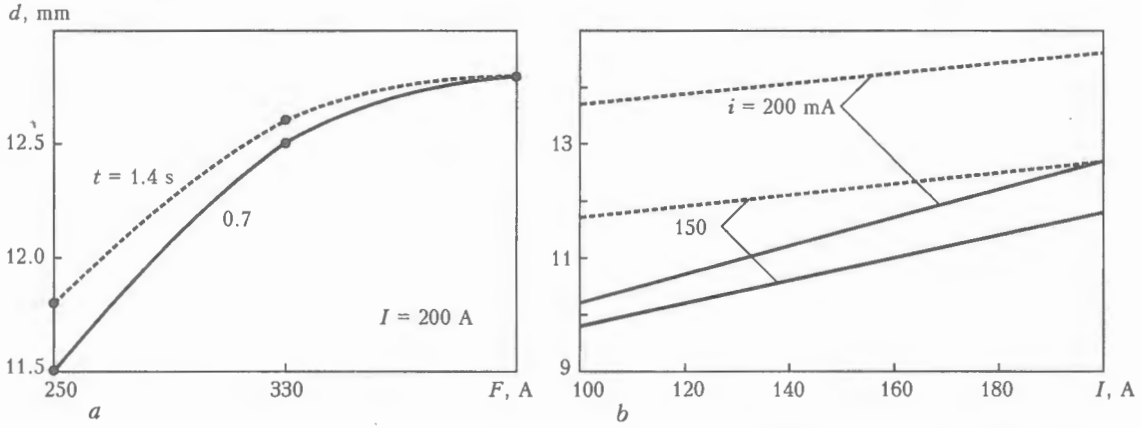

Figure 9. Dependence of outer diameter of a circular arc trace on magnetomotive force (*a*) and arc current (*b*) at different duration of arcing and supply current of arc rotation solenoid

noid (i = 150–250 mA), as well as arc gap length (2–2.5 mm). The above limits of variation of mode parameters were selected during preliminary experiments, proceeding from the necessary requirement of the arc running around the entire electrode circumference. Going beyond these limits led either to incomplete heating of the circumference under the electrode (formation of a crescents-shaped trace), or to melting of the entire surface within the ring. Appearance of the arc trace on a plate was studied at ×10 magnification in MBS-2 microscope. On metallographic sections, prepared by standard procedures, the depth and width of the treated zone was measured at ×155 and ×62 magnifications, respectively. Microhardness was determined with a LECO M400 instrument at 50 g load.

A condition to obtain an arc trace in the form of a closed ring is fulfilled not in the entire range of variation of the above arc parameters. For instance, at increase of arc current up to 200 A, circular melting was only obtained at not more than 0.7 s impact duration. At a longer arcing time the entire area of the circle was melted.

Mode adjustment allows obtaining a surface with minimum distortions (Figure 8) and high microhardness of the HAZ metal.

The arc trace diameter increases at increase of magnetomotive force (Figure 9, *a*) and arc current (Figure 9, *b*). Figure 9, *b* shows two sets, obtained at arcing duration of 2.5 s (dashed) and 1.4 s (solid curves). At the lowest arc currents and controlling magnetic field the arc rotates around the inner edge of the tubular electrode. At increase of these parameters and respective increase of the speed of arc rotation around the electrode edge, a neutral gas, entrained by the arc, is shifted to the outer edge of the tube by a centrifugal force. In this case, the arc acquires a conical shape, expanding the more at the treated sheet, the higher the interacting arc current and controlling magnetic field.

Longer arcing time also leads to increase of the outer trace diameter. This is, apparently, related not to kinematics, but to energy of the arc. The same explanation may be suggested for variation of the trace width, rising with arc current, and time of its rotation from 1.7 mm (I = 100 A, t = 0.7 s) up to complete melting up at I = 200 A and $t \geq 1.4$ s. Increase of rotation speed allows producing a circular shape of the arc trace right up to t = 2.5 s. Current increase at maximum magnetomotive force of the coil leads to narrowing of the arc trace (due to increase of inner diameter of the circle), because of a higher rotation speed. Arc elongation leads to widening of its trace.

Discrepancy between the calculated temperature in the center of the arc trace circle, which during equalizing does not exceed 1100 °C, and melting of

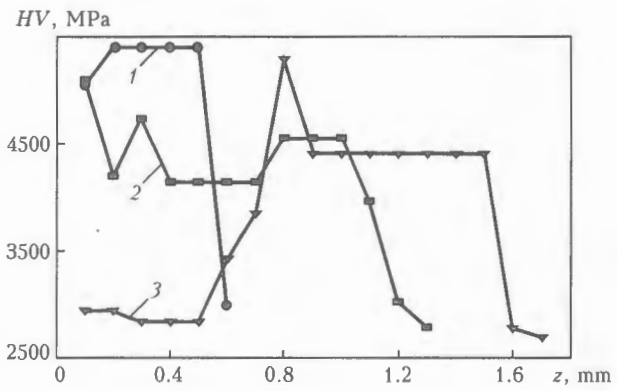

Figure 10. Distribution of HV microhardness across depth z of a sample heated at different treatment modes: *1* — t = 2.5 s, I = = 103 A, i = 150 mA; *2* — t = 2.5 s, I = 185 A, i = 150 mA; *3* — t = 2.5 s, I = 196 A, i = 200 mA

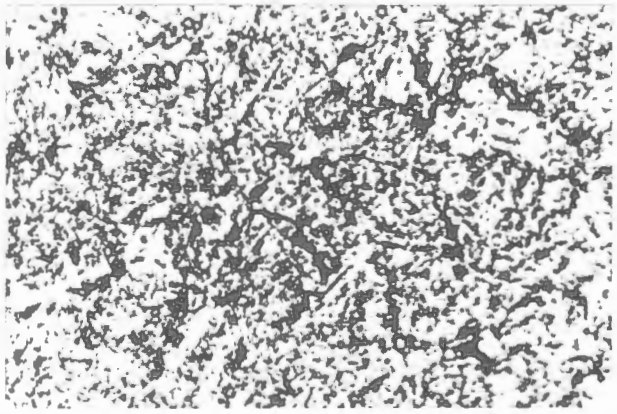

Figure 11. Microstructure of the section of HAZ metal after heat treatment to mode 1 (see Figure 10) (×800)

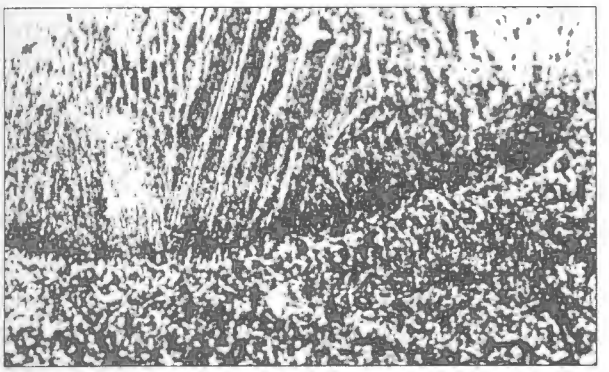

Figure 12. Microstructure of fusion zone on the surface of the sample treated to mode 3 (see Figure 10) (×400)

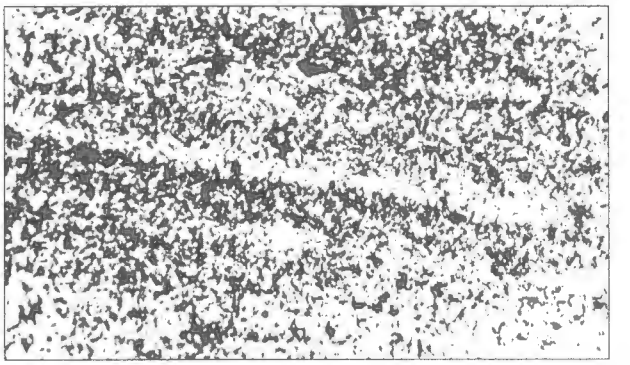

Figure 13. Microstructure of a section of HAZ metal after treatment to mode 3 (see Figure 10) (×400)

the entire area of the circle under certain conditions, is related, probably, to metal spreading from areas heated above the melting temperature (0.35 cm < $< r <$ 0.45 cm) over the hot inner region of the treated local surface.

Characteristic curves of variation of HAZ metal microhardness are shown in Figure 10.

In keeping with theoretical calculation at insufficient heating (Figure 10, curve *1*) just to the depth of 0.6 mm (see Figure 6, *a*), the cooling rate is sufficient for formation of a fine-grained martensite structure (Figure 11). Deeper down the microhardness drops to the level of ferrite-pearlite structure of the base metal. At increase of heat source power and arc rotation speed (Figure 10, curve *2*) microhardness of HAZ metal corresponds to martensite structure only near the surface. Starting from $z = 0.2$ mm the thermal impact area has the structure of upper bainite.

At intensive melting of the sample surface the solidified metal of the cast zone has a dendritic structure (Figure 12) with a relatively low microhardness (Figure 10, curve *3*). From the Figure it is seen that the high hardness is noted directly under the melting zone. Cooling proceeded so quickly here that there was not enough time for recrystallization to be over, rolling texture and fine-grained martensite were preserved as a result of quenching (Figure 13).

CONCLUSIONS

1. Local surface heat treatment by a magnetically-impelled arc allows obtaining a strengthened zone of a circular shape, having minimum distortion (convexity).

2. Depth of heat treatment zone of a higher hardness, which is 2 times higher than that of base metal, is up to 1.5 mm.

3. Presence of a central section of an unquenched (soft) metal promotes higher oil absorption of the surface and, as a result, decrease of the friction coefficient and wear of heat-treated surface can be anticipated.

1. Vajnerman, A.E., Kolganov, B.D., Popov, V.O. (1995) State-of-the-art and prospects of application of materials with special properties of surface layers. *Voprosy Materialovedeniya*, **1**, 116–125.
2. Safonov, A.N. (1996) Residual stresses in surface layers after laser treatment and their influence on service properties. *Svarochn. Proizvodstvo*, **8**, 7–11.
3. Gagen, Yu.G., Taran, V.D. (1970) *Magnetically-impelled arc welding*. Moscow: Mashinostroenie.
4. Bakhvalov, N.S. (1975) *Numerical methods*. Moscow: Nauka.
5. Popov, A.A., Popova, L.E. (1961) *Isothermal and thermokinetic diagrams of overcooled austenite decomposition*. Refer. Book of heat-treatment specialist. Moscow-Sverdlovsk: Mashgiz.
6. Lebedev, V.K., Kaleko, D.M., Bykhovets, V.N. (1999) Arc-contact T-joint welding of tubular shaped parts. *Avtomatich. Svarka*, **7**, 30–36.

NEW HEAT-RESISTANT STEELS FOR MANUFACTURE OF WELDMENTS IN HEAT POWER UNITS (REVIEW)

V.Yu. SKULSKY and **A.K. TSARYUK**
E.O. Paton Electric Welding Institute, NASU, Kiev, Ukraine

New grades of heat-resistant structural steels with an increased content of chromium (9–12 %), intended for manufacture of parts operating at supercritical (T > 560–600 °C) and ultra-supercritical (T ~ 620–630 °C) steam parameters, are considered. The effect of alloying on phase composition, corrosion resistance, ageing processes, long-time strength and weldability of steels is analysed.

Keywords: *heat-resistant steels, complex alloying, supercritical parameters, corrosion resistance, structure, ageing, dispersed phases, long-time strength, weldability*

Cr–Mo and Cr–Mo–V heat-resistant steels of the type of 12X1MF, 15X1M1F, 2.25Cr1Mo (P22) and X20CrMoV121 have been used for a long time in the world practice for manufacture of high-temperature parts of power boiler units. These steels allowed production of steam with temperature $T \leq 540$–560 °C and pressure $P \leq 25$–28 MPa. Further increase in steam parameters, in excess of the above ones (critical), is inadmissible because of an insufficient level of long-time strength of such steels. Progress in the field of development of new power units operating with steam having supercritical parameters (temperature up to 600 °C and pressure up to 31 MPa) became possible only after emergence of a new multi-component steel P91 (X10CrMoVNb 91), which was developed on a base of steel P9 (9Cr–1Mo). Steel P91 became the first material of a new generation of steels with 9–12 % Cr.

The purpose of this study is to generalise data on advanced heat-resistant steels, covering a period of the last two decades.

Chemical composition of the materials considered, including steel P91 and its prototype — steel P9, is given in the Table. Basic elements affecting the character of phase transformations in these steels are chromium, molybdenum and nickel. Steel P9 of the initial composition is quenched to form martensite, and may contain up to 2 % hypoeutectoid ferrite between the grains of primary austenite [6], which has a negative effect on performance under creep conditions. In welding, melting and solidification of this steel may result in formation of interlayers of retained δ-ferrite extending along the austenite phase [7].

Extra addition of nickel to steel P91 leads to a more complete high-temperature δ→γ transformation, on the one hand, and restriction of equilibrium decomposition of austenite, on the other hand. As a result, transformation of austenite in steel P91 ends with formation of a fully martensitic structure during cooling in tranquil air, i.e. normalising [8]. However, under conditions of slow natural cooling of massive parts, where the time during which metal dwells within a temperature range of 800–500 °C is more than 30,000–40,000 s (about 8–11 h), which corresponds to a pipe steel thickness of more than 80 mm, the probability exists of a partial equilibrium decomposition of austenite to form ferrite and carbides [8]. In such cases, precipitation of the ferrite phase can be eliminated through developing high cooling rates.

The following heat treatment conditions are recommended for steel P91: quenching (normalising) at 1040–1080 °C and tempering at 730–780 °C. These conditions guarantee the following mechanical properties (according to German standard TRD, material 1.4903, 1996 edition): σ_t = 620–850 MPa, $\sigma_{0.2} \geq$ ≥ 450 MPa, $\delta \geq 19$ % (along the rolling direction), $\delta \geq 17$ % (across the rolling direction), $KCV \geq 85$ (along the rolling direction) and ≥ 51.2 J/cm^2 (across the rolling direction). Owing to this combination of strength and ductility, the steel exhibits sufficient workability when subjected to machining, and can be treated by plastic deformation both in cold and hot (T = 750–1100 °C) state. After high-temperature pressure treatment, it is necessary to again subject the steel to normalising and tempering because of the probability of stress corrosion cracking that may develop in metal hardened by quenching, having microhardness HV 4000–4500 MPa. Strain hardening after cold deformation is eliminated by additional tempering.

In contrast to the earlier used martensitic steel X20, martenisitic transformation in steel P91 occurs at a temperature which is approximately 100 °C higher ($M_s \approx 400$ °C) [8]. In addition, steel P91 has a lower carbon content. Both factors lead to decrease in the degree of hardening of steel P91 in quenching, which provides its high resistance to cold cracking during welding. In turn, increased sensitivity of steel X20 with 12 % Cr to cold cracking leads to decrease in its weldability [8, 9].

One of the factors affecting development of damageability of boiler units (collectors, superheaters, screen pipes) and piping systems during operation is

Chemical composition of some common and new multi-component heat-resistant steels [1–5]

Steel grade	Content of elements, wt.%						
	C	*Si*	*Mn*	*S*	*P*	*Cr*	*Ni*
10CrMo910 (T22/P22)	0.05–0.15	< 0.5	0.30–0.60	< 0.025	< 0.025	1.9–2.6	–
X20CrMoV121 (X20)	0.17–0.23	< 0.5	< 0.10	< 0.03	< 0.03	10.0–12.5	–
T9/P9	< 0.15	< 0.1	0.30–0.66	< 0.03	< 0.03	8.0–10.0	–
X10CrMoVNb910 (T91/P91)	0.08–0.12	0.2–0.5	0.30–0.60	< 0.01	< 0.02	8.0–9.5	< 0.4
X11CrMoWVNb911 (E911)	0.09–0.13	0.1–0.5	0.30–0.60	< 0.01	< 0.02	8.5–9.5	0.1–0.4
X10CrWMoVNb92 (NF616, T92/P92)	0.07–0.13	< 0.5	0.30–0.60	< 0.01	< 0.02	8.5–9.5	< 0.4
HCM12	< 0.14	< 0.5	0.30–0.70	< 0.03	< 0.03	11.0–13.0	–
HCM12A (T122/P122)	0.07–0.14	< 0.5	< 0.70	< 0.01	< 0.02	10.0–12.5	< 0.5
7CrMoVTiB10-10	0.05–0.10	0.15–0.45	0.30–0.70	< 0.01	< 0.02	2.2–2.6	–
HCM2S(T23)	0.04–0.10	< 0.5	0.10–0.60	< 0.01	< 0.02	1.9–2.6	–

Cont.

Steel grade	Content of elements, wt.%					
	Mo	*V*	*Nb*	*W*	*N*	*Others*
10CrMo910 (T22/P22)	0.87–1.13	–	–	–	–	–
X20CrMoV121 (X20)	0.8–1.2	0.25–0.35	–	–	–	–
T9/P9	0.9–1.1	–	–	–	–	–
X10CrMoVNb910 (T91/P91)	0.85–1.05	0.18–0.25	0.06–0.10	–	0.03–0.07	< 0.04 Al
X11CrMoWVNb911 (E911)	0.9–1.1	0.18–0.25	0.06–0.10	0.9–1.1	0.05–0.09	–
X10CrWMoVNb92 (NF616, T92/P92)	0.3–0.6	0.15–0.25	0.04–0.09	1.5–2.0	0.03–0.07	< 0.04 Al 0.001–0.006 B
HCM12	0.8–1.2	0.2–0.3	< 0.2	0.8–1.2	–	–
HCM12A (T122/P122)	0.25–0.60	0.15–0.30	0.04–0.10	1.5–2.5	0.09–0.10	< 0.04 Al < 0.005 B 0.3–1.7 Cu
7CrMoVTiB10-10	0.9–1.1	0.2–0.3	–	–	< 0.012	0.05–0.10 Ti 0.0015–0.0070 B
HCM2S(T23)	0.05–0.30	0.2–0.3	0.02–0.08	1.45–1.75	< 0.03	< 0.04 Al 0.0005–0.0060 B

corrosion wear of their internal surfaces under the effect of steam and water [10–12]. The process of corrosion of metal (with no allowance for peculiarities of the effect of deposits of salts from water and various complex compounds, as well as changes in the character of water boiling [12]) comprises several stages, i.e. formation of oxide layer (scale consisting of several layers), fracture of scale, its separation and subsequent corrosion of an exposed metal surface [11]. Hard particles of scale and deposits present in a circulating water, involved in the vapour phase, cause erosion wear of piping systems and working surfaces of turbines [10, 11, 13]. Additionally, roughness of the surface of metal in heavy-loaded parts acts as a stress raiser and leads to decrease in the fatigue limit [14] (in this case it is thermal fatigue under thermal cycling conditions) and a special type of fatigue (corrosion-fatigue [12]) damage. In turn, strength of the oxidised surface layer, influencing service life of equipment, depends upon alloying of steel and, first of all, upon the concentration of chromium and alloying elements in it [10, 11]. Study [11] gives comparative evaluation of corrosion resistance of steels of the P91, P91 + W, X20 and P22 types.

As seen from the results shown in Figure 1, increase in the test time leads in all the cases to decrease in the intensity of corrosion wear, which is most likely associated with decrease in the rate of mass transfer of an oxidising component to the metal surface through an oxidised layer barrier. Under the conditions considered, corrosion resistance of steel with 12 % Cr is a bit higher than that of steel with 9 % Cr.

It can be seen that the corrosion layer near the metal surface consists of iron-chromium oxides, whereas the external layer consists of iron oxide and magnetite (Fe_3O_4). Metal near the interface with scale is depleted in chromium, and corrosion affects the Cr-depleted regions. The corrosion process develops uniformly in steel P91, and the metal–scale interface remains relatively smooth. The depth of corrosion

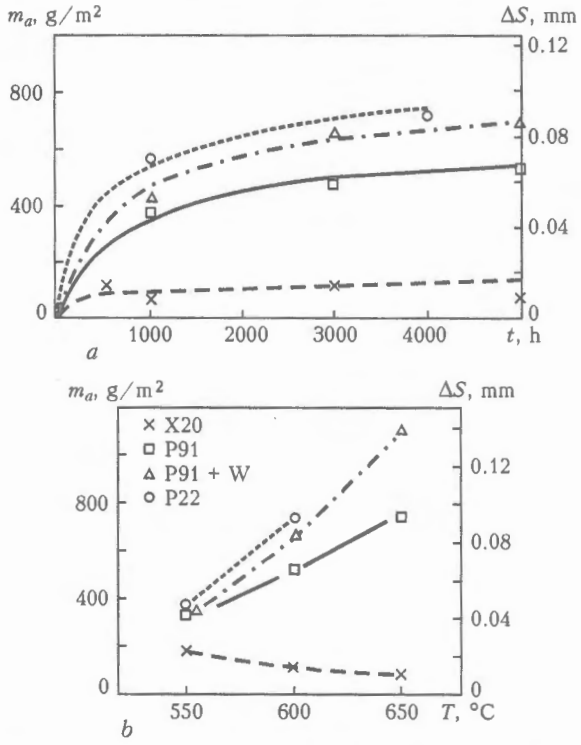

Figure 1. Effect of test time t for heat-resistant steels in steam-gas environment on the character of changes in mass losses m_a and metal thickness decrease ΔS at a temperature of 600 °C [11] (*a*), and effect of temperature T on changes in the same corrosion characteristics per test cycle at t = 4000 h (*b*) [11]

damage of metal increases with increase in temperature. In steel X20 the corrosion process results in local recesses formed on the surface, and size of these recesses increases with growth of temperature. This increased roughness, extending the contact area, leads to increase in adhesion between the metal and scale. Besides, the oxidised layer in steel X20 contains more chromium and has higher strength, and transfer of chromium to this layer grows with increase in temperature. This attributes to decrease in mass losses in steel X20 with increase in temperature, as well as increase in these losses in steel of the P91 type (Figure 1, *b*).

Despite the above differences, the rates of corrosion of steels with 12 and 9 wt.% Cr are considered to be close and acceptable for their service conditions. For steels of the type of P91 and P91 + W, the decrease in metal thickness during 10^5 h at 600 °C caused only by corrosion, as calculated by the extrapolation method, is 0.2–0.3 mm, which should be taken into account in design of boiler equipment [11].

Resistance of modified steels with 9 % Cr of the P91 type against development of high-temperature creep is provided by alloying them with chromium and molybdenum, strengthening of solid solution with dispersed phases and ensuring of high dislocation density as a result of martensitic transformation [8, 15, 16]. In this case, strengthening with microdispersed phases and by complex microalloying is achieved due to formation of microdispersed nitrides and precipitation of coarse carbides $M_{23}C_6$ along the grain boundaries and between martensite laths in tempering, as well as intra-lath (in locations with an increased physical defect content) fine carbonitrides V/Nb of the MX type. Here the decisive factor causing increase in long-time strength of steel with a basic composition of 9Cr–1Mo is microdispersed strengthening (formation of fine particles of the MX type and stabilisation of the grain boundaries with carbides $M_{23}C_6$) [8].

Main phases that influence the creep process under ageing conditions during long-time service are precipitates of nitrides VN and Laves phases [16]. Fine nitride particles provide efficient strengthening of metal and are characterised by low susceptibility to coagulation. The Laves phases have a double effect. Their formation at an early stage of operation leads to strengthening of solid solution. At the same time, at a longer cycle of ageing the Laves phases weaken the crystalline lattice by combining alloying elements (molybdenum, tungsten), and, additionally, they are susceptible to rapid coagulation. Therefore, the positive effect of the Laves phases shows up only if the operating periods are sufficiently short. This character of changes of the dispersed precipitates in steel of the P91 type during long-time ageing served as the ground to revise and decrease the preliminarily predicted level of its long-time strength at 600 °C for 10^5 h from 100 to 90 MPa [8].

Tungsten was additionally introduced into the composition of a new generation of high-chromium steels to further increase their long-time strength [1, 3, 4, 16–18]. The positive role of tungsten (like molybdenum) is related to strengthening of the crystalline lattice, increase in recrystallisation temperature and restriction of the diffusion processes, which, in turn, provides improvement of stability of solid solution at increased temperatures [1, 19]. As noted in study [3], tungsten also promotes lowering of the rate of coagulation of carbides $M_{23}C_6$. The normal tungsten content is 0.8–2.6 wt.% [1].

Among the new W-containing materials given in the Table, steel E911 developed in Europe under the European Program COST 501 [3, 4] is closest in alloying to steel P91. At present, some European companies, such as Mannesmann (Germany), Valloures (France) and Dalmline (Italy), manufacture pipes of this steel from ingots supplied by United Engineering Steel (Great Britain) [1, 4, 18]. Like steel P91, steel E911 belongs to materials of the martensitic class, has similar characteristics of thermokinetic transformation of austenite and contains identical precipitates of strengthening phases formed in tempering, i.e. intergranular carbides $M_{23}C_6$, intragranular (formed mostly at dislocations inside the subgrains) fine carbides and nitrides of vanadium and niobium of the MX type [3, 18]. The application field of this steel includes manufacture of welded piping systems for supercritical steam, fittings and collectors [4].

The metallurgical industry of Japan has mastered production of steels NF616 (P92), HCM12 and NCM12A (T122/P122) [1, 2, 4, 16, 17, 20]. Steel

NF616 is produced by Nippon Steel, and steels HCM12 and HCM12A — by Sumitomo Metal Industries, Ltd. and Mitsubishi Heavy Industries [1, 17, 20].

In structure characteristics, steel NF616 (P92) belongs to a group of martensitic materials with 9 % Cr and differs from steel E911 in a lower average molybdenum content (NF616 ~ 0.7 wt.%, E911 ~ 1 wt.%) and higher tungsten content (NF616 ~ 1.7 wt.%, E911 ~ 1 wt.%), as well as in extra microalloying with boron. Like steel P91, steel NF616 is quenched to form martensite within a wide range of cooling rates. The martensitic transformation point of this steel is M_s = 410 °C [17].

Steel HCM12A is a modification of steel HCM12. Owing to a higher chromium content (up to 11–12 wt.%), these steels have a two-phase structure consisting of martensite and retained δ-ferrite [1, 20]. According to the data of study [1], steel HCM12 with a nominal composition of 0.1C–12Cr–1Mo–1W–VNb may contain up to 30 vol.% δ-ferrite. In turn, up to 5 vol.% δ-ferrite is formed in steel HCM12A with a somewhat modified proportion of ferrite- and austenite-forming agents (0.1C–11Cr–2W–0.4Mo–1Cu–NiVNb) [1, 5]. Due to an improved alloying, steel HCM12A has a higher level of long-time strength than steel HCM12. According to the ASME standard, the level of permissible stresses for steel HCM12A at 550, 600 and 650 °C is higher by 11, 20 and 23 %, respectively, compared with steel HCM12 [1]. Transformation of austenite in steel HCM12A occurs without formation of equilibrium structures. Temperatures of the martensitic transformation range are as follows: beginning of the transformation — M_s = 350 °C, and end of the transformation M_e = 170 °C [1].

High-chromium heat-resistant steels alloyed with tungsten are characterised by the decisive effect of the Laves phases $(Fe, Cr)_2(Mo, W)$ on the extent of decrease in their long-time strength during ageing [4, 16, 18]. In this case tungsten promotes a more rapid precipitation of these phases and some additional microdispersed strengthening, on the one hand, and their more rapid coagulation, on the other hand, compared with steel of the P91 type. With this character of ageing, rapid short-time strengthening is followed by rapid decrease in long-time strength [16]. It is shown (Figure 2) by an example of steel NF616 that precipitation of the Laves phases at a temperature of 600 °C occurs after 500 h, and at 650 °C — after 200 h [4]. During a cycle of 10^5 h at 600 °C tungsten in an amount of approximately 70 % transfers from solid solution to the Laves phases. In long-time ageing, precipitation of the Laves phases leads to embrittlement. Therefore, the tungsten content of steel E911 is limited to 1 wt.%, whereas the Japanese steels contain up to 2 wt.% W [3].

While investigating precipitates formed during the process of creep tests of steel G-X12, similar to E911, the Austrian researchers showed that a new modified Z-phase, in addition to the Laves phases, might be

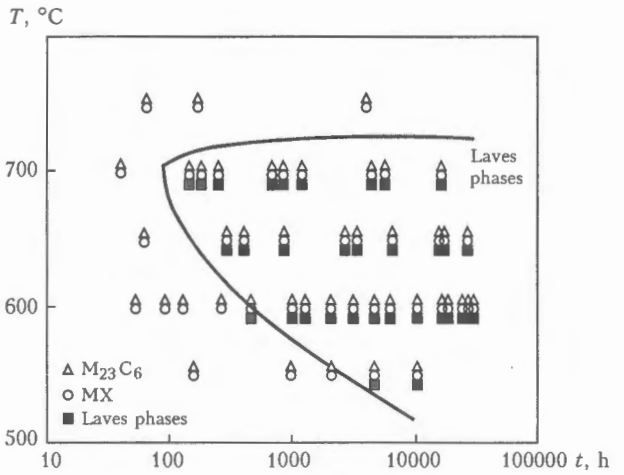

Figure 2. Effect of ageing conditions on types of precipitating phases in steel NF616 (reported in [14] by Mimura H., Ohgami M., Naoi H. and Fujita T. Conf. «Materials for Advanced Power Engineering 1994», 3–6 Oct., 1994 / D. Coutsouradis et al. (Eds). Pt 1. Dordrecht: Kluwer Acad. Publ., 1994. P. 361–372)

formed in such materials after 12,000 h of ageing at temperatures of 600–650 °C [21]. This new phase is characterised by a high content of chromium, vanadium and nitrogen. Its precipitation is accompanied by decrease in the amount of carbides. At a longer test cycle, coarsening of the Laves phases and Z-phase occurred, no coarsening of chromium and vanadium carbides of the $M_{23}C_6$ and MX types taking place in this case. The data obtained suggest that decrease in long-time strength of steels alloyed with tungsten during ageing for more than 10^4 h is associated with formation of both Laves phases and Z-phase.

Allowing for the above peculiarities of long-time ageing of new heat-resistant steels and selection of the Larson–Miller criterion values on the basis of evaluation of fracture stress during 3000 h, long-time strength for a cycle of 10^5 h at 600 °C can be preliminarily estimated as follows: steel E911 — 118, NF616 — 119, HCM12A — 109 MPa [4]. It is reported that the Japanese researchers obtained for the same conditions the higher values of long-time strength for steels of the Japanese production (NF616 — 132, HCM12A — 127 MPa) [4, 16]. This overestimation of possible actual values is related to the insufficiently correct estimate of the Larson–Miller criterion and fracture characteristics for a short test cycle (e.g. less than 100 h at 700–750 °C), during which the strength properties of specimens are hardly affected by changes in structure and alloying of solid solution caused by formation of the Laves phases [4].

New W-containing steels E911, NF616 and HCM12A have a higher level of long-time strength than steel P91. Their application makes it possible to raise the steam operating temperature to 620–630 °C and build new power boiler units with ultra-supercritical parameters (USC parameters) of steam [4, 5].

The most vulnerable (critical) locations of modern boiler equipment are thick-walled components of the main steam piping (pipes, fittings, collectors), steam superheaters and gas-tight panels [4, 5]. One of the problems addressed by the COST 501 Program was

selection of materials for manufacture of the above units, allowing for their specific service conditions. So, steels E911 and NF616 were selected as the basic materials for the manufacture of piping for steam with the USC parameters and their elements [4, 5]. Steam superheaters, the temperature of metal of which is higher than the temperature of the main steam pipes approximately by 30 °C, are made from austenitic Cr–Ni–Mo materials of the type of X3CrNiMoN17-13 [4, 5] and steel HCM12A [1].

It was a special challenge to develop material for the manufacture of gas-tight panels for a new generation of boiler units [3, 4]. These panels operate at a lower temperature than the main steam pipes. Therefore, the material for them can have lower strength characteristics. However, to provide the possibility of increasing the working parameters of the steam, the temperature and pressure of the steam-water mixture in membrane pipes should be increased accordingly. Material for such conditions should have a somewhat higher long-time strength, compared with steels used before, such as bainitic steel 10CrMo910 [3]. It is intended that in new boiler units the level of working temperatures in the membrane sections will be 500–550 °C [3, 4].

The key problem in manufacture of gas-tight panels is the absence of the possibility to conduct postweld heat treatment (tempering) of pipe-membrane welded joints [3, 4]. To ensure satisfactory toughness and avoid stress corrosion cracking, material for the gas-tight panels should have moderate sensitivity to quenching and formation of martensite during welding. Microhardness of the HAZ metal in the as-welded condition equal to HV ~ 3500 MPa can be considered acceptable [3]. Microhardness of the HAZ metal of purely martensitic materials with 9–12 % Cr is HV 4500–6500 MPa, depending upon the carbon content, which made it impossible to use them under the above conditions.

The Mannesmann Company developed a new steel 7CrMoVTiB10-10 on the base of bainitic steel 10CrMo910 (P22) with 2.25 % Cr. This new steel differs from the initial one in a decreased content of carbon to reduce the extent of hardening during welding, and in the presence of alloying microadditions to ensure the required level of long-time strength [3, 4].

Similar steel HCM2S additionally alloyed with tungsten was developed in Japan. These materials take an intermediate position between steels X20 and P91 in the long-time strength level. For example, long-time strength of these steels for 10^5 h at 600 °C is 64 MPa for 7CrMoVTiB10-10 and 84 MPa for HCM2S [4]. Judging from the character of thermokinetic transformation of austenite in steel 7CrMoVTiB10-10, structure of the HAZ metal will consist of bainite with a differing amount of martensite (~ 70–40 %), depending upon the thermal welding conditions and thickness of the steel welded, which corresponds to a change in microhardness equal to HV 3500–3200 MPa. Rapid cooling of thin metal may result in formation of a purely martensitic structure, also having a low microhardness approximately equal to HV 3600 MPa. This reaction to the thermal welding cycle proves the possibility of performing welding of the developed microalloyed steels with 2.25 % Cr without postweld tempering.

As follows from the data presented, all new multicomponent high-chromium steels are characterised by a high stability of austenite and high quenching ability with formation of martensite, which makes them sensitive to cold cracking. The factor that promotes improvement of weldability is the carbon content limitation. Compensation for the loss in strength is achieved by adding an extra amount of alloying elements and heat treatment. At the same time, increase in the degree of alloying also leads to increase in sensitivity to cracking. It is reported that steels with 12 % Cr of the type of X20CrMoV121 have a somewhat lower weldability than steels with 9 % Cr [8, 21]. In practice this shows up in the fact that, in contrast to steel X20, welding of steels with 9 % Cr can be performed with long intervals, by stopping concurrent heating, and after welding, prior to tempering, they can be cooled to room temperature. In turn, a limited tungsten content of steel E911 makes it advantageous in weldability over steel NF616, which has a higher tungsten content [3]. Steels P91 and E911 are identical in weldability, which is indirectly confirmed by the character of changes in microhardness of welded joints (Figure 3) [21].

Special processes for manual covered-electrode arc, mechanised submerged-arc and gas-shielded tungsten-electrode welding have been developed for manufacture of commercial equipment from the new high-chromium heat-resistant steels [8, 15, 21, 22–24]. Welding of similar joints is performed using consumables which provide an identical alloying system and close chemical composition of weld metal and steel [5, 8]. To avoid cold cracking, lower the level of internal stresses and impart welded joints the required structure and toughness, welding of the new heat-resistant steels with 9 % Cr is carried out with a mandatory preliminary and concurrent heating within a temperature range of 200–300 °C and with

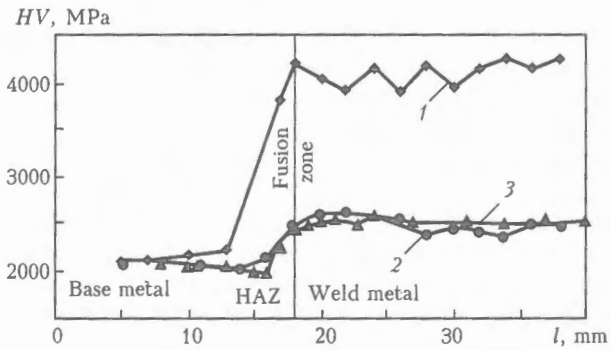

Figure 3. Distribution of values of microhardness HV in cross section of welded joints in steel P91 and E911 [21]: *1* — P91, as-welded condition; *2* — same, after tempering (750 °C, 2 h); *3* — E911, after tempering (760 °C, 2 h)

postweld high tempering at 730–780 °C [3, 10, 25, 26].

It should be noted in conclusion that the application of the new heat-resistant steels make it possible to raise the heat power generating equipment and technologies for generation of the electric power to a new quality level. At the same time, the research and development activities aimed at further increase in the efficiency of thermodynamic processes and upgrading of equipment of power units at thermoelectric and steam power plants, based on the application of new structural materials, continue in Europe, USA and Japan. The TERMI Program implemented by the EU countries provides for building of a power unit with the following parameters of steam: T = = 700–750 °C, P = 37.5 MPa and design efficiency of 52–55 %.

1. Zeman, M., Brozda, J., Pasternak, J. (1999) Ocena spawalnosci stali HCM12A przeznaczenej na elementy kotlow energetycznych pracujace przy parametrach nadkrytychnych. *Przeglad Spawalnictwa*, **6**, 1–7.
2. Haarmann, K. (1995) New material grades for tubing and piping as replacement of T22 and P22. In: *Proc. of Conf. Power-Gen'95 – Asia: Mannesmann Workshop*, Singapore, Sept. 29, 1995.
3. Bendick, W., Haarmann, K., Rigg, M. et al. (1996) Current state of development of advanced pipe and tube materials in Germany and Europe for power plant components. In: *Proc. of VGB Conf.*, Cottbus, Oct. 8–9, 1996.
4. Bendick, W., Haarmann, K., Rigg, M. et al. (1996) Assessment of creep rupture strength of new steels for advanced power plant piping and tubing. In: *Proc. of Int. Symp. on Creep Resistant Metallic Materials*, Hradec and Moravici, Czech Rep., Sept. 23–26, 1996.
5. Hoizer, G. (1997) Filler materials for welding in power engineering. *Avtomatich. Svarka*, **9**, 40–44, 47.
6. Choudhary, B.K., Bhanu Sankara Rao, K., Mannan, S.L. et al. (1999) Serrated yielding in 9Cr–1Mo ferritic steel. *Mat. Sci. and Tech.*, 15(**7**), 791–797.
7. Laha, K., Latha, S., Bhanu, K. et al. (2001) Comparison of creep behaviour of 2.25Cr–1Mo/9Cr–1Mo dissimilar weld joint with its base and weld metals. *Ibid.*, 17(**10**), 1265–1272.
8. Zschau, M., Niederhoff, K. (1994) Construction of piping systems in the new steel P91 including hot induction bends. *VGB Kraftwerkstechnik*, 74(**2**), 142–149.
9. Schubert, J., Ulrichs, K., Scholler, H. (1997) Weldability of heterogeneous joints between the cast steel GX12CrMoWVNb10-11 and low alloyed steels. *Schweissen und Schneiden*, **9**, 688–690.
10. Irving, B. (1991) A promising chrome-moly steel returns to American shores. *Welding J.*, 70(**12**), 35–40.
11. Haarmann, K., Schwenk, W., Venkateswarlu, J. et al. (1993) Hochtemperaturkorrosionsbestaendigkeit des warmfesten Stahls X10CrMoVNb91 (P91/T91) im Vergleich zu hoeher- und niedriglegierten warmfesten ferriti-schen Chromstaehlen in Wasserdampt. *VGB Kraftwerkstechnik*, 73(**9**), 837–840.
12. Vajnman, A.B., Melekhov, R.K., Smiyan, O.D. (1990) *Hydrogen-induced embrittlement of high-pressure boiler components*. Kiev: Naukova Dumka.
13. Keiji, S., Ichiro, K., Muneharu, S. et al. (1988) Erosion of stainless steel and Cr–Mo steel in moving liquid medium. *J. Iron and Steel Inst. Jap.*, 84(**12**), 881–887.
14. Nuriakhmetov, V.D. (2000) Influence of fatigue on service reliability of tubes. Abstr. of pap. by Niinomi, M. *Bulletin of Iron and Steel Inst. Jap.*, 5(**20**), 16–22.
15. *The success of new material*. Reprint from «Report». Issue S28/29. Mannesmann Rohr.
16. Koukal, J., Schwarz, D. (1998) Welding of steels for power engineering. *Zvaranie*, **6**, 2–5.
17. Ohgami, M., Mimura, H., Naoi, N. et al. (1997) Development of 9CrW tube, pipe and forging for ultra supercritical power plant boilers. *Nippon Steel Tech. Rep.*, 72(Jan.), 59–64.
18. Vladimirov, V.B. (2001) Properties and structure of modified 9 % Cr steel. *Abstr. of pap. by Gianferncesco, A. et al. La Rev. de Met.*, **1**, 117–123.
19. Lanskaya, K.A. (1976) *High-chromium high-temperature steels*. Moscow: Metallurgiya.
20. *TWI information site*: power@twi.co.uk.
21. Cerjak, G., Letofsky, E. (2000) Structure and properties of E991 steel welded joints. *The Paton Welding J.*, **9/10**, 112–116.
22. Rosenbrock, L.A. (2001) Critical overview of the welding of P91 material. *Austral. Welding J.*, 46(**2nd Qw.**), 5–8.
23. Zemzin, V.N. (1966) *Dissimilar steel welded joints*. Moscow: Mashinostroenie.
24. Gotalsky, Yu.N. (1981) *Welding of dissimilar steels*. Kiev: Tekhnika.
25. Adam, W., Mischok, W., Wellnitz, G. et al. (1994) Welding on new types of steel for power plant construction. In: *Proc. of Conf. on Welding and Cutting*, Bremen, 28–30 Sept., 1994.
26. Bergquist, E.-L. (1999) Consumables and welding modified 9Cr–1Mo steel. *Svetsaren*, 54(**1/2**), 22–25.

ELECTRON BEAM WELDING OF TURBINE BLADE PACKS OF 08Kh16N13M2B AND 18Kh11MNFBSh STEELS

M.L. ZHADKEVICH[1], A.A. BONDAREV[1], O.N. KORSUN[1], S.V. NAZARENKO[1], M.A. POLISHCHUK[1], A.F. MINETS[2], V.I. NOVIKOV[2], S.I. DIDENKO[2], V.A. OLEKSEENKO[2] and M.V. BESKORSKY[2]

[1]E.O. Paton Electric Welding Institute, NASU, Kiev, Ukraine

[2]OJSC «Poltava Turbomechanical Plant», Poltava, Ukraine

Data is given on weldability in electron beam welding of high-chromium and austenitic steels applied in manufacture of turbine blades. Technology and technique of welding turbine blade packs are described. Modes of blade heat treatment after welding and joint properties are given.

Keywords: *high-chromium steels, electron beam welding, turbine blades, heat treatment, joint properties*

It was earlier established [1] that a feature of EBW of packs of turbine blades of high-chromium steels is their delayed cracking susceptibility. The same authors found that in order to prevent this phenomenon it is necessary to perform welding in the range of speeds of 1.7 mm/s $\leq v_w \geq$ 2.8 mm/s. This condition is applicable in the case, when steels are welded in a heat-hardened state. Therefore, weldability of high-chromium steels is mainly due to the kinetics of austenite transformation, which is exactly what determines the type of structure of weld metal and HAZ. The causes for formation of cracks found in the joints at EBW are both structural changes and the developing stresses induced by the thermal cycle, and the quality of base metal, containing dissolved hydrogen, oxygen and impurity elements, influencing the segregation processes. The same factors stipulate development of other kinds of defects in the zone of blade pack joints.

In order to prevent formation of such defects and ensure a high quality of the joints, packs were welded of blades made of electroslag remelted steels, the composition of which is given in Table 1.

To avoid a lot of difficulties, caused by the reaction of these steels to the thermal cycle of welding, heat treatment of the already welded blade packs was performed after their welding. Table 2 gives the heat treatment modes of each of the steel grades.

After machining and before welding the blades into packs, the blades were thoroughly degreased by organic solvents. Packs were assembled, using run-on and run-off tabs, which were fastened by tack welds performed by argon-arc welding.

Run-on and run-off tabs were made of the same steel grade as the blade packs. Tab width was somewhat greater than that of the HAZ, established during optimization of welding parameters. Size of the tabs along the butt joints (Figure 1) was selected from the condition of being large enough for reaching the welding mode and subsequent lowering of beam power to zero at the end of welding.

Parameters of the process of blade welding both from the side of the shroud and the root part are given in Table 3.

According to earlier given recommendations and to provide a higher efficiency in implementation of the batch process, the welding speed was higher than 3 mm/s in all the cases. Considering a limited volume of the vacuum chamber 6 to 8 blade packs were welded in one run (in a fixture). Welding was performed in U-212 unit with power supply from U-250A power source. In view of the small weight of assembled packs, as well as considering performance of their heat treatment after welding, no preheating before welding was used. Figure 2 shows weld formation from the shroud side, and Figure 3 is a transverse macrosection of welds made from the blade root side. The Figure shows guaranteed overlapping of the penetration zone at deposition of a two-sided weld.

One of the most critical sections at incomplete penetration of the butt joint in the root part of blade packs was the zone of taking the electron beam to full power, starting from the moment of switching on

Table 1. Composition of high-alloyed chromium steels, %

Steel grade	*C*	*Si*	*Mn*	*Cr*	*Ni*	*Mo*	*Nb*	*V*
18Kh11MNFBSh	0.23	0.45	0.75	11.3	0.93	0.95	0.354	0.38
08Kh16N13M2B	0.08	0.40	0.58	16.5	13.7	2.50	0.980	–

Figure 1. Model of a pack of two blades (run-on and run-off tabs are located at butt joints)

Table 2. Modes of heat treatment of turbine blade packs

No.	*Operation*	*Temperature, °C*	*Soaking time, h*
	08Kh16N13M2B steel		
1	Stepwise heating	Up to 200	2
2	Temperature rise	Up to 350	1.5
3	Annealing	720	3
4	Cooling in air	From 200	
	18Kh11MNFBSh steel		
1	Stepwise heating	Up to 200	2
2	Temperature rise	Up to 400	2
3	Temperature rise	Up to 600	3
4	Tempering	720	3
5	Cooling in air	From 200	

Table 3. Modes of welding packs of blades of high-alloyed chromium steels

Steel grade	*Edge thickness, mm*	*Mode parameters*				
		U_{acc}, *kV*	I_b, *mA*	I_f, *mA*	v_w, *m/h*	f_{sc}, *Hz**
18Kh11MNFBSh	13	30	115–120	58.0	20	125
	60	30	360–370	56.5	10	100
08Kh16N13M2B	13	30	120–125	57.5	20	125
	60	30	370–380	57.0	10	100

*Discrete scanning was performed by a circular trajectory with 1.2 mm amplitude.

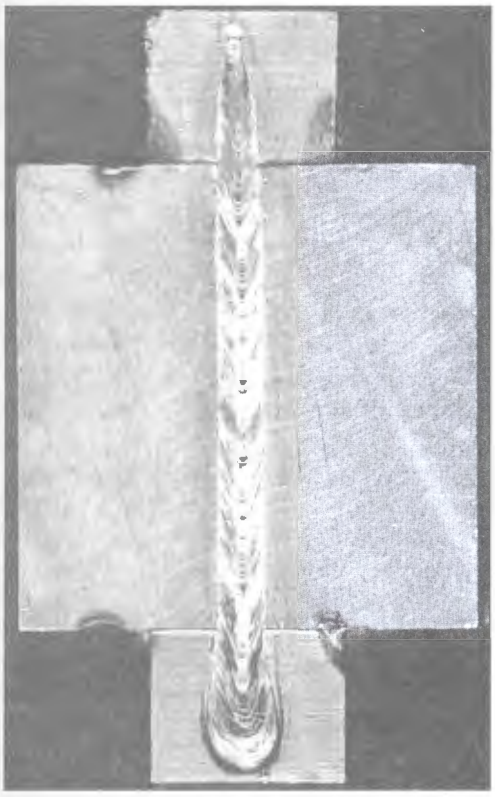

Figure 2. Appearance of a butt joint from the shroud side

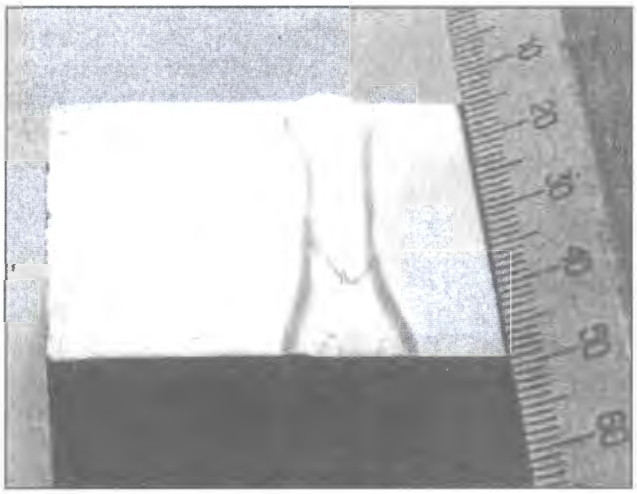

Figure 3. Macrosection of a two-sided weld in welding a pack of two blades from their root side

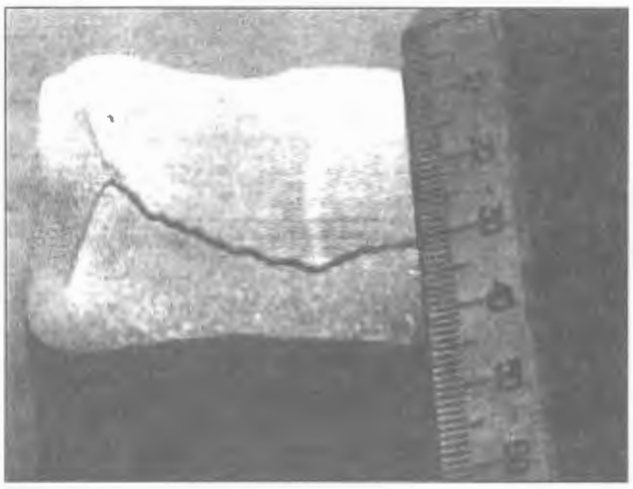

Figure 4. Macrosection of a two-sided weld (the cut is made along its axis)

the welding manipulator displacement and reaching the specified speed.

To prevent formation of root defects, welding was performed by a discretely-scanning beam with programming of power density in the heated spot [2]. Amplitude of circular scanning at the frequency of 100–125 Hz was 1.2 mm. The macrosection in Figure 4 reveals a smooth increase of penetration depth in each weld at complete absence of root defects. The most characteristic feature of prevention of root defects development is formation of weld root in the partially melted zone with not more than 1 mm rounding-off radius (see Figure 3).

When hardness distribution was studied (Figure 5) in the joints on transverse macrosections after welding, the HAZ showed short sections of partial hardening.

Subsequent heat treatment (see Table 2) leads to a practically complete equalizing of hardness both of weld metal and the HAZ to that of base metal. No

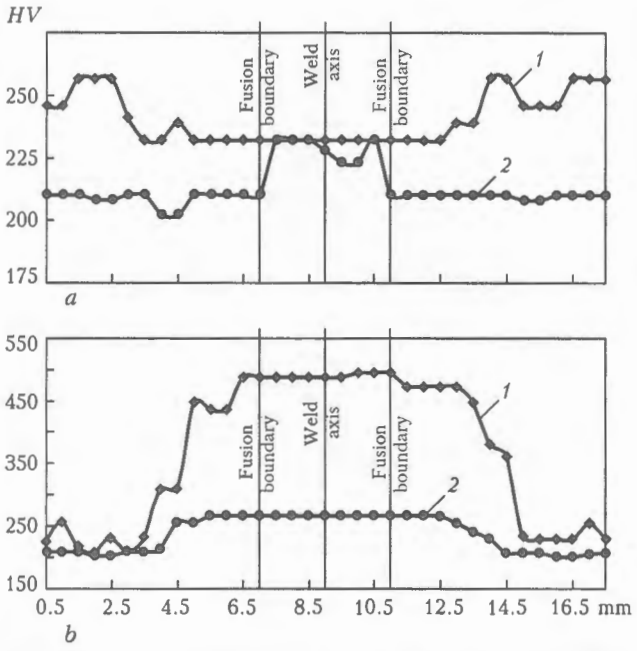

Figure 5. Hardness distribution in a joint on steel 18Kh11MNFBSh (*a*) and 08Kh16N13M2B (*b*) after EBW (*1*) and subsequent heat treatment (*2*)

other defects in the form of microcracks, looseness, or root defects were found in the welds either at ultrasonic testing or in metallographic investigations.

Thus, the proposed technology and parameters of the process of welding turbine packs made of high-chromium steels allowed ensuring a high quality and reliability of items, not using any means or techniques of their repair.

1. Nazarenko, O.K., Kajdalov, A.A. et al. (1987) *Electron beam welding*. Kiev: Naukova Dumka.
2. Bondarev, A.A., Skryabinsky, V.V. (1987) Welding of aluminium alloys with programming of electron beam density distribution in the heating spot. In: *Automatic control of electron beam welding technological process*. Kiev: PWI.

TECHNOLOGICAL PECULIARITIES OF ARGON-ARC WELDING AND BRAZING FOR REPAIR OF CAST BLADES OF MULTICOMPONENT HIGH-CHROMIUM NICKEL ALLOYS

M.S. SAMOKHIN[1], G.F. MYALNITSA[1], V.A. KRESHCHENKO[1], S.M. SAMOKHIN[1] and Yu.G. DOBKINA[2]
[1]State Ukrainian Research&Production Complex for Gas Turbine Construction «Zarya-Mashproekt», Nikolaev, Ukraine
[2]Physico-Technological Institute of Metals and Alloys, NASU, Kiev, Ukraine

Structure of cast blades in the as-welded and heat-treated condition has been studied. Austenising of joints prior to welding provides their heat resistance (900 °C) at a level of base metal. Experimental examination of structure of regions in gas turbine engine blades repaired by welding and brazing has been conducted.

Keywords: *argon-arc welding, arc brazing, nickel alloys, welded joints, filler materials, eutectic phase, heat treatment, heat resistance, microstructure, repair of blades*

Blades and vanes of heat-resistant nickel alloys are the most critical parts of gas turbine engines (GTE). The need to develop repair technologies arises from a high cost of structural materials and sophisticated and power-extensive technologies used to manufacture blades [1]. The hot problem is repair of both new blades with casting defects and used blades, which were in service for a certain period of time.

As shown by information analysis, the majority of currently available technologies for repair of cast components of the GTE nozzle sections are based on the process of vacuum diffusion brazing using composite braze powders, sometimes in combination with remelting of metal to be repaired by the electron beam or hollow-cathode arc methods [2–5]. The use of this approach is partly attributable to difficulties associated with technological realisation of many recommendations [6, 7] on avoiding cracking of heat-resistant nickel alloys under the effect of electric arc heating, including preliminary or concurrent heating, or long-time multistage overageing.

Nevertheless, under the gas turbine manufacturing conditions, repair of blades is easier to perform using affordable, available and well-mastered technologies, such as argon-arc welding with local or general shielding of a part [8–10]. In this case the welding process is performed using a simple standard equipment, and characterised by the possibility of visual inspection and fitness for manufacture of a wide range of parts and components.

The probability of cracking can be efficiently reduced and sound joints in welding of heat-resistant nickel alloys can be provided by such well-known technological approaches as preweld heat treatment of base metal, use of a special composition of filler wire and minimal heat input of the arc [6, 7].

These technological approaches for argon-arc welding of multicomponent high-chromium heat-resistant alloys, the grades and compositions of which are given in Table 1, have been insufficiently studied, and no practical recommendations for these alloys are available in technical literature. This study, which is intended to expand the range of parts to be repaired by welding and optimise the repair technology, focuses on the effect of composition of filler materials and parameters of heat treatment of base metal before and after manual argon-arc welding at currents of 80–100 A on heat resistance of butt welded joints in 4–5 mm thick cast plates of alloys EK9-VI and ChS104U-VI.

System analysis of regularities of structural-phase transformations occurring in alloys of parts to be repaired is important for assigning parameters of heat treatment of welded joints.

Analysis of the data accumulated by «Zarya-Mashproekt» on structural-phase composition of metal of the used cast blades shows that the most intensive fracture of the working surface and negative changes in metal structure occur in the airfoil part of blades. The most characteristic types of defects found in blades of different stages of GTE, made from high-chromium cast alloys EK9-VI, ChS104U-VI and ChS88U-VI, after operation at a temperature of 850–950 °C are as follows:

- regions of corrosion damage on working surfaces and wear of base metal in the hottest zones of fracture of protective coatings;
- structural changes of base metal, which show up in formation of continuous films by carbides $Me_{23}C_6$ and Me_6C and the eutectic γ'-phase at grain boundaries, as well as a «network» of the laminated σ-phase precipitates in the matrix (Figure 1, *a*), with increase in the total amount and oriented coagulation of the γ'-phase.

Welding of heat-resistant nickel alloys may involve initiation of hot microcracks at the inter-crys-

Table 1. Chemical composition of cast nickel alloys

Alloy grade	Content of basic elements, wt.%					
	Cr	W	Mo	Co	Ti	Al
EK9-VI	19.0–20.0	2.5–4.0	3.0–4.0	4.0–6.0	2.0–3.0	3.0–4.0
ChS104U-VI	20.0–21.8	3.0–4.0	0.3–0.9	10.3–12.0	3.1–3.9	2.1–2.9
IN738LC	16.0	2.6	1.75	8.5	3.4	3.4

Table 1 (cont.)

Alloy grade	Content of basic elements, wt.%					
	Nb	Ta	Zr	Hf	C	B
EK9-VI	1.4–2.0	–	–	–	0.10–0.15	0.12
ChS104U-VI	0.15–0.35	–	0.03–0.05	–	0.07–0.14	0.015
IN738LC	2.0	1.2	0.1	–	0.17	0.17

Note. Here and in Table 2 nickel is the base of all the alloys.

talline boundaries of the HAZ in regions of melting of the metastable phases, clustering of intermetallic compounds characterised by unfavourable morphology and microporosity [7].

Degradation of the working surface and internal structure of metal of blades during operation leads to substantial deterioration of their repairability by arc welding, as carbide fringing of grain boundaries and laminated σ-phase precipitates favour development of cracks. The fact that the as-cast metal contains a large amount of liquation colonies based on complex eutectic ($\gamma + \gamma' + MeC + Me_3B_2$) along the grain boundaries and carbide inclusions of an unfavourable shape (Figure 1, *b*) also has a negative effect on crack resistance of blades in argon-arc welding repair of surface defects. Apparently, the blade metal should be subjected to preweld heat treatment to decrease the concentration of coarse structural components at the grain boundaries after casting or service and, thus, improve its crack resistance.

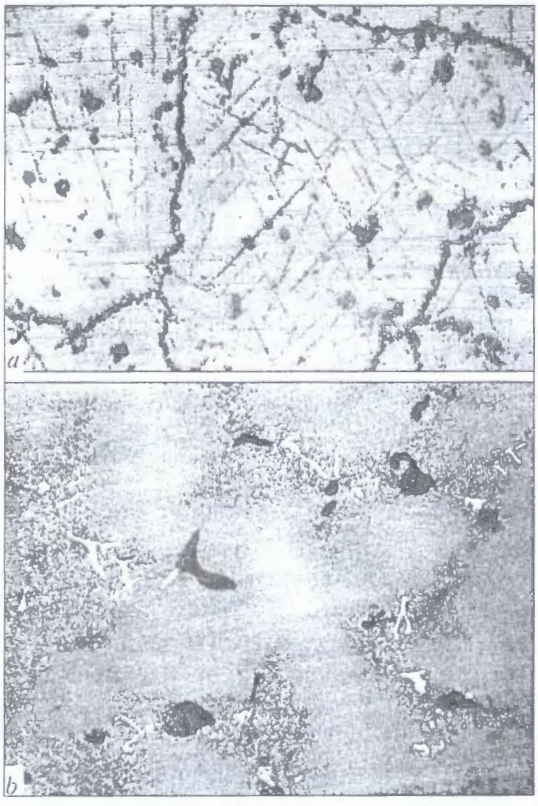

Figure 1. Microstructure of metal of blade airfoil made from alloy ChS88U-VI after operation for 21690 h (*a*) (×400); ChS88NK in as-cast condition (*b*) (×200)

Currently, there is no single opinion concerning the efficiency of the influence of homogenising or overageing of heat-resistant alloy prior to welding on its weldability. The use of this heat treatment or the other depends upon the fact whether the amount of phases providing relaxation resistance of alloy or leading to formation of cracks and melting of grain boundaries during welding decreases or not.

It has been experimentally found that high-temperature austenising (homogenising) of multicomponent high-chromium heat-resistant alloys EK9-VI and ChS104U-VI prior to manual argon-arc welding, combined with complete standard or partial stepwise ageing after welding, provides increased values of short- and long-time strength of the joints at a temperature of 900 °C (Figure 2), compared with other known standard types of preweld heat treatment. In this case fracture of welded specimens in testing almost always occurs in the weld, which is an indirect indication of the absence of cracks in the HAZ metal both in the as-welded condition and after postweld heat treatment.

With other types of preweld heat treatment of metal the joints have lower heat resistance, and welded specimens fracture primarily in the HAZ. This is attributable to a substantial decrease in deformation ability of the HAZ metal under the effect of welding heat, because of an extra precipitation of the finely dispersed γ′-phase, coarsening of morphology of inclusions of the primary γ′-phase and carbides, and probable precipitation of topologically closely packed

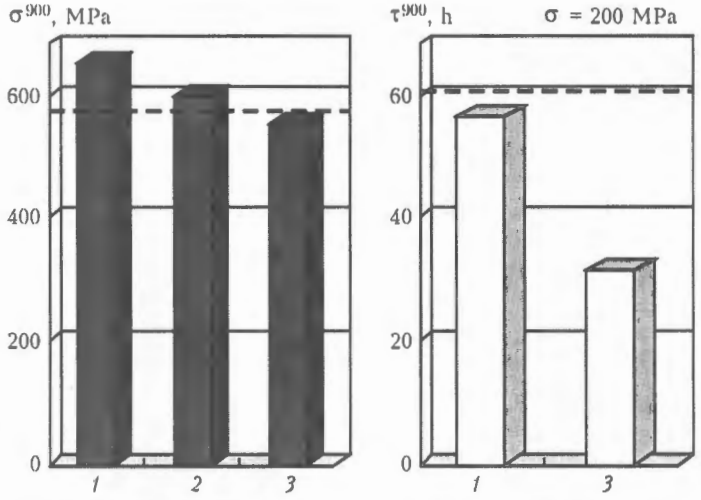

Figure 2. Heat resistance of welded joints in alloy ChS104U-VI: *1* — austenising–welding–quenching+ageing; *2* — austenising–quenching+ageing–welding; *3* — austenising–quenching+ageing–welding–quenching+ageing; *dashed line* — parameters for base metal

(TCP) phases along the boundaries and in the bulk of grains.

The types of heat treatment studied have similar effect on properties of welded joints in alloys ChS88U-VI, IN738LC, ChS70-VI and GT2100. Standard welding wires EI868, EP367, EP595, EP648-VI, EP533, etc., alloyed with chromium, molybdenum and tungsten (Table 2), are usually used for welding repair of defects in cast heat-resistant nickel alloys.

Practical verification of the EP595 type wires with a high molybdenum concentration in argon-arc welding of blades at low values of heat input shows that high toughness of molten filler metal and poor wettability of the surface and penetration of base metal edges with the weld pool metal lead to formation of pores, cavities and lacks of fusion of the weld layers. High-chromium wires EP533, EP648 and EP868 provide the higher quality in welding and cladding.

Expected strength properties of deposited metal in argon-arc welding of defects in blades using standard welding wires are difficult to evaluate, as only mechanical properties of wires in the deformed condition are known. No data are available on strength properties of metal of such wires after arc remelting and ageing.

Mechanical properties of metal deposited with these wires were determined. Comparative strength tests of metal of the wires were conducted on specimens of ingots subjected to ageing (T = 850 °C, 16 h, air cooling) after argon-arc remelting in a water-cooled copper crucible. Results of the tests shown in Figure 3 demonstrate that metal deposited with wire EP533 has the highest strength at 20 and 800 °C. The trend was detected to decrease in ductility of deposited metal with increase in the concentration of chromium in the wires, which is characteristic of Cr-containing nickel alloys [11].

High concentration of chromium in wires EP533, EP868 and EP648 guarantees the level of resistance of deposited metal against oxidation and high-temperature corrosion at a temperature of 800–1000 °C that is not lower than that of alloys EK9-VI and ChS104U-VI. Nevertheless, the maximal concentration of the γ'-phase in deposited metal is normally not in excess of half of its content of the base metal. Allowing for a too high total concentration of chromium, molybdenum and tungsten, the weld metal will differ from the base metal in a lower rate of precipitation of the γ'-phase and high susceptibility to precipitation of the TCP phases. These factors make it difficult to provide repaired regions with performance equal to that of the base metal. In addition, as precipitation and dissolution of the γ'-phase in nickel alloys are accompanied by volume changes of metal [12], operation of a blade for a certain period of time

Table 2. Chemical composition of filler materials

Steel grade	*Content of basic elements, wt.%*							
	Cr	*W*	*Mo*	*Ti*	*Al*	*Nb*	*C*	*B*
Sv-KhN75MBYuT (EI602)	19.0–22.0	–	1.8–2.3	0.35–0.75	0.35–0.75	0.9–1.3	0.10	–
Sv-KhN60VT (EI868)	23.5–26.5	13.0–16.0	–	0.3–0.7	≤ 0.5	–	0.01	–
Sv-06Kh15N60M15 (EP367)	14.0–16.0	–	14.0–16.0	–	–	–	0.08	–
Sv-Kh11N60M23 (EP595)	9.0–13.0	–	21.5–24.5	–	–	–	≤ 0.10	–
Sv-Kh50VMTYuB (EP648)	32.0–35.0	4.3–5.3	2.3–3.3	0.5–1.5	0.5–1.1	0.5–1.1	≤ 0.06	≤ 0.008
Sv-08Kh20N57M8V8T3R (EP533)	19.0–22.0	7.0–9.0	7.0–9.0	2.3–2.9	≤ 0.4	–	≤ 0.10	≤ 0.005

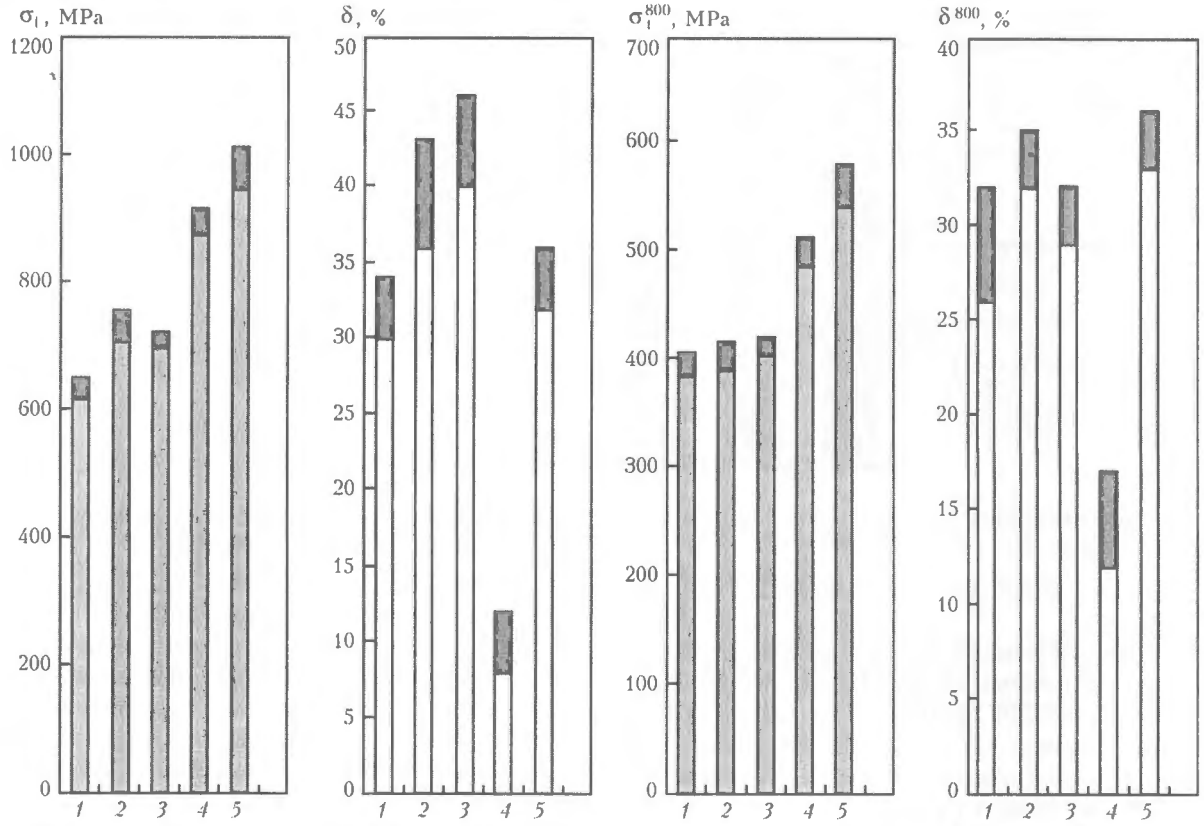

Figure 3. Mechanical properties of metal of Cr–Ni welding wires after argon-arc remelting and ageing (T = 800 °C, 16 h): *1* — EI602; *2* — EI868; *3* — EP367; *4* — EP648; *5* — EP533

under the thermal cycling conditions will involve cracking of the repaired region [10, 13].

To eliminate cracking during welding, specialists recommend to increase the concentration of boron, niobium, zirconium or hafnium in alloys of different alloying systems in order to improve morphology of carboboride phases along the grain boundaries or cause formation of a two-phase structure with a multicomponent eutectic phase in the weld metal [6, 14–18]. Both filler wires and structural heat-resistant alloys of nickel with boron and niobium are considered to be technologically mastered [14–18]. Concentrations of the above elements that provide formation of a sufficient amount of the eutectic phase in the deposited metal to avoid cracking during welding are 0.35–0.65 % B and 4.0–7.0 % Nb [14, 18]. Note that the addition of more than 0.1 % B or more than 2.0 % Nb has a negative effect on high-temperature corrosion resistance of Cr–Ni alloys [19–23]. Moreover, the presence of the above elements in alloy in an amount exceeding their solubility limits leads to precipitation of individual coarse intermetallic phases, destabilises phase equilibrium in heat-resistant alloys and deteriorates heat resistance and metallurgical compatibility with protective coatings [23, 24].

The idea of using eutectics with zirconium to improve weldability and avoid hot cracking in arc welding of Cr–Ni steels and alloys was first put forward in study [14]. Microalloying with zirconium and hafnium was investigated for multicomponent high-chromium nickel alloys of the type of EK9-VI and ChS104U-VI. However, until now no systematic investigations have been conducted to study the effect of alloying using more appreciable concentrations of zirconium or hafnium on phase composition, structure and weldability of the above alloys.

Practice of collaborative efforts with the Admiral Makarov Ukrainian State Marine Technical University (Nikolaev), E.O. Paton Electric Welding Institute and G.V. Kurdyumov Institute of Metal Physics of the NAS of Ukraine proved the possibility and efficiency of using the known Zr-containing multicomponent nickel brazes [25, 26] for argon-arc repair of defects in cast blades. The efforts also showed the impossibility to ensure consistent resistance of deposited metal against formation of cracks and pores.

Adjustment of the deposition process parameters and compositions of Zr-containing filler metals with allowance for the requirements of repair technologies using arc heating led to the development and investigation, in collaboration with the E.O. Paton Electric Welding Institute and G.V. Kurdyumov Institute of Metal Physics, of new experimental compositions of filler materials with increased concentrations of zirconium, chromium and other elements that form eutectic with nickel [27–29]. This allowed formation of the required amount of the multicomponent eutectic phase in melting, which is characterised by a high ability to intergranular migration and metallurgical compatibility with base metal. Combination of alloying elements and their concentrations in new filler materials were chosen on the basis of known recommendations for ensuring resistance of nickel alloys of transportation GTE against high-temperature salt cor-

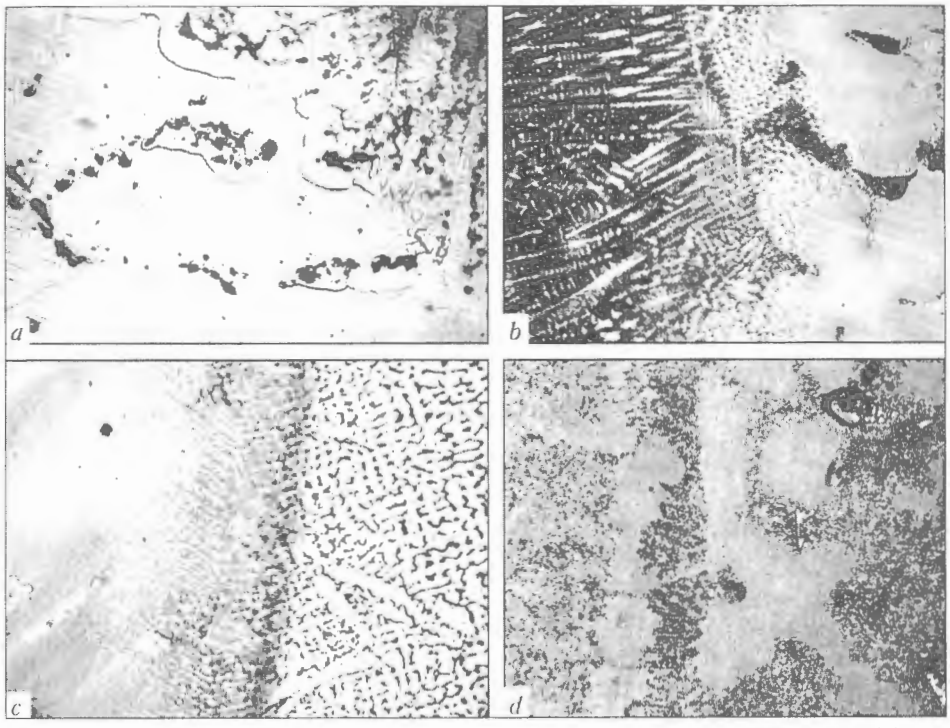

Figure 4. Structure of the fusion zone in welding repaired regions on blades made from alloys ChS104U-VI (*a*) and ChS88NK (*b–d*): *a* – wire Sv-08Kh20N57M8V8T3R (EP533) (×400); *b–d* – experimental filler materials based on the Ni–Cr–Zr system, after arc welding (brazing) (*b, c*) and after standard postweld heat treatment (*d*) (×200)

rosion, compatibility with protective coatings and heat resistance [20, 30], as well as minimal range of solidification of deposited metal.

Repair of surface and through defects by argon-arc welding using eutectic fillers was performed on experimental castings and mass-produced blades of alloys EK9-VI and ChS104U-VI.

Unlike homogeneous welding wires, which provide formation of a smooth fusion line with local incipient melting of the base metal grain boundaries in welding (Figure 4, *a*), the interface formed in cladding using fillers with the Zr-containing eutectic phase comprises many «passages» along the grain boundaries in the HAZ (Figure 4, *b, c*), filled with liquid metal. Liquid phase «refines» the base metal grain boundaries. Eutectic causes splitting and dissolution of coarse carbide inclusions, colonies of the eutectic γ'-phase and other intermetallics to a depth of 10–40 μm. These factors improve homogeneity, high-temperature ductility and resistance of the HAZ metal of heat-resistant alloys to cracking during welding.

Experimental multicomponent high-chromium filler materials based on the Ni–Cr–Zr master system used for argon-arc brazing provide quality formation of the repaired regions on blades, independently of the type of preweld heat treatment, including in cladding with no preheating.

It has been experimentally proved that, despite the presence of the eutectic phase with a melting point of 1090–1155 °C in the intercrystalline regions of deposited metal, homogenising of parts after cladding provides an efficient improvement in homogeneity of the repaired metal (Figure 4, *d*).

According to the X-ray microanalysis data, the multicomponent intermetallic phase close in composition to a compound of the $Ni_7(Zr, Ti)_2$ type was revealed in the eutectic colonies along the deposited metal grain boundaries with 9–15 % Zr. No such phase was revealed after heat treatment. Noted also is a decreased total amount of carbides $Cr_{23}C_6$ in the deposited metal, as well as an increased content of carbides MeC, in which the zirconium concentration amounts to 40–80 %. In this case zirconium favours substantial refining of dendritic structure and modification of the carbide phase in deposited metal. Phase composition of the latter and its resistance to high-temperature corrosion are close to base metal.

Similar character of interaction and structure formation was revealed in arc brazing of alloys ChS88U-VI, ChS70-VI, IN738LC and GT2100, using experimental Zr-containing fillers.

Currently, the new filler materials with the Zr-containing eutectic phase have passed technological verification in repair of cast blades of different GTE stages. Compositions providing heat and corrosion resistance of deposited metal on blades with oriented solidification structure have been specified. The investigation and test results allowed development of technological recommendations, substantiation of parameters for repair of cast GTE blades, and increase in volumes of repair of defective cast blades and blades that were in use as part of GTE.

CONCLUSIONS

1. It has been established that after service at a temperature of 850–950 °C as part of GTE, as well as in the as-cast condition, mulitcomponent high-chro-

mium heat-resistant nickel alloys are characterised by formation of continuous films at the intercrystalline boundaries, as well as coarse precipitates based on chromium carbides, $\gamma + \gamma'$ eutectic and TCP phases, which leads to cracking and makes it difficult to repair service and casting defects in blades by argon-arc welding.

2. Technological verification of standard filler wires alloyed with molybdenum, tungsten and chromium, used for argon-arc welding of cast blades of alloys EK9, ChS70-VI, ChS88U-VI and ChS104U-VI showed that a minimal amount of defects and high resistance of deposited metal to high-temperature corrosion are provided by using wires EP533, EP868 and EP648.

3. Austenising (homogenising) of base metal prior to welding, compared with other types of heat treatment, provides high heat resistance of welded joint at 900 °C, similar to that of base metal, including in using standard high-chromium welding wires.

4. New multicomponent filler materials with the Zr-containing eutectic phase, which provides dissolution of unfavourable structural components along the grain boundaries in the HAZ metal and quality formation of the repaired regions in blades, independently of the type of preweld heat treatment, were developed and tested under industrial conditions in repair of cast blades of different GTE stages.

1. Myalnitsa, G.F. (1999) Peculiarities of the process of manufacture of turbine blades from high-chromium heat-resistant nickel-based alloys. *Izvestiya AINU*, **1**, 266–269.
2. Arzhakin, A.N., Stolyarov, I.I., Yazovskykh, V.M. et al. (1998) Technology for reconditioning aircraft engine stator blades by brazing and electron beam remelting. *Svarochn. Proizvodstvo*, **3**, 27–29.
3. Rylnikov, V.S., Shatov, A.P., Tsaryov, V.I. (2000) Technology for repair of gas-turbine engine stator blades. In: *Abstr. of pap. of Int. Conf. on Welded Structures*, Kiev, Oct. 2000.
4. Nerovny, V.M., Yampolsky, V.M., Rogov, R.M. (1989) Repair of gas-turbine blades by vacuum arc brazing. *Energomashinostroenie*, **2**, 22–24.
5. Kvasnitsky, V.V., Kostin, A.M., Kvasnitsky, V.F. et al. (1995) Technology for brazing repair of casting defects in heat-resistant alloys. In: *Proc. of Russian Sci.-Techn. Conf. on Current Problems of Welding Science and Technique «Welding-95»*, Perm, Oct. 1995. Part 1. Perm: PGTU.
6. Medovar, B.I. (1966) *Welding of heat-resistant austenitic steels and alloys*. Moscow: Mashinostroenie.
7. Zemzin, V.N. (1972) *Heat resistance of welded joints*. Leningrad: Mashinostroenie.
8. Pinchuk, N.I., Khorunov, V.F., Zakharov, L.S. et al. (1998) Welding repair of casting and service defects in gas-turbine blades from heat-resistant nickel alloys. In: *Proc. of Int. Conf. on Welding and Related Technology for the 21st Century*, Kiev, Sept. 1998. Kiev: PWI.
9. Sorokin, L.I., Lukin, V.I., Bagdasarov, Yu.S. (1997) Weldability of cast heat-resistant nickel alloys of the JS 6 type. *Svarochn. Proizvodstvo*, **6**, 12–17.
10. Sorokin, L.I., Fyodorov, B.M. (2002) Welding repair of marking holes in turbine blades from JS 26 alloy VSNK. *Ibid.*, **8**, 34–37.
11. Bulat, S.I., Tikhonov, A.S., Dubrovin, A.K. (1975) *Deformability of structurally inhomogeneous steels and alloys*. Moscow: Metallurgiya.
12. Zhetvin, N.P., Frid, Ya.L., Kontsevaya, E.M. et al. (1966) Study of kinetics of strengthening and weakening of heat-resistant alloys to select hot plastic deformation and heat treatment temperature range. In: *Transact. on Welding and Applications of Heat-Resistant Alloys*. Moscow: Nauka.
13. Savchenko, V.S., Yushchenko, K.A., Savolej, N.I. et al. (1993) Peculiarities of welding of high-nickel precipitation-hardening heat-resistant alloys and repair of items made from them. *Avtomatich. Svarka*, **10**, 31–33.
14. Medovar, B.I., Pinchuk, N.I., Chekotilo, L.V. (1970) *Austenite-boride steels and alloys for welded structures*. Kiev: Naukova Dumka.
15. Zimina, L.N. (1977) Weldable heat-resistant nickel alloys and principles of their alloying. *Metallovedenie i Term. Obrab. Metallov*, **11**, 2–7.
16. Makushek, O.V., Tashchilov, V.S., Melnikov, N.A. (1985) Improvement of weldability of heat-resistant alloys of the KhN67MVTYu type by alloying with Nb, Hf, Ta, Re. In: *Transact. on Influence of Alloying and Heat Treatment on Properties of High-Quality Steels and Alloys*. Moscow: Metallurgiya.
17. Sorokin, L.I., Erokhin, A.A., Kuznetsov, O.M. (1971) Influence of rhenium, niobium and tantalum on mechanical properties of deposited metal. *Avtomatich. Svarka*, **12**, 61–62.
18. Yushchenko, K.A., Pinchuk, N.I., Danilyak, A.G. et al. *Welding wire composition*. USSR author's cert. 1425012. Int. Cl. B 23 K 35/30. Publ. 23.09.88.
19. Kireev, V.B. (1987) Steels and alloys for high-temperature service. In: *Heat-resistant and heat-temperature metallic materials*. Moscow: Nauka.
20. Gajduk, S.V., Belikov, S.B., Koval, A.D. (1988) Principles of development of high-corrosion-resistant alloys. In: *Transact. on New Structural Materials and Effective Methods for their Production and Treatment*. Kiev: UMK VO.
21. Kostyrko, O.S., Myalnitsa, G.F., Voloshchenko, N.I. et al. *Heat- and corrosion-resistant nickel-based alloy*. USSR author's cert. 959443. Int. Cl. C 22 C 19/05. Publ. 30.10.90.
22. Peremuzov, E.P., Stepanov, V.M., Kononova, E.G. et al. *Cast heat-resistant nickel-based alloy*. USSR author's cert. 677531. Int. Cl. C 22 C 19/05. Publ. 15.11.90.
23. Eliseev, Yu.S., Abramov, N.V., Krymov, V.V. (1999) *Chemical heat treatment and protective coatings in aircraft engine manufacturing*. Moscow: Vysshaya Shkola.
24. Khimushin, F.F. (1969) *Heat-resistant steels and alloys*. Moscow: Metallurgiya.
25. Kvasnitsky, V.F., Ignatov, V.A., Zabolotsky, V.M. et al. *Brazing filler metal for heat-resistant alloys*. USSR author's cert. 1544541. Int. Cl. B 23 K 35/32. Publ. 23.02.90.
26. Khorunov, V.F., Ukader, E.M., Zubchenko, V.P. *Filler metal for brazing heat-resistant nickel alloys*. USSR author's cert. 1743773. Int. Cl. B 23 K 35/32. Publ. 30.06.92.
27. Samokhin, S.M., Kvasnitsky, V.F., Khorunov, V.F. et al. *Brazing filler metal*. Pat. 43903 Ukraine. Int. Cl. B 23 K 35/32. Publ. 15.01.02.
28. Khorunov, V.F., Maksymova, S.V., Samokhin, M.S. et al. (2000) Brazing filler metals containing Zr and Hf used as depressants. In: *Abstr. of pap. of 3rd Int. Conf. on High Temperature Capillarity*, Kurashiki, Japan, Nov. 19–22, 2000.
29. Khorunov, V.F., Maksymova, S.V., Zvolinsky, I.V. et al. (2000) Arc brazing of heat-resistant nickel alloys. In: *Proc. of Int. Brazing and Soldering Conf.*, Albuquerque, New Mexico, April 2–5, 2000.
30. Nikitin, V.I. (1987) Prospects of protection of nickel alloys from sulphide-oxide corrosion. In: *Heat-resistant and high-temperature metallic materials*. Moscow: Nauka.

IMPROVEMENT OF DESIGNS OF INDUCTORS FOR INDUCTION SURFACING OF THIN ELEMENTS OF MACHINE PARTS

O.N. SHABLY[1], Ch.V. PULKA[1], A.S. PISMENNY[2] and M.V. SHARIK[1]
[1]Ivan Pulyuj State Technical University, Ternopol, Ukraine
[2]E.O. Paton Electric Welding Institute, NASU, Kiev, Ukraine

Existing designs of inductors for induction surfacing of thin elements of flat parts, including shaped discs, are considered and analyzed. New designs of inductors and heating systems developed by the authors to reduce the energy content to improve the surfacing process efficiency and deposited metal quality, are described for induction surfacing of thin steel toothed discs.

Keywords: *induction surfacing, brazing, designs of inductors, heating system, flat parts, discs, surfacing efficiency, steel and ferrite magnetic cores, electromagnetic and heat screening*

In various branches of economy, in agricultural machinery in particular, the thin flat parts, including thin shaped discs with a toothed and solid working surface, are used as operating organs of earth-moving machines. To increase the wear resistance, their working surfaces are subjected to surfacing with powdered hard alloys (charge) using high-frequency currents. Here, the thickness of the deposited metal is 0.3–2.5 mm. The following equipment is used for surfacing: generators, devices for fastening parts and charge feeding, mechanisms for loading and unloading of parts before and after surfacing, and also inductors.

Special requirements are specified to the designs of inductors, having an influence on the energy content, process efficiency, and also the deposited metal quality. More often they are selected experimentally separately for each new design of the part.

Capacity of heat sources in the zone of surfacing can be adjusted, as was mentioned above, by selection of the design of inductors, their sizes and distance to the part. But in some cases, depending on configuration of surface subjected to surfacing, it is very difficult to adjust capacity in width of the surfacing zone by varying only the inductor design. For this purpose it is necessary to develop the another methods and devices for heating, heating systems, with the help of which it is possible to control the electromagnetic field (capacity) in the zone of surfacing. The present work is devoted to the analysis of existing designs of inductors and development of the new designs.

Let us consider the designs of inductors for the induction surfacing and heat treatment of thin flat parts, including discs.

At present there is a large number of various designs of inductor for heating parts for quenching or surfacing. Nevertheless, the continuously changing and increasing nomenclature of parts subjected to surfacing, continuous improvement of the process require the careful selection or design of special inductors. Dimensions and shape of inductors for the induction surfacing of different parts, and also parameters of heating condition for each definite part are selected experimentally.

The main operating current frequency, at which the surfacing of thin flat parts (including discs of 2–6 mm thickness) is performed using induction method, is 440, and for larger thickness of the parent metal it is 70 kHz.

Figure 1, *a* presents a looping single-turn inductor for simultaneous surfacing of one cutting edge of central shovels of cultivator at current frequency of 70 kHz. To increase the heating temperature at the area (of 1.2 mm thickness) of the cutting edges the upper branch of the inductor is shifted as regards to the lower branch by 6 mm. The nose part of the shovel is made thick, therefore it is elongated at the area of surfacing. In this case there is no shifting of the branches. A base surface for fixation of parts in the inductor is an asbestos plate.

Figure 1, *b* shows a looping inductor for surfacing of plough shares. A circular expansion serves for levelling the distribution of electromagnetic field at a plough share cut edge and simplification of the inductor adjustment. A bushing-type inductor (Figure 1, *c*) is designed for surfacing the wedge-shaped plough shares in mechanized installations.

Three-turn oval inductor (Figure 1, *d*) is used for the continuous-successive surfacing of blades of exhausters, and a circular single-turn inductor (Figure 1, *e*) — for surfacing of cutting edges of discs of surface plows.

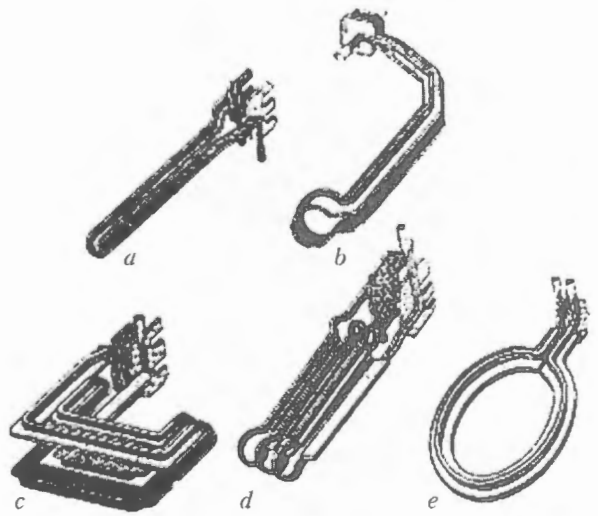

Figure 1. Designs of inductors for surfacing of machine flat parts [1]

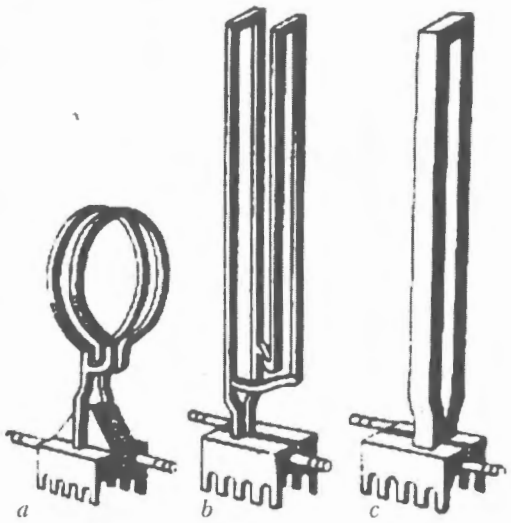

Figure 2. Inductors for brazing of disc-type cutters [2]: *a* — with two turns connected in parallel; *b* — rectangular with an inverted parallel turn (magnetic fluxes in turns are opposite directed); *c* — looping

Figure 2 shows the designs of inductors for brazing of disc-type cutters with the help of which the required distribution of electromagnetic field in the zone of brazing is attained [2]. Single- and multiturn inductors whose turns are located in one plane (Figure 3), are used for heat treatment and surfacing of flat working surfaces [3].

Analysis of described designs of inductors showed that they have a low efficiency factor due to a weak coupling between the electromagnetic field of inductor and the part. In addition, in some cases it is insufficient or very difficult to control the power in the zone of surfacing only by varying the design of the inductor (electromagnetic field) due to intricate geometric shape of the surface and also with the allowance for automation of the technological process of surfacing.

To decrease the losses by limiting the dissipation of the electromagnetic field and increase in its concentration in the zone of surfacing, the magnetic cores are also used, the use of which in applying to active parts of the inductor from one or two sides allows concentration of electromagnetic field at the preset area of the part surface being deposited.

Magnetic cores are manufactured from the sheets of transformer steel or ferrites. Section of inducting wire with a magnetic core, made from transformer steel, is shown in Figure 4. If to apply this induction system, then the current concentration under the inductor will increase significantly.

In work [4] a new design of the magnetic core has been suggested, the use of which in applying to active parts of the inductor from one or two sides allows concentration of magnetic field at the preset area of heating of the part being deposited and increasing the speed of deposition by more than 20 % as compared with surfacing without the magnetic core.

In surfacing of wedge-shaped shares in inductors without magnetic core the process of charge melting at the nose is lagging from that at the cutting edge by 3–5 s. When surfacing with magnetic core the advance in charge melting at the nose is observed that gives an opportunity to mechanize or automate the process of surfacing the plough shares.

In this case the magnetic cores are manufactured in the form of packs assembled of plates of 0.1 mm thick electrical thin sheet steel of E44 grade. Schematic diagram of the inductor with a magnetic core is presented in Figure 5. The use of this magnetic core makes it possible to increase significantly the output of parts being surfaced at decrease in losses of electric energy and reduction in time for surfacing.

Magnetic cores can be used successfully in equipment of factories of tractor and agricultural machine-building.

Technology of induction surfacing of thin steel discs with use of ferrite and steel magnetic cores is described in works [3, 4, 6]. Figure 6 shows a scheme of device for surfacing solid discs using a ferrite magnetic core [7]. However, it is very difficult to control the power in the zone of surfacing of thin discs of a toothed shape at a larger width of deposition than a tooth height using magnetic cores.

The application of single-turn circular inductors without and with magnetic cores (Figure 1, *e*; 2, *c*; 6) for simultaneous surfacing over the entire working surface of thin steel toothed discs to increase the process efficiency encounters difficulties in providing the uniform distribution of electromagnetic field in the area of surfacing that has a negative influence on the quality (uniformity) of thickness of the deposited metal.

Drawbacks of two-looped inductor, as well as segment inductor, are as follows: comparatively low efficiency, distortion of part due to a local heating, and

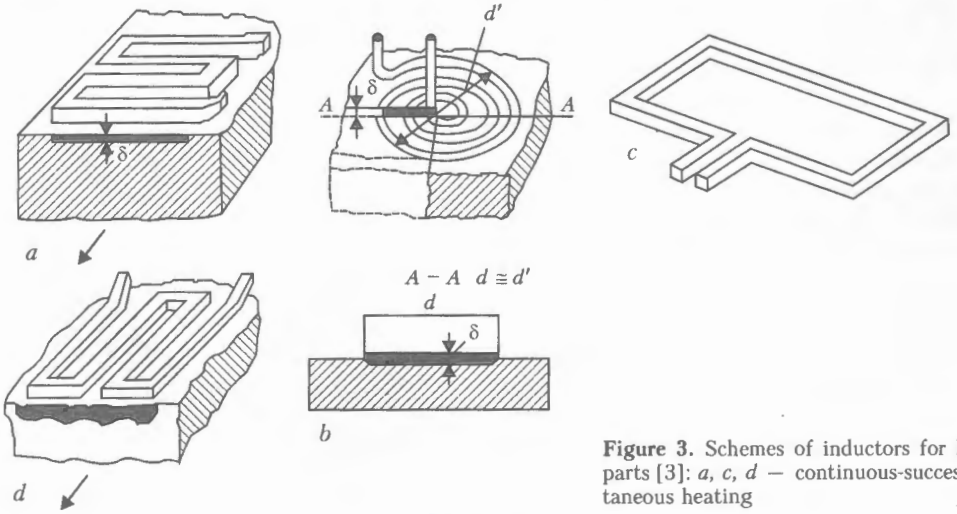

Figure 3. Schemes of inductors for heating thin flat parts [3]: *a*, *c*, *d* — continuous-successive; *b* — simultaneous heating

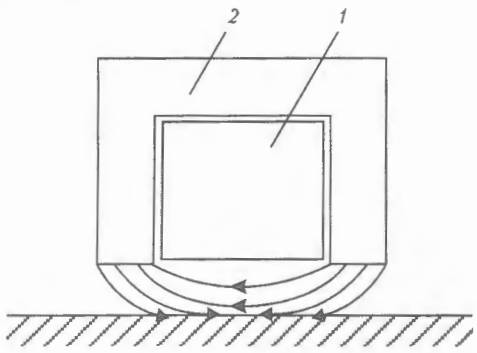

Figure 4. Section of inducting wire (*1*) with a magnetic core (*2*) made from transformer steel [4]

also impossibility to use it for a simultaneous surfacing over the entire surface of thin toothed discs with a larger width of deposition than the tooth height.

The known two-turn (see Figure 2, *a*) inductors with a similar diameter of rings do not allow their use in mechanization of the process of surfacing shaped toothed discs with a projection in their middle part.

Authors have developed the two-turn circular inductors (Figure 7) [8, 9] with different diameters of circular turns and areas of their transverse sections of rectangular and circular shape. Here, the diameter of the lower turn is located under the surface being deposited and the upper turn is located above it (Figure 7). Respectively, the diameter of the lower turn is smaller and diameter of upper turn is larger than the disc diameter; area of transverse section of the lower turn is larger than the area of transverse section of the upper turn. This creates the feasibility for automation of the process of feeding the blanks from the top in charge loading and surfacing of the disc.

Mathematical model and algorithm have been developed, graphical relationships and table data are plotted, according to which the design sizes of a two-turn circular inductor for orbitrary diameters of discs and width of surfacing zone with the allowance for the technology requirements are selected. Calculations of engineering results, published in [10, 11], are made.

As the theoretical and experimental investigations showed, overheating of disc edge and deposited metal occurs in surfacing of thin toothed discs with a width larger than a tooth height using a two-turn circular inductor, that influences the quality of the product as a whole.

In practice of induction heating to provide a necessary distribution of power in the width of surfacing zone, and also to protect the separate areas of the part from overheating in action of the electromagnetic field

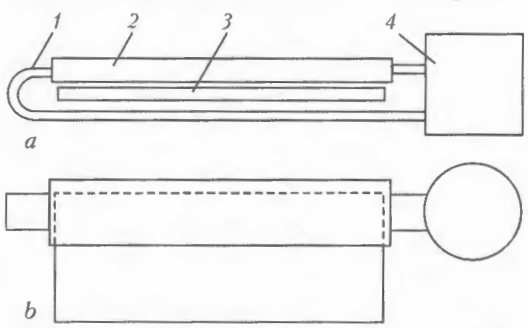

Figure 5. Scheme of inductor with a magnetic core [5] from the side (*a*) and from the top (*b*): *1* — inductor loop; *2* — magnetic core; *3* — part; *4* — high-frequency generator

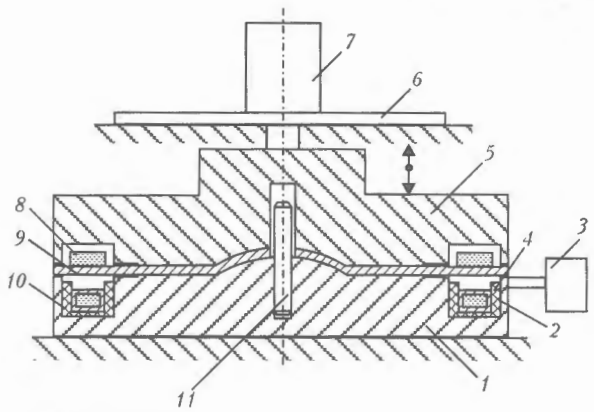

Figure 6. Scheme of unit for surfacing discs using a ferrite magnetic core [7]: *1, 5* — lower and upper pressure plates, respectively; *2* — copper electromagnetic screen; *3* — high-frequency generator; *4* — ferrite magnetic core; *6* — upper support; *7* — pneumatic drive; *8* — powdered hard alloy; *9* — solid thin disc; *10* — circular single-turn inductor; *11* — guide

the screens are used. They are manufactured, as a rule, from a red copper with high values of electro- and heat conductivity and used successfully for tempering of rims of gear-boxes [3]. Figure 8 shows the mutual arrangement of inductor, gear and screen in the induction heating process.

Technology of induction heating using the screening of electromagnetic fields was used by the authors in the development of technology of induction surfacing of thin toothed discs to decrease the power generation at the disc edge and its uniform distribution in the width of the surfacing zone [12]. In work [12] the theoretical investigations of system for the optimization of design sizes of two-turn circular inductor with allowance only for screening of electromagnetic fields at accepted values of coefficients of screening K = 1, 0.25 and 0, were carried out.

To control the power in the zone of surfacing thin discs, the authors have suggested to use the screening of the electromagnetic field, generated by inductor, to attain the uniform distribution of power in the zone of surfacing [12]. However, as the theoretical and experimental investigations showed, the most effective distribution of power in the width of the surfacing zone is attained taking into account simultaneously both electromagnetic and

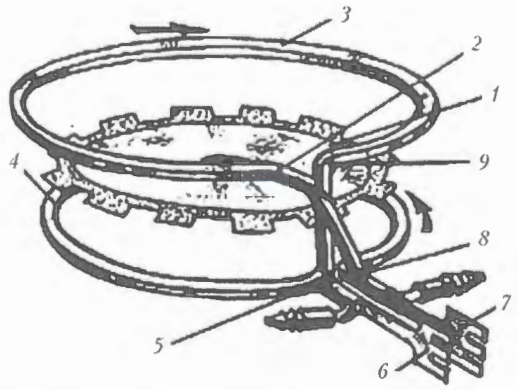

Figure 7. Two-turn inductor for surfacing thin toothed discs with a rectangular similar transverse section and different diameters of turns [8, 9]: *1* — disc; *2* — place of connection of upper turn *3* end with lower turn *4; 5* — place of connection of lower turn with a pipe connection for water supply; *6, 7* — left and right terminals, respectively; *8* — place of connection of lower turn to a pipe connection for water drain; *9* — place of connection of upper turn with lower turn

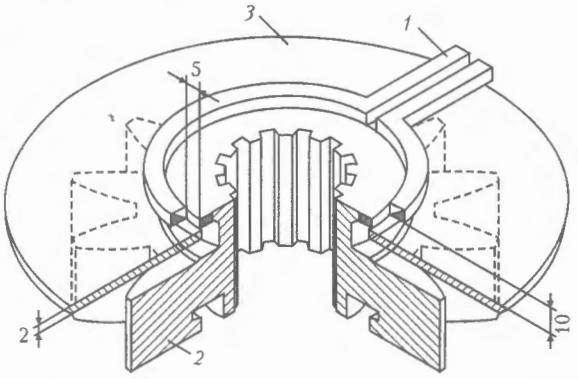

Figure 8. Scheme of mutual arrangement of inductor (*1*), gear (*2*) and electromagnetic screen (*3*) in the process of induction heating of gear-box rims for tempering [3]

heat screening (heat insulation of disc edge from environment). For this purpose the device [13] has been designed, which makes it possible to control the power in the zone of surfacing taking into account simultaneously both the electromagnetic and also heat screening, firstly, to attain the uniform thickness of deposited metal and, secondly, to realize the feasibility of automation of the technological process of induction surfacing of thin toothed discs.

The work [14] describes the mathematical model of heating system (Figure 9), designed for determination of temperature in the disc by the parameters of two-turn circular inductor, which was used for heating. The use of the combined electromagnetic and heat screening allows optimization of the mentioned temperature in the zone of surfacing of disc depending on the parameters of inductor, disc, electromagnetic and heat screens, and also electrical current in inductor. The developed algorithm allows also designing of the heating system (inductor, heat and electromagnetic screens), providing the necessary conditions for the fulfillment of the technological process of surfacing including the method of determination of coefficients of electromagnetic and heat screening with the help of which the control of temperature distribution in width of the surfacing zone with a complex geometry of the surface shape is realized.

The obtained results of calculation and experimental data of the heating system, developed by the authors, showed the feasibility of keeping the necessary law of distribution of temperature in width of the zone of surfacing to attain the uniform thickness of deposited metal in surfacing of knives of toothed beet-topping machines with a width of zone larger than the tooth height. Here, 15–25 % of electric energy is saved using the condition of heating with time according to the exponential law.

Thus, the analysis of existing designs of inductors showed that most effective technological process of simultaneous surfacing over the entire working surface of thin steel toothed discs is realized in use of the heating system consisting of an inductor, heat and electromagnetic screens.

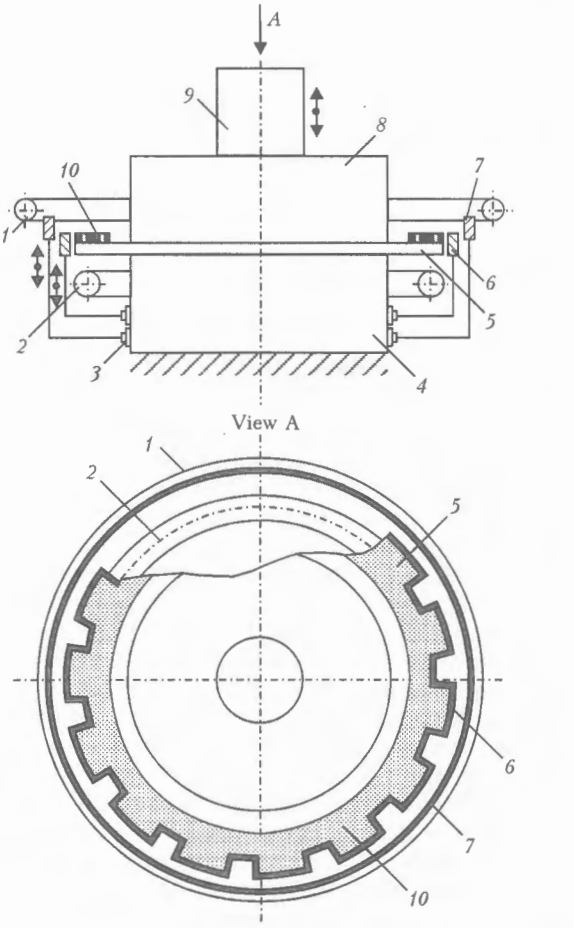

Figure 9. Scheme of device for control of power in the zone of surfacing with simultaneous screening of electromagnetic and heat fields [13]: *1, 2* — upper and lower turns of inductor; *3* — mechanism of screens displacement; *4* — lower plate; *5* — disc; *6, 7* — heat and electromagnetic screens, respectively; *8* — upper plate; *9* — pneumatic drive; *10* — charge

1. Tkachev, V.N. (1971) *Wear and improvement of service life of agricultural machine parts*. Moscow: Mashinostroenie.
2. Vologdin, V.V. (1965) *Brazing and hardfacing in induction heating*. Moscow-Leningrad: Energiya.
3. Lozinsky, M.G. (1958) *Industrial application of induction heating*. Moscow: AN SSSR.
4. Slukhotsky, A.E., Ryskin, S.E. (1974) *Inductors for induction heating*. Leningrad: Energiya.
5. Nilovsky, I.A., Suvorov, V.A., Stepanets, A.E. (1973) Improvement of productivity of induction hardfacing on operating elements of agricultural machines. In: *Coll. abst. on Welding Production*. Series Technology and Automation of Industrial Processes. Issue 1.
6. Pismenny, A.S., Pantelejmonov, E.A., Prokofiev, A.S. et al. (2000) Design of an inductor with a magnetic core for heating flat surfaces. *The Paton Welding J.*, **11**, 41–45.
7. Shably, O.M., Pulka, Ch.V. (2002) Study of induction hardfacing of thin shaped discs with magnetic core. *Visnyk TDU*, 7(4), 77–80.
8. Pulka, Ch.V., Shably, O.M., Budzan, B.P. et al. *Method of hardfacing of thin-walled shaped discs*. Pat. 55349 Ukraine. Int. Cl. B 23 K 13/00. Publ. 17.03.03.
9. Pulka, Ch.V., Shably, O.M., Budzan, B.P. *Device for hardfacing of flat thin-walled parts*. Pat. 55346 Ukraine. Int. Cl. B 23 K 13/00. Publ. 17.03.03.
10. Shably, O.N., Pulka, Ch.V., Budzan, B.P. (1988) Ways of energy saving in induction hardfacing of thin-walled discs. *Avtomatich. Svarka*, **12**, 56–58.
11. Shably, O.N., Pulka, Ch.V., Pismenny, A.S. (1997) Optimization of design parameters of inductor for induction hardfacing of thin steel discs. *Ibid.*, **6**, 17–24.
12. Shably, O.N., Pulka, Ch.V., Pismenny, A.S. (2002) Optimization of inductor parameters for uniform heating of discs across the width of the hardfacing zone, allowing for screening. *The Paton Welding J.*, **11**, 23–25.
13. Shably, O.M., Pulka, Ch.V., Pismenny, A.S. et al. *Device for control of power in hardfacing zone*. Pat. 58943A Ukraine. Int. Cl. B 23 K 13/00. Publ. 17.11.03.
14. Shably, O.N., Pulka, Ch.V., Pismenny, A.S. (2003) Optimization of induction hardfacing of thin discs allowing for thermal and electromagnetic shielding. *The Paton Welding J.*, **9**, 20–23.

SELECTION OF BORON-CONTAINING CHARGE MATERIALS FOR THE CORE OF FLUX-CORED WIRE

A.P. ZHUDRA, S.Yu. KRIVCHIKOV and **V.V. PETROV**
E.O. Paton Electric Welding Institute, NASU, Kiev, Ukraine

Results of experimental studies of the effect of different powdered boron-containing materials (amorphous boron, boron nitride, boron trioxide, boron carbide and iron-chromium-boron master alloy) contained in self-shielded flux-cored wire on structure, hardness and crack resistance of high-carbon deposited metal are given. It is shown that deposited metal alloyed with boron, using the iron-chromium-boron master alloy, has the most favourable physical-mechanical properties.

Keywords: *arc surfacing, flux-cored wire, deposited metal, microstructure, microalloying with boron, hardness of deposited metal*

It is a known fact that microalloying of foundry cast irons and carbon steels with boron can have a positive effect on some principal physical-mechanical properties of alloys [1]. As shown in [2], in electric arc surfacing of low alloys of the type of hypoeutectic white cast iron (2.2–2.5 % C) using flux-cored wire, microalloying with boron in an amount of 0.1–0.2 % favours growth of resistance of the deposited metal to cold cracking and its micro- and macrohardness, and leads to a substantial change in morphology of structural components of deposited white cast iron.

The purpose of this study is to evaluate efficiency of the effect exerted by microalloying with boron on the above properties of deposited cast iron when adding cast iron to a composition of the core of self-shielded flux-cored wires in the form of different B-containing materials. Surfacing using flux-cored wire 1.8 mm in diameter was performed on samples of steel St.3 by depositing individual beads in four layers at a direct current of reversed polarity under the following conditions: I_s = 160–170 A, U_a = 20–21 V, v_f = = 160 m/h and v_s = 7.7 m/h. Welding rectifier VDU-506 with constant external characteristic was used as a power supply. Deposition of each next bead was made after complete cooling of the previous bead.

Depositions with experimental self-shielded flux-cored wires were made in order to optimise the type of a B-containing addition. Boron was added to the wires in the form of powder of amorphous boron (99.9 % B), boron carbide B_4C (78.8 % B), boron nitride BN (44 % B), boron trioxide B_2O_3 (31.4 % B) or Fe–Cr–B master alloy containing 19.7 % B and 41.2 % Cr. For comparative metallographic analysis, the used samples of the deposited metal had approximately identical composition, wt.%: 0.12–0.15 B; 2.12–2.30 C; 0.40–0.50 Cr; 0.84–1.02 Si; 1.12–1.42 Mn; 0.22–0.28 Al and 0.08–0.18 Ti. The above concentration of boron in deposited metal (0.12–0.15 %) was provided at its design content of the core of flux-cored wire equal to 0.60–0.75 wt.%.

It was found that crack resistance (presence of microcracks determined by metallography) of deposited metal, other conditions being equal, depends upon the type of a B-containing addition in the core of a flux-cored wire. For example, when using BN and B_2O_3, macrocracks visible to an unaided eye are formed in the deposited bead. At the same time, no cracks were detected for powders of the Fe–Cr–B master alloy, B_4C and amorphous B. A small amount of microcracks was detected in the fusion zone and deposited metal alloyed with amorphous B, NB and B_2O_3. Individual microcracks were fixed when using the Fe–Cr–B master alloy and B_4C.

Differing effect exerted by the studied alloying B-containing components of flux-cored wires on crack resistance of high-carbon deposited metal is related to the probability of formation of the martensite phase and its morphology. Alloying of deposited metal with amorphous B, BN and B_2O_3 (Figure 1, *a–c*) leads to formation of the martensite phase, whereas the use of powders B_4C and Fe–Cr–B prevents martensitic transformation to occur in the deposited metal (Figure 1, *d*, *e*). It can be concluded on the basis of the performed metallographic analysis that alloying B-containing additions can be ranked as follows as to their effect on completeness of martensitic transformation: Fe–Cr–B – B_4C – amorphous B – B_2O_3 – BN. Fusion zone of the investigated deposited samples comprises regions of acicular martensite. However, in the case of using B_4C and Fe–Cr–B master alloy the martensite formed is dispersed, containing individual regions of bainite, rather than having the coarse-acicular structure. Probably, this also prevents initiation and propagation of microcracks.

It is likely that such substantial differences in the effect exerted by B-containing charge materials in a flux-cored wire on crack resistance and microstructure, the boron content of the deposited metal being identical, are associated with the impact on conditions of solidification of the weld pool metal by other chemical elements contained in the alloying additions studied.

It was established (Figure 2) that variations in hardness of deposited metal occurred within a relatively narrow (0.05–0.15 %) range of boron concen-

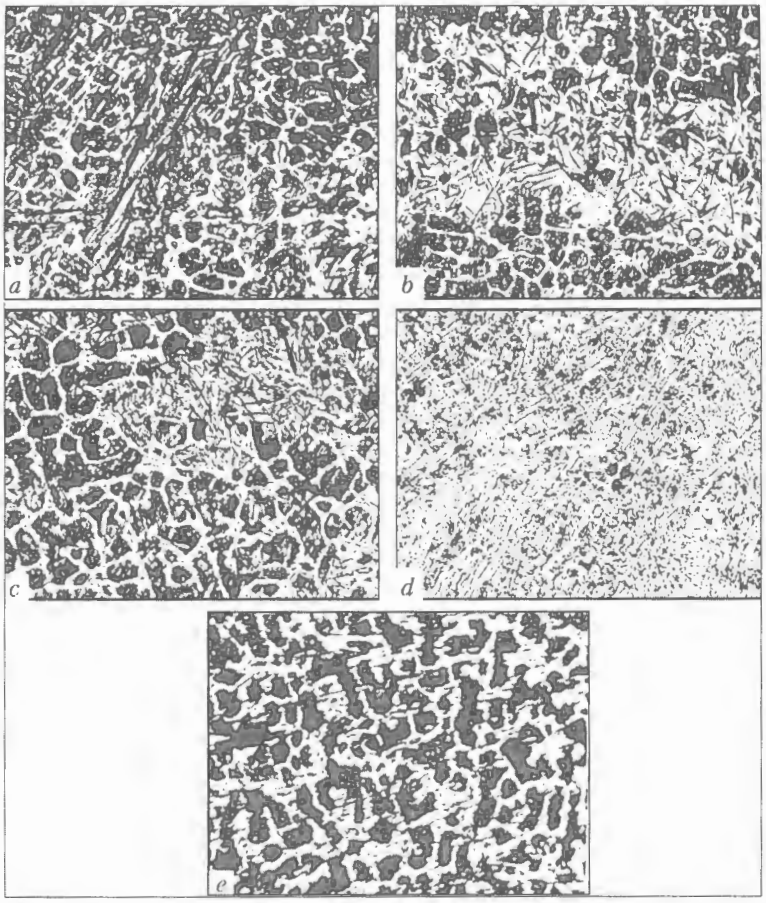

Figure 1. Microstructure of boron-containing (0.12–0.15 %) deposited metal alloyed with boron added to flux-cored wire: *a* — BN; *b* — B_2O_3; *c* — amorphous B; *d* — B_4C; *e* — Fe–Cr–B master alloy (×320)

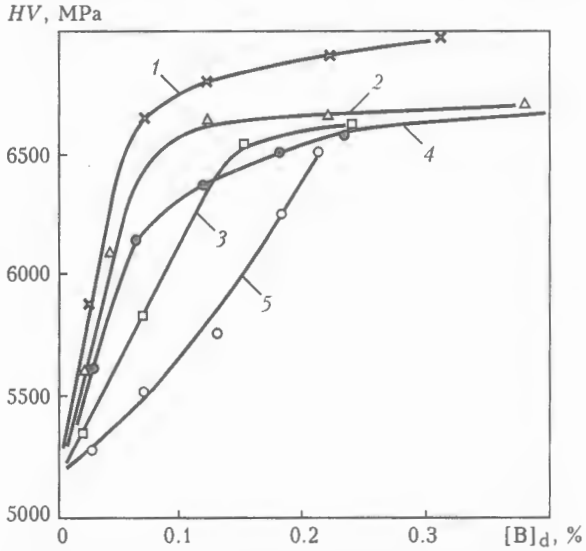

Figure 2. Effect of different boron-containing components of flux-cored wire on microhardness of deposited cast iron: *1* — B_4C; *2* — amorphous B; *3* — BN; *4* — B_2O_3; *5* — Fe–Cr–B master alloy

tration and hardly depended upon the type of a B-containing material of the core of a flux-cored wire, except for the Fe–Cr–B master alloy. In the latter case, increase in the content of the Fe–Cr–B master alloy in a flux-cored wire (and, therefore, growth of the concentration of boron in the deposited metal) leads to a more gradual variations in hardness, compared with the cases of using other B-containing materials. The positive factor here is that variations in the coefficient of filling of a flux-cored wire, taking place in manufacture, hardly have any substantial effect on hardness of the deposited metal. From this standpoint, and allowing for the favourable effect of the Fe–Cr–B master alloy on structure and crack resistance of the deposited metal, using it as a source of microalloying with boron is more preferable, compared with other B-containing components studied.

1. (1961) *Boron, calcium and zirconium in cast iron and steel.* Ed. by S.M. Vinarov. Moscow: Metallurgiya.
2. Krivchikov, S.Yu. (1990) *Development of technology for wear-resistant surfacing of cast iron crankshafts for internal combustion engines using self-shielded flux-cored wire.* Syn. of Thesis for Cand. of Techn. Sci. Degree. Kiev.

THESIS FOR A SCIENTIFIC DEGREE

E.O. Paton Electric Welding Institute of the NAS of Ukraine, Kiev

On February 25, 2004 **G.V. Zhuk** (PWI) defended the thesis of Doctor of science on the subject «Main principles of the influence of thermophysical conditions of metal solidification in electron beam melting on the structure and properties of ingots».

The thesis is devoted to determination of thermophysical regularities of formation of the ingot structure in electron beam melting with an intermediate crucible (EBMIC) under the conditions of high rates of cooling at melt solidification and development of optimized modes of ingot melting on this basis.

Regularities were established of formation of the crystalline structure of ingots of titanium and nickel alloys at EBMIC, taking into account the rates of cooling and solidification of the melt in the mould, and temperature gradient on the solidification front.

Methods of mathematical simulation were used to determine the dependencies of thermophysical conditions of solidification of the metal of titanium ingots in the mould on EBMIC process parameters, namely process efficiency, process cycle frequency, power and electron beam heating distribution.

It is established that lowering of the power of electron beam heating and shifting of its maximum to ingot periphery allows increasing the melt cooling rate by more than 10 times, and the solidification rate by 30 times. Process modes are determined of EBMIC of titanium alloys with the specific power of metal heating in the mould of $(1.5–2)\cdot10^5$ W/m^2, providing a solid-liquid state of ingot surface in the mould and maximum rates of melt cooling.

It is experimentally established that the calculated process conditions allow producing in ingots of titanium alloy Ti–6Al–4V of both a circular and rectangular cross-section an equiaxed structure across the entire ingot section at a homogeneous distribution of alloying elements, structural and phase components. It is further established that the homogeneous structure in the slab ingots of a titanium alloy provides a high level and isotropic nature of mechanical properties.

Further ways are determined to improve the rates of metal cooling at EBMIC, namely melt solidification in microvolumes. A new method is proposed of melt dispersion from an intermediate crucible, using a drum dispersant, rotating at up to 2500 rpm. A mathematical model is developed for producing an ingot from a dispersed melt with forced cooling of the ingot.

It is established that high rates of melt cooling of up to 10^5 K/s at solidification are achieved in this process. High rates of cooling typical for melt dispersion from an intermediate crucible using a drum dispersant allow producing refractory alloy ingots of an ultra-fine structure, fibrous composite materials with minimum thickness of the interlayer on the fibre–matrix boundary, joining titanium alloy ingots without edge melting.

Performed research of ingot structure formation in a broad range of melt cooling rates in electron beam processes with application of an intermediate crucible allowed optimizing the process parameters of melting. Technology of producing slab ingots of titanium alloy Ti–6Al–4V with an equiaxed structure and isotropic mechanical properties has been developed and put into production. This structure is optimum for subsequent rolling of slabs and producing a sheet.

THESIS FOR A SCIENTIFIC DEGREE

E.O. Paton Electric Welding Institute of the NAS of Ukraine, Kiev

On February 18, 2004, **V.A. Brodovoj** (PWI) defended the thesis of Candidate of Science on the subject «Determination of cyclic fatigue life of welded structure elements under the condition of a fatigue crack retardation».

The thesis is devoted to solving the scientific problem of ensuring the performance of welded structures with premature fatigue cracks.

It is shown that one of the possible ways to extend the cyclic fatigue life of materials and load-carrying structural elements is retardation of a fatigue crack by inducing a field of residual compressive stresses ahead of its tip.

It is experimentally established that the residual stresses induced under the impact of cyclic loading in the zones of the stress raiser or fatigue crack interact with artificially induced stresses and form a new stress field, responsible for further propagation of a crack. Investigation of the fields of residual stresses was conducted by an improved acoustic NDT method.

Appropriate testing of specimens for cyclic crack resistance was conducted to determine the effectiveness of retardation of a fatigue crack by inducing compressive stress fields ahead of its tip. Flat specimens of steel St3sp (killed) and aluminium alloy D16AT with a pregrown fatigue crack were tested. Compressive residual stresses were induced in front of the fatigue crack tip by local explosion treatment, point heating or spot weld deposition.

Such experimental results were used to plot kinetic diagrams of fatigue fracture (KDFF), which consist of two parts. The first branch represents the kinetics of fatigue fracture at crack propagation without its retardation. The second branch of the diagram has a different slope and represents the kinetics of fatigue fracture since the moment of retardation. It is seen from KDFF that inducing compressive residual stresses in the crack tip zone significantly lowers the rate of crack growth.

The notion of the coefficient of effectiveness of a fatigue crack retardation was introduced. A correlation of this coefficient with the value and mode of distribution of the induced residual compressive stresses is established. This is the basis for suggesting an experimental-design method for determination of fatigue life of structural elements with a fatigue crack, which propagates in the field of residual compressive stresses induced for its retardation. A number of original programs have been developed to support the respective algorithms, which allows performing the necessary calculation in the PC.

The suggested method was tried out on the basis of experimental investigations of cyclic crack resistance in large-scale specimens of steel St3sp and aluminium alloy D16AT at retardation of a fatigue crack by compressive residual stresses, which were induced due to local strengthening treatments.